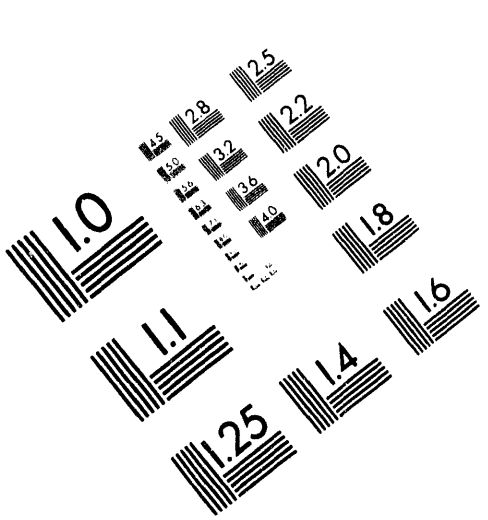

Association for Information and Image Management

1100 Wayne Avenue, Suite 1100
Silver Spring, Maryland 20910

301/587-8202

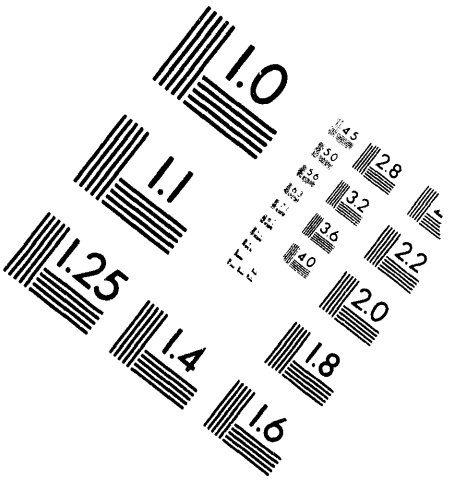

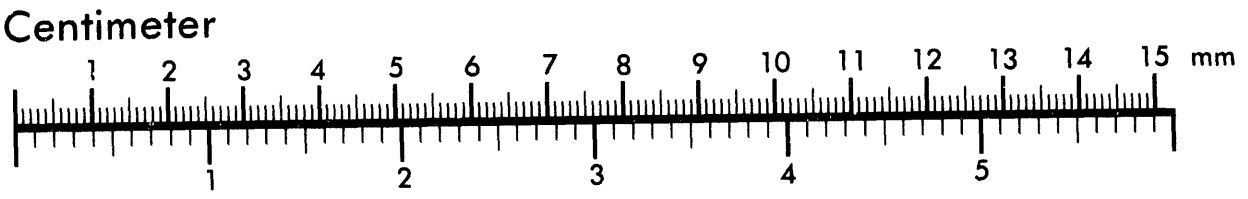

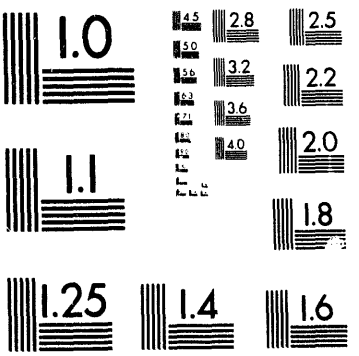

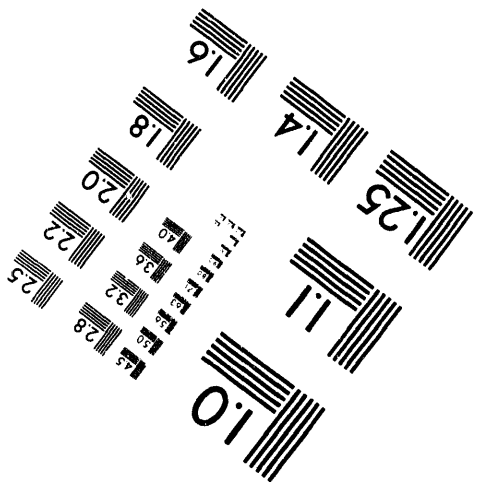

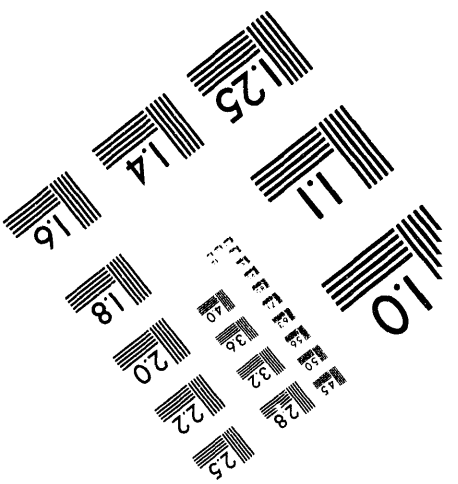

MANUFACTURED TO AIIM STANDARDS
BY APPLIED IMAGE, INC.

1 of 2

SAND94-0012
Unlimited Release
Printed August 1994

Distribution
Category UC-122

EFFECTIVE-STRESS-LAW BEHAVIOR OF AUSTIN CHALK ROCKS FOR DEFORMATION AND FRACTURE CONDUCTIVITY

N. R. Warpinski
Advanced Geophysical Technology Department

L. W. Teufel
Geomechanics Department

Sandia National Laboratories
Albuquerque, NM 87185-5800

ABSTRACT

Austin chalk core has been tested to determine the effective law for deformation of the matrix material and the stress-sensitive conductivity of the natural fractures. For deformation behavior, two samples provided data on the variations of the poroelastic parameter, α, for Austin chalk, giving values around 0.4. The effective-stress-law behavior of a Saratoga limestone sample was also measured for the purpose of obtaining a comparison with a somewhat more porous carbonate rock. α for this rock was found to be near 0.9. The low α for the Austin chalk suggests that stresses in the reservoir, or around the wellbore, will not change much with changes in pore pressure, as the contribution of the fluid pressure is small.

Three natural fractures from the Austin chalk were tested, but two of the fractures were very tight and probably do not contribute much to production. The third sample was highly conductive and showed some stress sensitivity with a factor of three reduction in conductivity over a net stress increase of 3000 psi. Natural fractures also showed a propensity for permanent damage when net stressed exceeded about 3000 psi. This damage was irreversible and significantly affected conductivity. α was difficult to determine and most tests were inconclusive, although the results from one sample suggested that α was near unity.

ACKNOWLEDGMENTS

The authors would like to acknowledge the assistance of ORYX Energy Company in providing both core and technical information. Interactions with ORYX have been invaluable, and we would like to especially acknowledge the efforts of Harold Illich, Joe Perez, Howard White and Bob Skopec. The project was conducted under funds received from the U.S. Department of Energy's oil research program throught the Bartlesville Project Office under contract DE-AC04-76DP000789. Special thanks go to our project managers, Fred Burtch and Bob Lemmon. These results were conducted as a part of a project under DOE's Oil Recovery Technology Partnership.

Table of Contents

LIST OF FIGURES

LIST OF FIGURES Continued

LIST OF TABLES

LIST OF TABLES Continued

INTRODUCTION

The results included in this report are one part of a joint project between ORYX Energy Company and Sandia National Laboratories. The objective of this project was to perform a study of some important rock and reservoir properties that influence the production of hydrocarbons from naturally fractured reservoirs, with particular emphasis on reservoirs currently being completed with horizontal wells. The focus of this study is the Austin chalk, in Texas, where large numbers of horizontal wells have significantly increased production and reserves. However, the rapid draw down of many of these wells and the success of techniques such as large-volume water frac stimulations suggest that many important details of the behavior of this reservoir are not understood.

This study is concerned with the effective-stress-law behavior of the reservoir, in terms of the deformation of the matrix and the conductivity of the natural fractures. Of particular importance is the understanding of the behavior of the matrix rock and the natural fractures with draw down of the reservoir. Draw down changes the effective stress, the total stress, and the deviatoric stress within the reservoir. The amount of change is strongly influenced by the effective-stress law of deformation for the matrix material (the chalk). The changes in stress, in turn, affect the closure and, thus, conductivity of the natural fractures. This type of behavior has never been examined for the chalk.

During the course of this study, the deformation effective-stress-law behavior of two Austin chalk matrix samples were analyzed in great detail. Because of unexpected findings for this low-porosity material, a higher porosity limestone, from the Saratoga formation, was also tested to determine its properties relative to the Austin chalk. In addition, three Austin chalk natural fractures were tested for their conductivity properties. The results from all six samples are included in this report.

BACKGROUND

The behavior of rocks under the combined effects of confining stress and pore pressure is an important issue for any *in situ* petroleum process. For reservoir and near-wellbore behavior, the important issues are permeability, porosity, deformation, and failure. For reasons given below, only aspects of permeability and deformation are addressed here.

In order to simplify the difficulties in dealing with two independent parameters, it is customary to introduce an effective-stress law which relates a net, or effective, stress to some combination of confining stress and pore pressure. This law is usually given as

$$\sigma_{eff} = \sigma - \alpha p, \tag{1}$$

where σ is the stress, p is the pore pressure, and α is a parameter or function that may depend upon both stress and pressure. The classical effective-stress law, given by

$$\sigma_{eff} = \sigma - p, \tag{2}$$

is a simplification of equation 1 that is usually applied to soil mechanics and certain rock mechanic properties. For example, Robin[1] shows theoretically that pore volume compressibility of normal reservoir rocks essentially follows the classical effective-stress law, and Cornet and Fairhurst[2] summarize empirical data showing that failure of rocks also follows the classical effective stress law. The remaining two important issues, permeability and deformation, have only been slightly studied.

The advantages to using effective stress laws are two-fold. First, assuming that the effective-stress law is known, the material behavior can be measured at one pore pressure (often zero) and subsequently predicted for any other pore pressure. There is no need to measure behavior at all combinations of stress and pore pressure. Second, calculations of rock deformation behavior, for example, must be conducted in the effective-stress space, as some fraction of the pore pressure is a neutral stress that offsets the stress in the solid component of the rock. As an example, wellbore stability calculations using the elasticity equations must be calculated using the effective stresses, not the total stresses, or the results will be seriously in error. The application of the effective-stress law can be circumvented by using the full poro-elastic equations, but the parameters defining the effect of pore pressure must still be determined, and, in fact, are determined directly from the effective-stress law, as measured here. .

The major difficulty with application of poro-elasticity or other uses of an effective-stress law is obtaining an accurate model for the material behavior, as rocks are often heterogeneous, nonlinear and anisotropic. Furthermore, Robin[1] has demonstrated that the effective-stress law is dependent upon the particular property or process that is active (e.g., failure, deformation, permeability), so that different laws will be required for each. Deformation and fracture conductivity are, thus, treated separately.

Deformation

In this study, deformation of rocks under the influence of both stress and fluid pressure, often called poro-elasticity, is one of the concerns. Important developments in poroelasticity include works by Biot[3], Biot and Willis[4] and Rice and Cleary,[5] to name a few. An effective-stress-law model for deformation has been developed by Nur and Byerlee,[6] although this model requires an isotropic, homogeneous, single-component material with fully interconnected pore space to be valid. For this model, α is given as

$$\alpha = 1 - K/K_s \,, \tag{3}$$

where K is the bulk modulus of the rock and K_s is the bulk modulus of the skeletal material (only the solid component). Carroll[7] has developed a model for anisotropic materials, but the formulation is highly complex requiring a multitude of material constants.

An approach often taken for deformation behavior is to assume the Nur and Byerlee model is correct and determine both K and K_s in the laboratory, thus arriving at a calculated value of α. The primary uncertainty with this approach is an unknown accuracy and/or range of validity of this model for real rocks. This study presents some initial laboratory data that quantifies the error found in using the Nur and Byerlee model.

Permeability and Conductivity

There is no good theory for the effective-stress law for permeability of rocks, primarily because there is no good law for permeability as a function of rock properties and characteristics. Thus, permeability behavior must be determined empirically. In any study of the Austin Chalk reservoirs, permeability of the matrix rock is very low, so while the matrix may contribute to reservoir volume, it is not important for production. Natural fractures are the dominant production mechanism and they are the focus of this study.

Several theories [8-12] exist to model closure and flow in natural fractures based on asperity contacts between opposing surfaces. While these models are idealized, ignore mineralization and clays, and cannot be used in a predictive sense, they do form a framework under which laboratory or field data can be analyzed. For example, Walsh's model[9] for conductivity in a fracture, K_f^n, of the form

$$K_f^{\,n} = A + B\ln[\sigma - \alpha p] \tag{4}$$

has been useful for correlating both lab[9] and field[13] data, where A and B are constants. The exponent, n, is 1/3 according to Walsh's theory. Important questions concern the amount of conductivity reduction (essentially the constant B) and the value (including stress and pore pressure dependence) of, α, the effective-stress-law parameter.

Walsh[9] examined data by Kranz et al.[14] for flow through tension fractures and polished surfaces, estimating $\alpha = 0.56$ for the tension fractures and $\alpha = 0.9$ for the polished surfaces. Kranz et al. measured permeability reductions of 1-2 orders of magnitude with applied stress. Engelder and Scholz[15] also measured 1-2 orders of magnitude drops in permeability with applied stress. In both of these studies, the important effects of hysteresis in loading, as well as other path dependencies, were recognized. Liquids were the test fluids in both cases.

Boitnott and Scholz[16] developed an ingenious method for determining the effective-stress-law behavior of fractures in impermeable materials while avoiding hysteresis effects. In glass fractures, they obtained α values that decreased from 1.0 to about 0.85 as pore pressure was increased. However, there is considerable uncertainty using their method for porous materials. They also tacitly assume that the effective-stress-law for closure of the fracture is the same as for permeability of the fracture.

In this study, the effective-stress-law behavior of two Austin Chalk natural fractures is measured. Such behavior is extremely important for calculating the change in reservoir production with draw down of the reservoir.

Turbulence

While there is no intention to make a study of turbulence in Austin chalk fractures, highly permeable fractures will often exhibit a significant degree of inertial/turbulence effects. It thus becomes necessary to determine turbulence correction factors for extracting an appropriate intrinsic permeability that can be compared from test to test.

Turbulence has been thoroughly studied for flow through rough parallel plates or open fractures (e.g., Huitt,[17] Whan and Rothfus,[18] Rothfus et al,[19] and Iwai[20]), with transition to turbulence occurring at Reynold's numbers (Re) near 2000. Below Re = 2000, laminar flow conditions are generally predicted by

$$f = 24/Re, \qquad (5)$$

where f is a friction factor, given by

$$f = \frac{\Delta p}{\rho v^2}\frac{w}{L} \tag{6}$$

ΔP is the pressure drop across the fracture length, L, ρ is the fluid density, v is the fluid velocity, and w is the fracture width. Lomize[21] and Louis,[22] however, show that rough fractures have more complicated behavior, with roughness effects increasing the friction factor when the roughness is greater than a critical fraction of the width. To use this classical approach, however, the width must be known at all times. Unfortunately, apertures of natural fractures are not parameters that can readily be determined.

Turbulence in porous media has also been well studied (e.g., Geertsma[23] and Riepe et al.[24]), but the transition Reynold's number has been defined differently depending on the author. Using the Forchheimer equation,

$$\Delta p = \frac{1}{k_i}\mu v + \beta v^2 \tag{7}$$

Geertsma defined the Reynold's number as

$$Re = \frac{\beta \rho v k_i}{\mu} \tag{8}$$

In these equations, μ is the viscosity, k_i is an intrinsic permeability of the porous medium, and β is called the "turbulence factor" or "beta factor." Note that βk_i is a characteristic width dimension of the porous medium. The intrinsic permeability, k_i, is defined by Equation 4 when the velocity is very small. Taking Equation 5 for the definition of the Reynold's number, transition to turbulence begins at Reynold's numbers of about 0.1 to 1.0.

In many natural fractures, the asperity contacts are numerous enough that the natural fracture can more readily be envisioned as a 2-D porous medium than an open fracture. If mineralization is sparse, the fracture flow should tend toward the matrix porous-medium flow in the limit as net confining stress becomes large. Van Golf-Racht[25] discusses the application of the porous-medium approach to turbulent flow in a fracture. For this work, the porous-medium approach was used for turbulence analyses, primarily because of the inability to determine a width of the fracture under the different stress and pore pressure conditions.

EXPERIMENTAL PROCEDURE

Deformation

The experimental procedure[26,27] for deformation consists of measuring the volumetric-strain response of a rock subjected to a compression composed of varying hydrostatic-confining-stress and pore-pressure levels. An 8-in long Austin-chalk core sample, which was provided by ORYX from the Burton O George No. 1 well (Zavala County) at a depth of 7093 ft, was plugged in three mutually perpendicular directions, labeled A, B and C. Plug B was oriented along the hole axis; the orientations of plugs A and C relative to the vertical are unknown, but they both are perpendicular to the hole axis. Core Labs measured a porosity of 3.8% and a grain density of 2.70 gm/cc at this depth.

The Saratoga limestone sample was provide by ORYX from the Sonat Minerals, Inc. No. 1 well (vertical) from Sabine Parish, Louisiana. The depth of the chosen sample was 2737 ft; Core Labs testing yielded porosity of about 11%, grain density of about 2.71, and air permeability of 0.1-0.7 md. The sample is approximately 85-95% calcite, with about equal amounts of clay and quartz. A one-inch diameter horizontal plug was taken from the sample and instrumented with strain gages in axial and circumferential configurations.

All four samples were strain gauged, emplaced in neoprene jackets, and inserted in a modified overburden coreholder. The overburden coreholder uses hydraulic fluid to apply confining stress, while nitrogen supplies the pore pressure. Feedthroughs on one endcap allow for strain-gage wires to exit the coreholder. Figure 1 shows a schematic of the apparatus.

Samples are loaded and unloaded several times ("seasoning") with hydrostatic confining stress alone until rock behavior is stabilized (i.e., repeatable results are achieved on successive cycles), and the effects of relaxation microcracks are diminished. The samples are then saturated with the test fluid and measurements are made at various stress and pore-pressure levels, with care taken to avoid hysteresis and equilibration effects. To minimize pore-pressure-equilibration times, data were taken at constant pore pressure through both loading and unloading cycles in the confining stress.

Sample A was tested first, but the jacket failed immediately, resulting in hydraulic fluid contamination. Samples B and C were then tested, with good results. Finally the Saratoga limestone sample was successfully tested.

Detailed Test Plan

1. Seasoning cycle to close microcracks, bedding relief, and eliminate other nonlinear features. Cycle up to 8000 psi in 1000 psi steps, then back to 0 psi.
2. Seasoning cycle number two, to confirm the results of cycle 1; if cycle 2 overlays cycle 1, no further seasoning is needed. In both of these samples, the 2 cycles were identical and no further seasoning was needed.

3. Load sample to 2000 psi, apply 1000 psi inlet nitrogen pressure and let sample sit and equilibrate until gas flow through the sample raises outlet pressure to 1000 psi. However, at an outlet pressure of 500 psi, make a rough measurement of the permeability by measuring the flow rate.

4. When nitrogen pore pressure has equilibrated at 1000 psi, measure the volumetric strain at confining stresses of 2000 - 8000 psi in increments of 1000 psi.

5. Increase the confining stress to 3000 psi, and apply 2000 psi inlet nitrogen pressure to sample. Let equilibrate until outlet pressure is also 2000 psi.

6. When nitrogen pore pressure has equilibrated at 2000 psi, measure the volumetric strain at confining stresses of 3000 - 8000 psi in increments of 1000 psi.

7. Increase the confining stress to 4000 psi, and apply 3000 psi inlet nitrogen pressure to sample. Let equilibrate until outlet pressure is also 3000 psi.

8. When nitrogen pore pressure has equilibrated at 3000 psi, measure the volumetric strain at confining stresses of 4000 - 8000 psi in increments of 1000 psi.

9. Increase the confining stress to 5000 psi, and apply 4000 psi inlet nitrogen pressure to sample. Let equilibrate until outlet pressure is also 4000 psi.

10. When nitrogen pore pressure has equilibrated at 4000 psi, measure the volumetric strain at confining stresses of 5000 - 8000 psi in increments of 1000 psi.

At this point, the measurement cycle is usually finished. However, these samples were so tight ($K \leq 0.1\mu d$) that it was decided to also conduct a decreasing pore-pressure cycle to check the results. This consisted of the following steps.

11. Reduce inlet and outlet nitrogen pressure to 3000 psi, reduce confining stress to 4000 psi, and let equilibrate.

12. Measure the volumetric strain at confining stresses of 4000-8000 psi in increments of 1000 psi.

13. Reduce inlet and outlet nitrogen pressure to 2000 psi, reduce confining stress to 3000 psi, and let equilibrate.

14. Measure the volumetric strain at confining stresses of 3000-8000 psi in increments of 1000 psi.

15. Reduce inlet and outlet nitrogen pressure to 1000 psi, reduce confining stress to 2000 psi, and let equilibrate.

16. Measure the volumetric strain at confining stresses of 2000-8000 psi in increments of 1000 psi.

17. Reduce inlet and outlet nitrogen pressure to 0 psi, reduce confining stress to 1000 psi, and let equilibrate.

18. Measure the volumetric strain at confining stresses of 1000-8000 psi in increments of 1000 psi.

The end result of these procedures is a set of data consisting of volumetric strain vs stress at several values of pore pressure. Figure 2 shows the test design schematically. These data are then analyzed to extract the effective-stress information.

Conductivity

The apparatus used for conductivity tests is the same one employed for deformation. It consists simply of an overburden coreholder (pressure vessel), output flowmeters, input, output and differential-pressure transducers, a high-pressure nitrogen source (up to 5000 psi), and a high-pressure hydraulic-fluid pump (up to 10,000 psi). In the first two samples, the test fluid was nitrogen, in order to avoid chemical and capillary pressure effects and to improve pressure equilibrium between the fracture and the matrix. In the last sample, the test fluid was KCl water; water was used in an attempt to avoid turbulence corrections. Permeability measurements were made using the steady-state technique, a necessity to insure fracture-matrix equilibration. Except during seasoning cycles, pore pressures of the nitrogen tests were kept above 500 psi so that Klinkenberg corrections would not be needed. Pressure drops across the natural fractures varied from 5-300 psi depending on the type of test.

Three different natural fractures were chosen. These included a hairline, slightly mineralized fracture, and two smooth, poorly mated natural fractures. The samples were prepared by:

1. breaking apart the hairline, partially mineralized fracture (the other two were already separated;
2. epoxying the fractures back together;
3. taking a plug along the strike of the fractures; and
4. dissolving the epoxy.

The sample was then inserted in an overburden core holder and tested with nitrogen or KCl water.

Plug samples were allowed to equilibrate at each stress/pressure condition and then permeability data were taken every 5 seconds over a 5 minute period. These results were examined for any long-term trends (e.g., still equilibrating) and tests were rerun if not stabilized. Data were averaged over the 5-minute test period.

Prior to testing, all of the samples were put through a "seasoning process" by cycling up to maximum stress (determined by conductivity behavior on the first seasoning cycle) and back to low stress several times. Plug permeability was measured during these cycles, and the fracture was considered "seasoned" when permeabilities were identical on several successive cycles. Had the samples not been seasoned, then no effective-stress law correlations could have been made, as the natural fracture would be changing with each test.

As in the deformation measurements, tests were run at constant pore-pressure cycles, both through loading and unloading in order to minimize equilibration time and to avoid having pore-pressure-hysteresis effects embedded within stress-hysteresis effects. Loading data were analyzed as one set and unloading data as a second, separate set.

Fracture conductivity, K_f, is measured by determining the plug permeability, k_p, and recognizing that nearly all of the flow is through the fracture so that

$$K_f h = k_p \frac{\pi d^2}{4} \tag{9}$$

In this relation, d is the plug diameter and h is the fracture height (across the diameter of the plug), measured as the average height at both plug faces. For the samples used in this study, h is approximately equal to the diameter, d. The maximum volumetric flow through the matrix rock is calculated to be no more than 1% of the total flow for all three samples. This amount was considered negligible, and all gas or liquid flow was taken to be through the fracture.

ANALYSIS PROCEDURE

The analysis procedure[26,27] for both deformation and conductivity uses a statistical technique whereby an empirical response surface of either volumetric strain or conductivity is mathematically generated.[28] To do this, the volumetric strains or conductivities are (1) power-law transformed and (2) fit in a least-squares sense by a quadratic surface in both σ and p. The resultant mathematical form of the response surface is given by

$$\theta^{\lambda} = x_1 + x_2\sigma + x_3 p + x_4\sigma^2 + x_5\sigma p + x_6 p^2 \tag{10}$$

or

$$K_f{}^{\lambda} = y_1 + y_2 s + y_3 p + y_4 s^2 + y_5 s p + y_6 p^2 \tag{11}$$

where θ is the volumetric strain, K_f is the conductivity, and the x_i and y_i are fitting parameters to be fit. The power law (λ) employed is determined through a maximum-likelihood approach.[28] Given this empirical function, of the form $\theta(\sigma,p)$ or $K_f(\theta,p)$, Bernabe's formula for the tangent α[29] can be employed as

$$\alpha = -\frac{\partial\theta}{\partial p}\Big/\frac{\partial\theta}{\partial\sigma} \qquad \text{or} \qquad \alpha = -\frac{\partial K_f}{\partial p}\Big/\frac{\partial K_f}{\partial\sigma}. \tag{12}$$

Additionally, standard statistical techniques can be used to determine confidence limits, regression coefficients, and other indicators of the quality of the fit and the variability of the data.

The attractive feature of this technique is that there is no *a priori* need to assume a model for the rock behavior, as is the case when a mechanistic model is fit to the data. This avoids any possibility of biasing the fit. However, such an approach does not provide any information on mechanisms.

RESULTS

Permeability of the Matrix Rock for Sample B

The permeability of sample B could only be roughly measured . To get a measurable flow rate, it was necessary to apply a Δp of 1000 psi across the sample. Such a large Δp can often cause large differences in rock properties across the sample, so the data should not be considered anything more than an estimate of the permeability. The measured value was 0.015 μd, with a measurement standard deviation of 0.004 μd for 50 measurement values.

Poroelastic Behavior, Increasing Pore Pressure, Sample B

The poroelastic response was determined by measuring the volumetric-strain behavior as a function of confining stress at five different pore pressures. The results were then analyzed to determine the relative effects of confining stress and pore pressure on the strain behavior.[1] Figure 3 shows an example of the volumetric-strain response for each of the different pore pressures under loading conditions. Actual raw strain data are given in Tables 1-5. By loading conditions, we refer to increasing confining stress at some constant pore pressure. As can be seen from the figure, the material is very linear and very stiff, with a bulk modulus of about 6.8×10^6 psi. Pure calcite, for comparison, has a bulk modulus of about 10×10^6 psi.

Figure 4 shows the entire set of loading data, and the surface that was statistically fit to the data. These plots were derived from the volumetric strain data given in Table 6. The lines on the surface are constant stress and constant pore pressure (the lines of constant pore pressure are the actual pore pressures at which data were taken). As can be seen in the figure, the data are well fit by the statistical surface, which is very flat. The value of α given on the figure (α_1) is the value at low stress and low pore pressure (a first order approximation).

The equation of the statistical surface can then be interrogated to yield the value of α at any point on the surface. Figure 5 shows the actual α surface. It is very flat because the volumetric strain surface is flat. α varies from about 0.35 at 500 psi confining stress and zero pore pressure to about 0.43 at 8000 psi confining stress and 4000 psi pore pressure. α increases with increasing confining stress and is relatively independent of pore pressure.

Similarly, the unloading volumetric strains at each pore pressure are shown in Figure 6, based on the raw strain data in Tables 7-11. Again, the rock behavior is very linear with about 0.12% maximum strain under these test conditions. The resultant fit of the volumetric strains is shown in Figure 7 (based on data from Table 12) and the unloading α is given in Figure 8. Unloading refers to a decreasing confining stress at a constant pore pressure. The unloading α is about 0.46 at 500 psi confining stress and zero pore pressure, and about 0.39 at 8000 psi confining stress and 4000 psi pore pressure. The unloading α shows an increasing value with increasing confining stress and a decreasing value with increasing pore pressure. This is somewhat different than the loading behavior and demonstrates the importance of the path on all rock properties.

Poroelastic Behavior, Decreasing Pore Pressure, Sample B

Because the rock is so tight, there was some concern that the low values of α might be a result of a non-equilibrated pore pressure within the sample. To check this possibility, the same test matrix was run again, except in decreasing pore-pressure steps. If equilibration was a problem, higher pore pressures should be trapped within the sample for this case, yielding a different behavior pattern for α.

The volumetric-strain response and α surface for loading conditions are shown in Figures 9 and 10. The unloading results for strain and α are shown in Figures 11 and 12. All of the raw strain data and the volumetric strain data are given in Tables 13-24. As can be seen in Figures 10 and 12, the value of α is between about 0.35 and 0.45 for both cases, essentially the same number as seen with increasing pore pressure steps. Thus, pore-pressure equilibration has not affected the results in this test.

Poroelastic Behavior, Increasing Pore Pressure, Sample C

Sample C had material behavior very similar to sample B, thus confirming the accuracy of the results. The volumetric strains at each pore pressure during the loading cycle are shown in Figure 13. As in sample B, the material is very linear with a large bulk modulus (6.8-7.1 x 10^6 psi). The statistical fit (the response surface) is shown in Figure 14 and the variation of α is given in Figure 15. The variability of α with respect to pore pressure is considerably greater for this sample than for sample B, but the average value of α over the data domain is approximately the same. Differences between the pore-pressure response sample B and C are statistically significant, so the slightly different behavior is likely due to rock fabric, such as bedding. The value of α varies from about 0.21 at low stress and pressure to about 0.43 at high stress and pressure. Strain data for the loading results are shown in Tables 25-30.

The unloading volumetric strains for each pore pressure are given in Figure 16, while the response surface are shown in Figure 17, and the α variability is plotted in Figure 18. The effect of pore pressure on unloading behavior is similar to that of loading behavior. The value of α varies between 0.29 and 0.39 over the data domain. Actual data are given in Tables 31-36.

Poroelastic Behavior, Decreasing Pore Pressure, Sample C

To check if the low permeability of the rock was affecting pore-pressure equilibration and skewing the results, additional measurements were made in pressure unloading, but for this sample, these measurements were only made at 2000 psi and 0 psi. These data were essentially the same as the pressure increasing cycle and no further analysis was performed.

Poroelastic Behavior, Increasing Pore Pressure, Saratoga Limestone

The volumetric strains as a function of stress for each of the five pore pressures are shown in Figure 19 for the loading cycle. In loading, the limestone shows nearly linear behavior, except at low stress values. The bulk modulus of this material varies from about 2.4-3.3 $x10^6$ psi over the range of stress and pressures tested. The response surface for loading is shown in Figure 20 and the variation of α is given in Figure 21. The value of α in loading is relatively insensitive to either stress or pressure, varying from about 0.82 to 87 over the data domain. All data for the loading response are given in Tables 37-42.

The volumetric strains for each of the pore pressures during the unloading cycle are shown in Figure 22. The behavior in unloading is distinctly different (less linear) than the loading behavior, but the bulk modulus is nearly the same, varying from 2.1-3.4 x 10^6 psi. The response surface is shown in Figure 23 and the α variation is given in Figure 24. In unloading, there is slightly more variability in α, with the value ranging from 0.9 to 1.03. Strain results are tabulated in Tables 43-48.

Poroelastic Behavior, Decreasing Pore Pressure, Saratoga Limestone

To check the results, the deformation behavior was also measured during cycles of decreasing pore pressure. The response surface for loading is shown in Figure 25 and the α variation is given in Figure 26. There is little difference between these results and those shown in Figures 17 and 18. Strains obtained during pressure unloading are given in Tables 49-60.

Response-Surface Parameters for Deformation Tests

The response surface parameters of all of the deformation tests are given in Table 61. Included in this table are the values of the various x_i and the power-law variable, λ. Care must be taken not to extrapolate any results outside of the domain of the data. The data domain can be determined by examining the maximum and minimum stresses and pressures in either the figures or the tables.

Fracture Conductivity for Fracture 1

The first fracture tested, labeled fracture 1, was a hairline natural fracture with sparse mineralization on the surface of the fracture. This fracture was taken from the Burton O. George No. 1 core. The first set of tests run were seasoning cycles to try to stabilize rock behavior and provide reproducible rock conductivities on each successive run. The seasoning is usually performed by starting at some nominal confining stress (1000 psi) and pore pressure (500 psi), and increasing the confining stress in increments up to the maximum test value. Conductivity is measured at each increment through both loading and unloading cycles (back down to the original level). With most tight rocks, only one or two seasoning cycles are required. With this sample, 6000 psi was chosen as a maximum confining stress value, but the rock behavior could not be stabilized. With each cycle the conductivity of the sample continued to decrease, and the loading was permanently damaging the sample.

The sample was taken out of the core holder and examined, and several areas exhibited crushed calcite residues. These were clearly the high points on the fracture and therefore experienced the greatest stress levels. These areas were thoroughly cleaned, the fracture was remated, and the sample was again inserted into the apparatus. This time the maximum confining-stress test value was 2000 psi, and the sample behavior was easily stabilized.

The test matrix shown in Figure 27 was then run on the sample to determine the effective-stress law for fracture conductivity. The confining stresses were intentionally kept low to avoid any permanent damage to the fracture. The conductivity results are shown in the 3-D plot of Figure 28 and are given in Table 52. While the conductivity is quite low, this fracture still has a permeability ranging from about 0.1 to 0.3 md, but the width is extremely narrow.

A plot of α versus stress and pore pressure is shown in Figure 29. While this plot appears to show large variations in the α behavior, the confidence limits on α are only about ± 0.3 at the 95% level. Thus, all that can be said about these results is that the value of α for this Austin Chalk fracture is near unity over the range tested. The poor confidence limits are due to two factors, the low conductivity of the fracture and the limited test range. Higher permeability fractures should provide better information (but not too high, or turbulence will cause problems).

After completing the effective-stress-law matrix, the sample was reloaded several times in order to determine at what stress level permanent deformation begins. The first tests of this sample had used loading cycles up to 2000 and 6000 psi, and the results were reversibility and permanent damage respectively; this is shown in Figure 30. To better define the point at which damage begins to occur, loading cycles were run up to 3500 psi, and then 5000 psi. The 3500 psi cycles possibly showed a small amount of continuing damage, but it was very small and difficult to consistently measure. The 5000 psi cycles showed a considerable amount of continuing, permanent damage. Since the pore pressure for these tests was 500 psi, this fracture can only sustain a net normal stress of about 2500-3000 psi before it begins to irreversibly lose its conductivity.

Fracture Conductivity for Fracture 2

Fracture sample number 2 was also a natural fracture taken from the Burton O. George No. 1 core, but its characteristics were entirely different. This fracture had a smooth appearance, with no mineralization, and only a trace of plumose structure. However, the structure that could be seen indicated that the fracture was natural and not induced by the coring.

The fracture was first run through seasoning cycles to stabilize behavior. Care was taken to not let the net stress (stress minus pore pressure) exceed 3000 psi, the maximum that could be sustained on the previous sample without inducing permanent damage. Seasoning was successfully achieved in four cycles.

This sample was found to have very high permeability, and inertial/turbulence effects were large. Attempts were made to account for the turbulence, but the resultant data set acquired large measurement errors during the correction process. As a result, the conductivity of the sample could not be used to deduce the effective-stress law for this fracture. Nevertheless, the conductivity data are still useful for showing the stress sensitivity of this type of fracture. Figure 31 shows the conductivity plot and the response surface and Table 53 gives the conductivity data that make up this graph. The response surface is shown to highlight trends in the data, but it could not be used for estimates of α because of the errors, which resulted in confidence limits of ± 1.0 at the 95% level. This large value is obviously unacceptable.

The fracture exhibits a drop in conductivity of approximately 2.5 with a net stress level increasing from 500 psi to 3500 psi, so there approximately the same stress sensitivity to this type of fracture as seen in other tests.[30] However, most of the conductivity change occurs within the first 1000 psi, an amount less than the initial effective stress on the fractures in the reservoir. Thus, changes in conductivity within the reservoir are likely to be small. If these fractures are important pieces of the production mechanism, then this small sensitivity under reservoir conditions may explain why Austin chalk production does not drop off faster.

To circumvent the difficulties caused by inertial-turbulence effects, an attempt was made to re-measure this sample with KCl-water as the test fluid. However, in the process of initial testing with water, the sample began to show signs of permanent damage. While this change could have been due to chemical effects of the water, an examination of the fracture showed that small chips were flaking off the edge of the fracture, and the creation of fines and changes in the contact area are most likely responsible for the apparent damage. This sample could not be tested further.

Turbulence data for fracture 2

Since a large amount of turbulence data were obtained during the course of testing of this fracture, the data are also reported here. Table 54 gives all of the data for each nominal stress and pore pressure level, and Figures 32-66 show the turbulence plots. The y intercept of these plots, the intrinsic conductivity at the given stress and pressure level, is value reported in Table 53 as the conductivity. The β factors, which are related to the slope of the curve, are given in Table 55. β factors range from 2.24-6.01 x 10^6 ft^{-1}.

Fracture Conductivity for Fracture 3

Sample 3 was taken from the same natural fracture as sample 2, but showed considerably different response. In this case the test fluid was KCl water The fracture took 11 cycles before it appeared

seasoned, and the conductivity of the fracture was about three orders of magnitude lower than sample 2. These initial results show that fracture conductivity varies widely over the surface of a fracture and a single measurement of the conductivity may not be sufficient to interpret the conductivity of the fracture.

Similar to sample 2, the results were not suitable to obtain accurate data on the effective-stress law, but the stress sensitivity was measured. Figure 67 shows the conductivity as a function of stress and pressure. The data for this plot are taken from Table 56. There is about a factor of three decrease in conductivity as net stress is increased from 500 to 3500 psi. Most of the decrease occurs with the first 500 psi additional stress.

DISCUSSION

Deformation

This series of tests has provided the first accurate measurements of the effective-stress law for deformation of Austin chalk matrix rocks. In addition, the effective-stress law for a Saratoga limestone has also been measured. When these results are integrated with previous measurements of α in other carbonates, a general trend begins to emerge.

Figure 68 shows the measured value of α at a selected condition (5000 psi stress, 2000 psi pore pressure) as a function of porosity. The unloading data are presented here because they are considered to be the most accurate measure of α. The value given by Equation 3 (theory) is also shown. The theoretical value ranges from about 15-30% lower than the measured value.

Figure 69 shows the measured and theoretical values of α as a function of permeability. Although the data are plotted on a log scale, the measured data show a more consistent monotonic relationship between α and permeability than between α and porosity (Figure 68). This figure is only valid for one stress and pressure condition and there is some variability of α with stress and pressure, but the results shown in Figures 68 and 69 are representative of the general behavior throughout the data domain.

Since the measurement of α is a time-consuming, difficult process, it would be helpful if results from a few carbonate samples could be used to estimate α for other carbonates. If the matrix rock material is the same for all samples (calcite, in this case), then it is reasonable to assume that the pore and grain structures are the primary influence on the effective-stress law. Such structures would likely represent themselves in both the porosity and the permeability of the material, and cross plots of α as a function of these parameters could show behavior trends. Figures 68 and 69 are the beginning of such a correlation, although considerably more work remains to prove that a general trend for carbonates exists.

The results shown in Figures 68 and 69 illustrate that the theoretical value of α is not always a good approximation to the actual value. Rice and Cleary[5] have argued that Equation 3 is not appropriate, as it assumes that the skeletal material is homogeneous, that there is no unconnected porosity, that there are no inhomogeneities or discontinuities, etc. In other words, the theory only holds for a perfect rock. For the Austin Chalk sample, K is about 6.8×10^6 psi and K_S is about 9.1×10^6 psi. Thus, the theoretical value of α is about 0.25, or about 25% less than measured.

The error in the theory is not surprising, considering the severe assumptions that were required. These assumptions include linear, homogeneous and isotropic behavior, a single-component material, and fully interconnected pore space. Nevertheless, for the carbonate rocks studied here, many of these assumptions are acceptable. For example, these rocks are primarily a single component, many are relatively homogeneous, some exhibit very linear behavior, and many have nearly fully interconnected pore spaces, as measured by the unjacketed bulk modulus relative to pure calcite's bulk modulus. The primary assumption that cannot be met in most of these rocks is isotropy, and this is likely to be the primary source of model error. Carroll[7] provides a theoretical derivation for an anisotropic material,

although the equations are complex even for the simplest case of transverse anisotropy. Such a model should be considered in the future.

The unloading data provide the best estimate of α because relaxation microcracks[26] have the smallest effect on material properties under unloading conditions. During loading conditions, relaxation microcracks that are already open require considerably greater pressures to reclose. In this study, the values of α in loading are slightly lower than the unloading values. This behavior suggests that the *in situ* value of α may be somewhat greater than these lab measurements show, as decreasing microcrack activity appears to increase α. It is impossible to entirely eliminate the effects of relaxation microcracks in laboratory tests, but they can be minimized by seasoning the sample and using unloading data.

Fracture Conductivity

Although it was not possible to obtain high quality information on the effective-stress law for fracture conductivity, the limited data available suggest that α for this process is not far from unity. This is consistent with previous measurements[30] of natural fractures in other lithologies. The largest difficulty in making accurate conductivity measurements appears to be the propensity of the rock to crush with loading, and thus change the properties of the fracture during the testing. Of course, any analysis of effective-stress-law behavior is suspect if the fracture conditions are changing. Such damage can be minimized by performing the analysis over a very limited stress range, but then the statistical significance decreases as the range decreases. The best results are obtained when data are obtained over wide ranges of stress and pressure.

Data from the three fractures show that the conductivity is stress sensitive, but most of the sensitivity occurs within the first 1000 psi of loading. Natural fractures in the reservoir already have a higher loading on them, so additional stress effects, as would occur during draw down, will not be large. Thus, production would not be likely to suffer much with moderate draw down. However, with large drawdowns (>3000 psi), the aspects of permanent damage become important and reservoir conductivity is likely to suffer irreversible declines. Under such conditions, remedial treatments, such as water fracs, are likely to clear out fines and provide better production until additional damage occurs.

The large differences in conductivities found in samples 2 and 3, which are taken from the same natural fracture less than an inch apart, shows that a single measurement of fracture conductivity may not have much significance. There certainly is a scale effect and the size of the plugs in this test were insufficient to capture the true overall fracture conductivity, if such a property even exists. Nevertheless, the amount of conductivity reduction with net stress was very similar for all fractures.

CONCLUSIONS

We have completed an initial series of laboratory measurements of the deformation poroelastic response of Austin Chalk core. The sample tested was from the Burton O. George #1 well, at a measured depth of 7093 ft. The poroelastic parameter, α, in the effective-stress law, $\sigma_{eff} = \sigma_{total} - \alpha p$, is found to have a value near 0.4 (at reservoir conditions) for deformation, much lower than any other rocks that we have tested. α is slightly dependent on stress and pressure,.

These present results have important implications for the mechanical behavior of the wellbore and the natural fractures. Since α is low, there is initially a very high effective stress within the reservoir. However, with draw down, the effective stresses will not increase very much. Thus, wellbore stability will not change much with draw down.

These results also show that the value of α derived from equation 3 can be considerably in error. Measured values of α are 0.1-0.2 greater than predicted for all samples tested, giving a 15-30% discrepancy.

For carbonates, there appears to be a trend of decreasing α with decreasing permeability and porosity. This is not unexpected since decreasing permeability and porosity indicate an increasing volume of grain material relative to pore space, which will increase K in Equation 2.

The experimental procedure and statistical analysis used here can provide accurate data on α for deformation of this rock. The 95% confidence limits on α, based on the least-squares fit of the response surface for each sample, are ± 0.03 for the Austin chalk, and ± 0.06 for the Saratoga limestone over the range of experimental conditions.

Natural fractures in Austin chalk show a factor-of-three reduction in conductivity with increasing stress up to a net stress of about 3000 psi. Above this value, permanent damage begins to occur and irreversible damage significantly decreases fracture flow characteristics.

It was not possible to obtain an accurate measurement of the effective-stress-law behavior of Austin chalk fractures, although some data suggest that α is not far from unity.

REFERENCES

1. Robin, P-Y. F., "Note on effective pressure," *J. Geophys. Res.*, Vol. 78, pp. 2434-2437, 1973.
2. Cornet, F.H. and Fairhurst, C., "Influence of Pore Pressure on the Deformation Behavior of Saturated Rocks," Proc., Third Congress of the Int. Soc. for Rock. Mech., Vol. 1, Part B, pp. 638-644, Nat. Acad. of Sci., Washington, D.C., 1974.
3. Biot, M. A., "General theory of three-dimensional consolidation," *J. of Appl. Phys.*, Vol. 12, pp. 155-164, 1941.
4. Biot, M. A. and Willis, D. G., "The elastic coefficients of the theory of consolidation," *J. of Appl. Mech.*, Vol. 24, pp. 594-601, 1957.
5. Rice, J. R. and Cleary, M. P., "Some basic stress diffusion solutions for fluid-saturated elastic porous media with compressible constituents," *Rev. Geophys. and Space Phys.*, Vol. 14, pp. 227-241, 1976.
6. Nur, A. and Byerlee, J. D., "An effective stress law for elastic deformation of rocks with fluids," *J. Geophys. Res.*, Vol. 76, pp. 6414-6419, 1971.
7. Carroll, M. M., "An effective stress law for anisotropic elastic deformation," *J. Geophys. Res.*, Vol 84, pp. 7510-7512, 1979.
8. Greenwood, J. A. and Williamson, J. B. P., "Contact of Nominally Flat Surfaces," *Proceedings, Royal Society of London*, Series A, Vol. 295, pp. 300-319, 1966.
9. Walsh, J. B., "Effect of Pore Pressure and Confining Pressure on Fracture Permeability," *Int. J. Rock Mech., Min. Sci. & Geomech. Abstr.*, Vol. 18, pp. 429-435, 1981.
10. Tsang, Y. W. and Witherspoon, P. A., "Hydromechanical Behavior of a Deformable Rock Fracture Subject to Normal Stress," *J. of Geophys. Res.*, Vol. 86, No. B10, pp. 9287-9298, October 10, 1981.
11. Brown, S. R. and Scholz, C. H., "Closure of Random Elastic Surfaces in Contact," *J. of Geophys. Res.*, Vol. 90, No. B7, pp. 5531-5545, June 10, 1985.
12. Elsworth, D. and Goodman, R. E., "Characterization of rock Fissure Hydraulic Conductivity Using Idealized Wall Roughness Profiles," *Int. J. of Rock Mech., Min. Sci. & Geophys. Abstr.*, Vol. 23, No. 3, pp. 233-243, 1986.
13. Warpinski, N. R., "Hydraulic Fracturing in Tight, Fissured Media," *JPT*, February 1991, pp. 146-152, 208-209.
14. Kranz, R. L., Frankel, A. D., Engelder, T. and Scholz, C. H., "The Permeability of Whole and Jointed Barre Granite," *Int J. of Rock Mech., Min. Sci. & Geophys. Abstr.*, Vol. 16, pp. 225-234, 1979.
15. Engelder, T. and Scholz, C. H., "Fluid Flow along Very Smooth Joints at Effective Pressures up to 200 MegaPascals," in **Mechanical Behavior of Crustal Rocks**, Geophysical Monograph 24, American Geophysical Union, Washington D.C., pp. 147-152, 1981.
16. Boitnott, G. N. and Scholz, C. H., "Direct Measurement of the Effective Pressure Law: Deformation of Joints Subject to Pore and Confining Pressures," *J. of Geophys. Res.*, Vol. 95, No. B12, pp. 19,279-19,298, November 10, 1990.

17. Huitt, J. L., "Fluid Flow in Simulated Fracture," *AIChE Journal*, Vol. 2, No. 2, pp. 259-264, June 1956.

18. Whan, G. A. and Rothfus, R. R., "Characteristics of Transition Flow Between Parallel Plates," *AIChE Journal*, Vol. 5, No. 2, pp. 204-208, June 1959.

19. Rothfus, R. R., Archer, D. H., Klimes, I. C. and Sikchi, K. G., "Simplified Flow Calculations for Tubes and Parallel Plates," *AIChE Journal*, Vol. 3, No. 2, pp. 208-212, June 1957.

20. Iwai, K., "Fundamental Studies of Fluid Flow through a Single Fracture," PhD Thesis, University of California, Berkeley, December 1976.

21. Lomize, G. M., "Water Flow in Jointed Rock," *Gosenergoizdat*, Moscow, 1951.

22. Louis, C., "A Study of Groundwater Flow in Jointed Rock and Its Influence on the Stability of Rock Masses," Imperial College Rock Mechanics Research Report No. 10, 1969.

23. Geertsma, J., "Estimating the Coefficient of Inertial Resistance in fluid Flow through Porous Media," *SPEJ*, Vol. 14, pp. 445-450, October 1974.

24. Riepe, L., Sachs, W. and Schopper, J. R., "Pressure Effects on Permeability," Transactions, Eight European Formation Evaluation Symposium, London Soc. of Prof. Well Log Analysts, London, England, March 14-15, 1983.

25. Van Golf-Racht, T. D., **Fundamentals of Fractured Reservoir Engineering**, Elsevier Scientific Publishing Co., New York, 1982.

26. Warpinski, , N.R. and Teufel, L.W., "Determination of the effective-stress law for permeability and deformation in low-permeability rocks," *SPE Formation Evaluation*, Vol. 7, pp. 123-131, 1992.

27. Teufel, L.W. and Warpinski, N.R., "Laboratory determination of effective-stress laws for deformation and permeability of chalk," *Third North Sea Chalk Symp.*, Copenhagen, Denmark, 1990.

28. Box, G.E.P. and Draper, N.R., **Empirical Model Building and Response Surfaces**, John Wiley & Sons, N.Y., 1987

29. Bernabe, Y., "The effective pressure law for permeability in Chelmsford granite and Barre granite," *Int. J. Rock Mech., Min. Sci. & Geomech abstr., Vol. 23*, pp. 267-275, 1986.

30. Warpinski, N.R., Teufel, L.W. and Graf, D.C., "Effect of Stress and Pressure on Gas Flow Through Natural Fractures," SPE 22666, Proc., 66th Annual SPE Tech. Conf., Vol Ω, Dallas, TX, pp. 105-118, Oct. 6-9, 1991

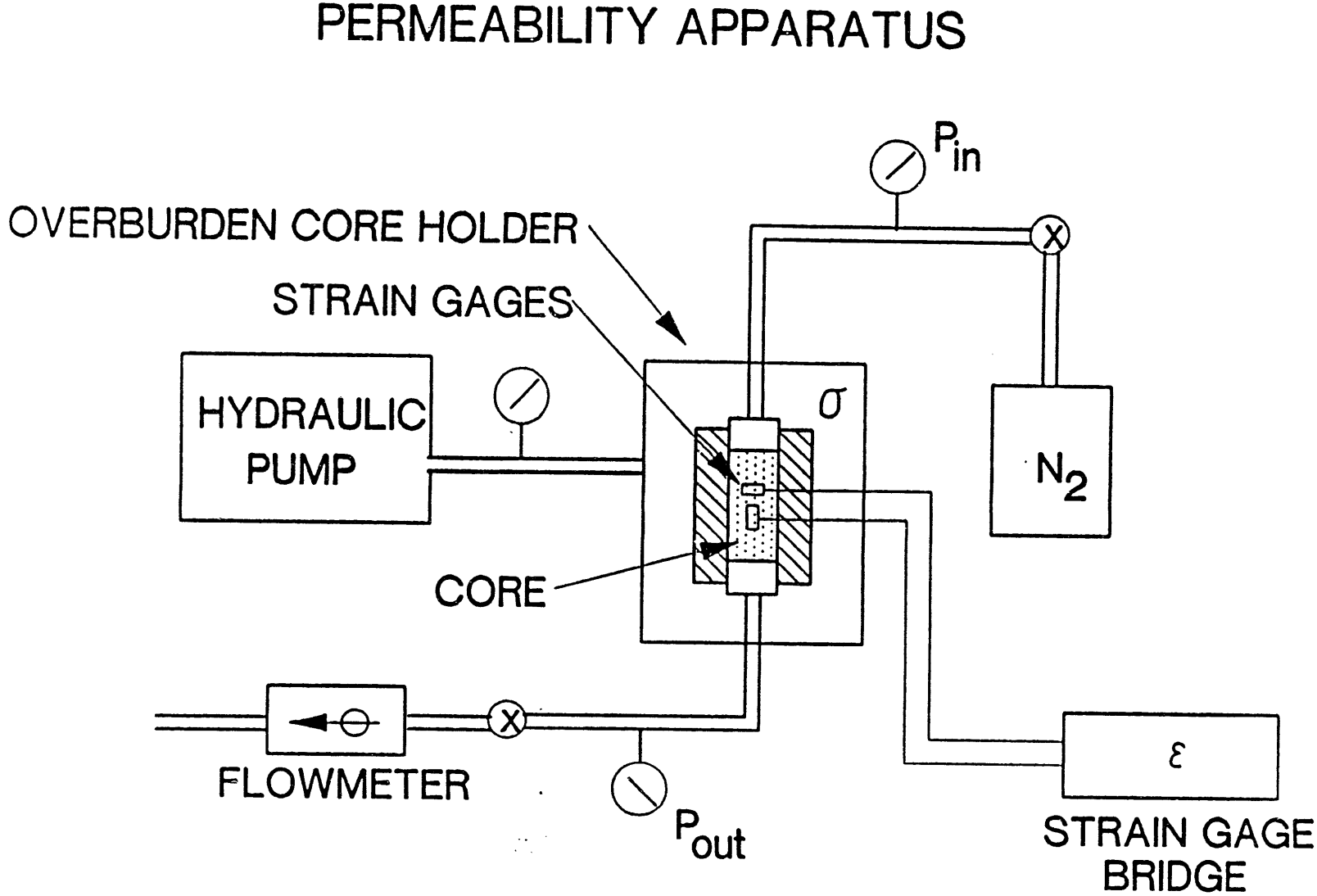

Figure 1 Permeability apparatus

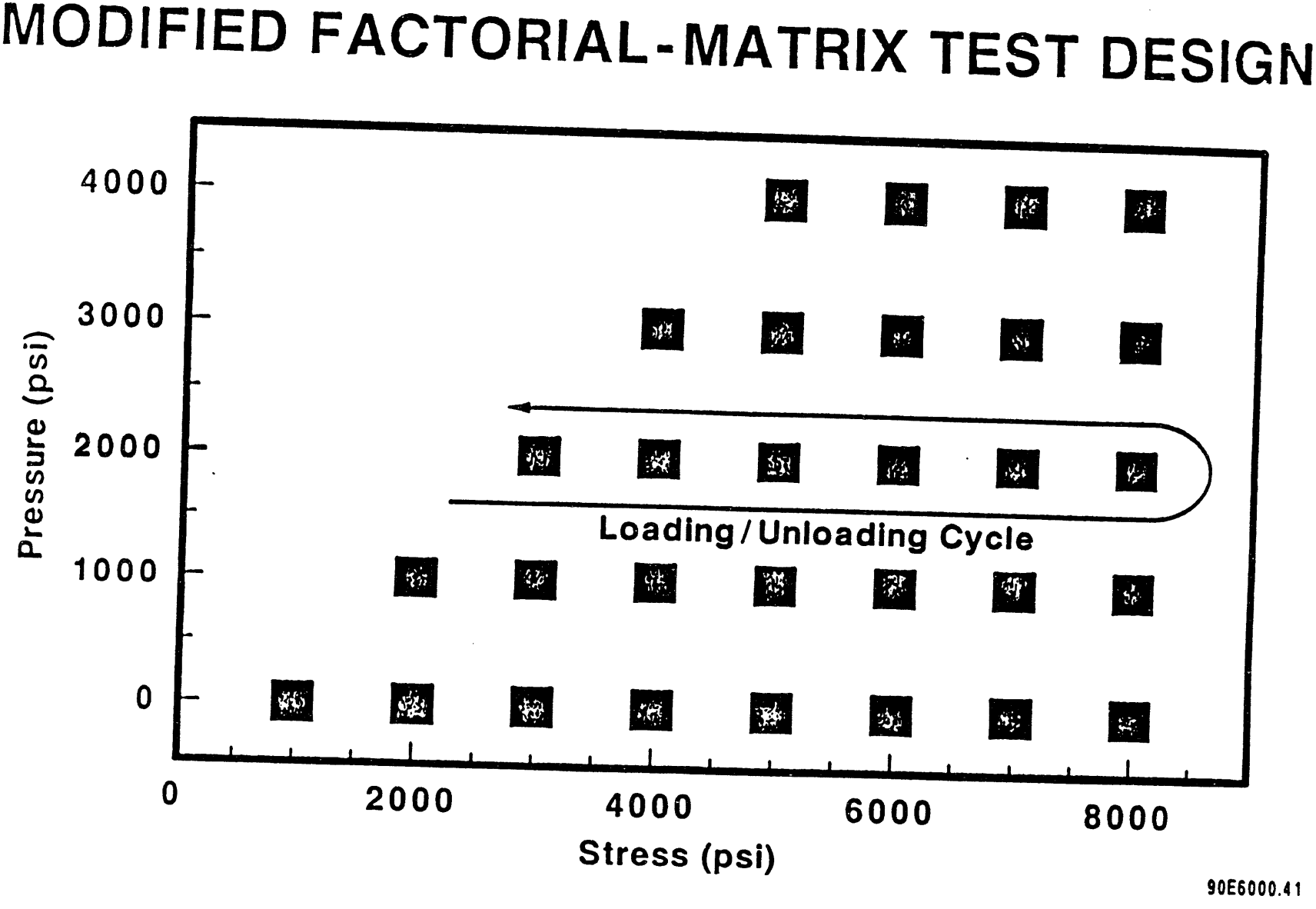

Figure 2 Design matrix, strain

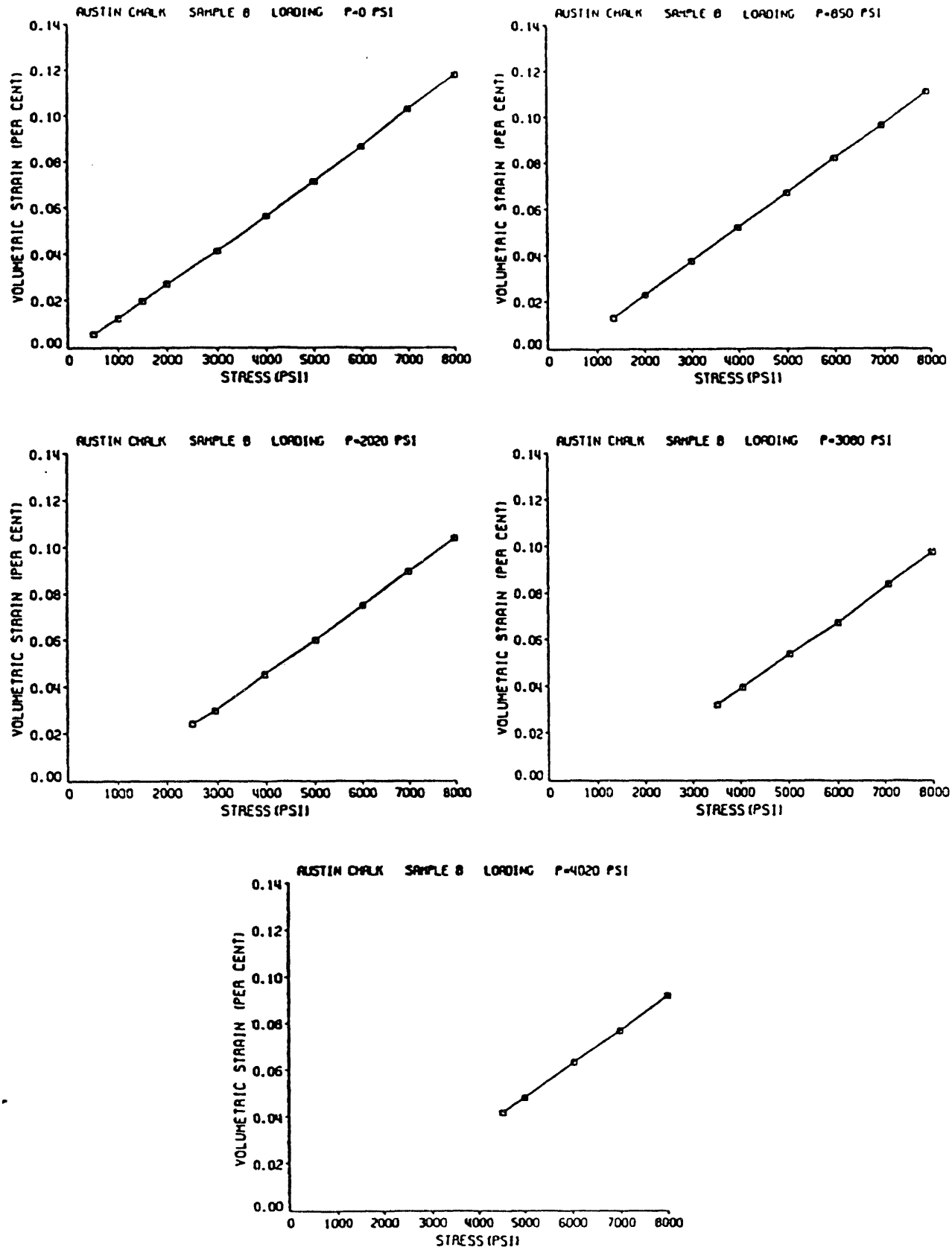

Figure 3 Volumetric strain data, sample B, loading

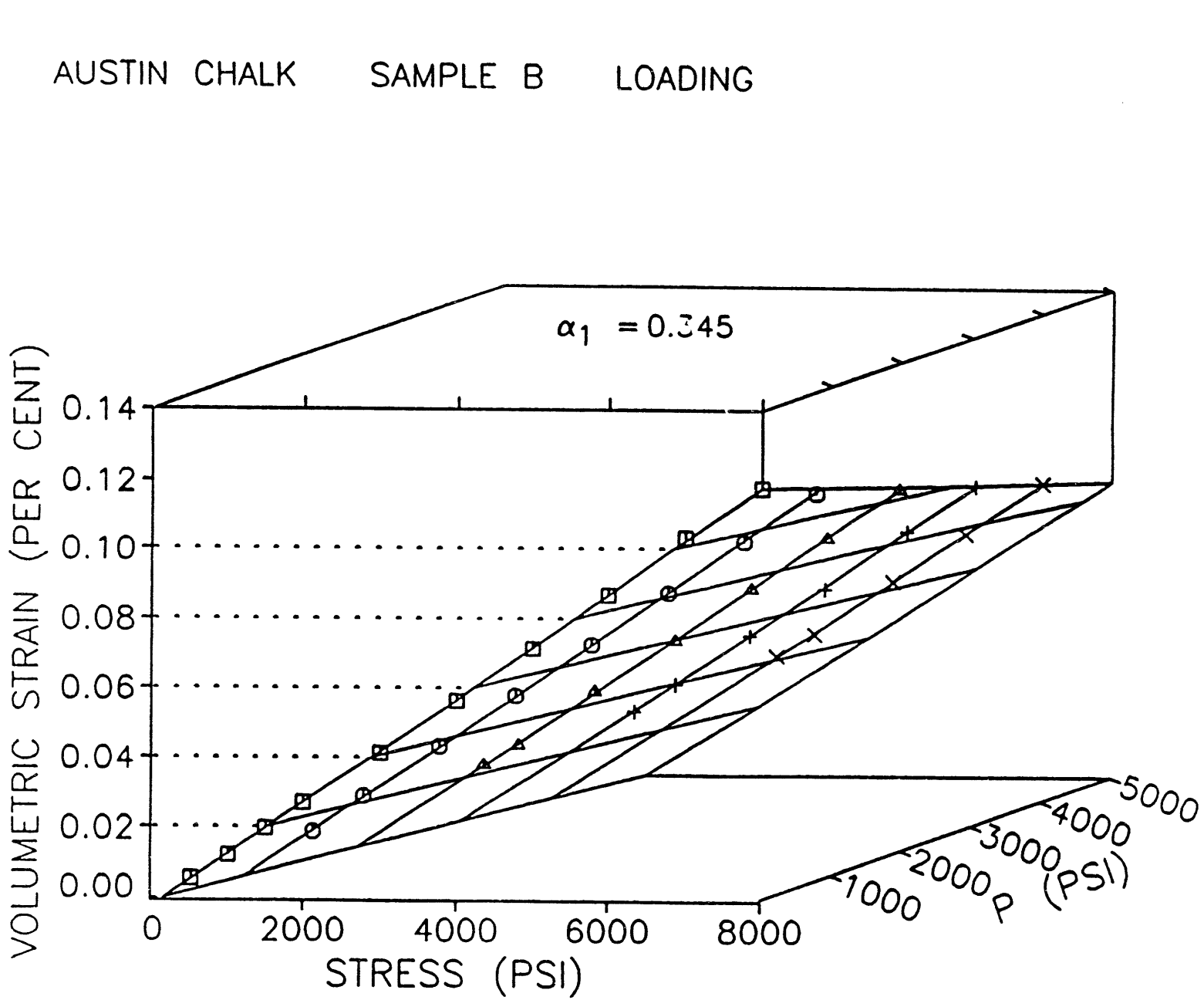

Figure 4 **Response surface, sample B, loading**

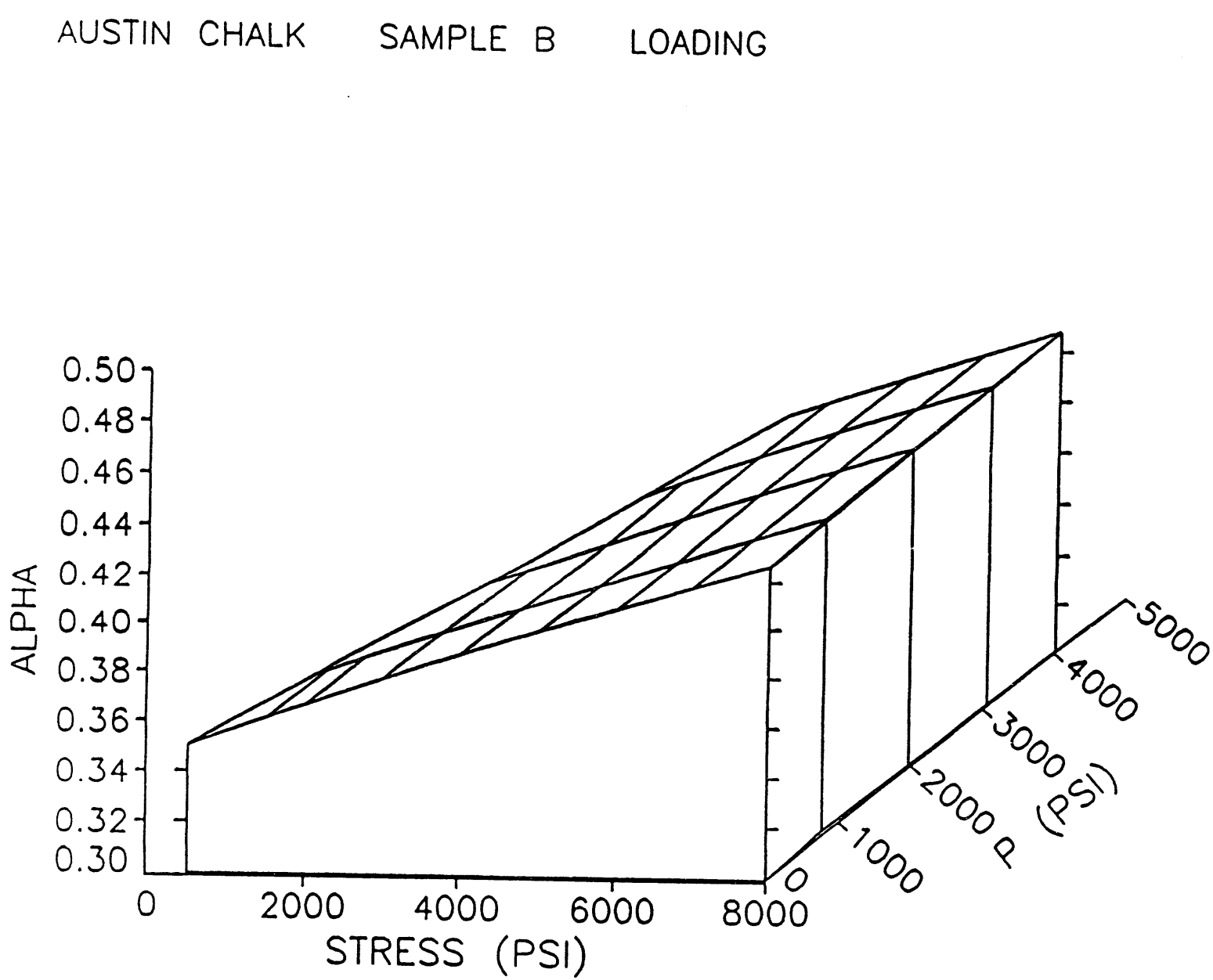

Figure 5 **α surface, sample B, loading**

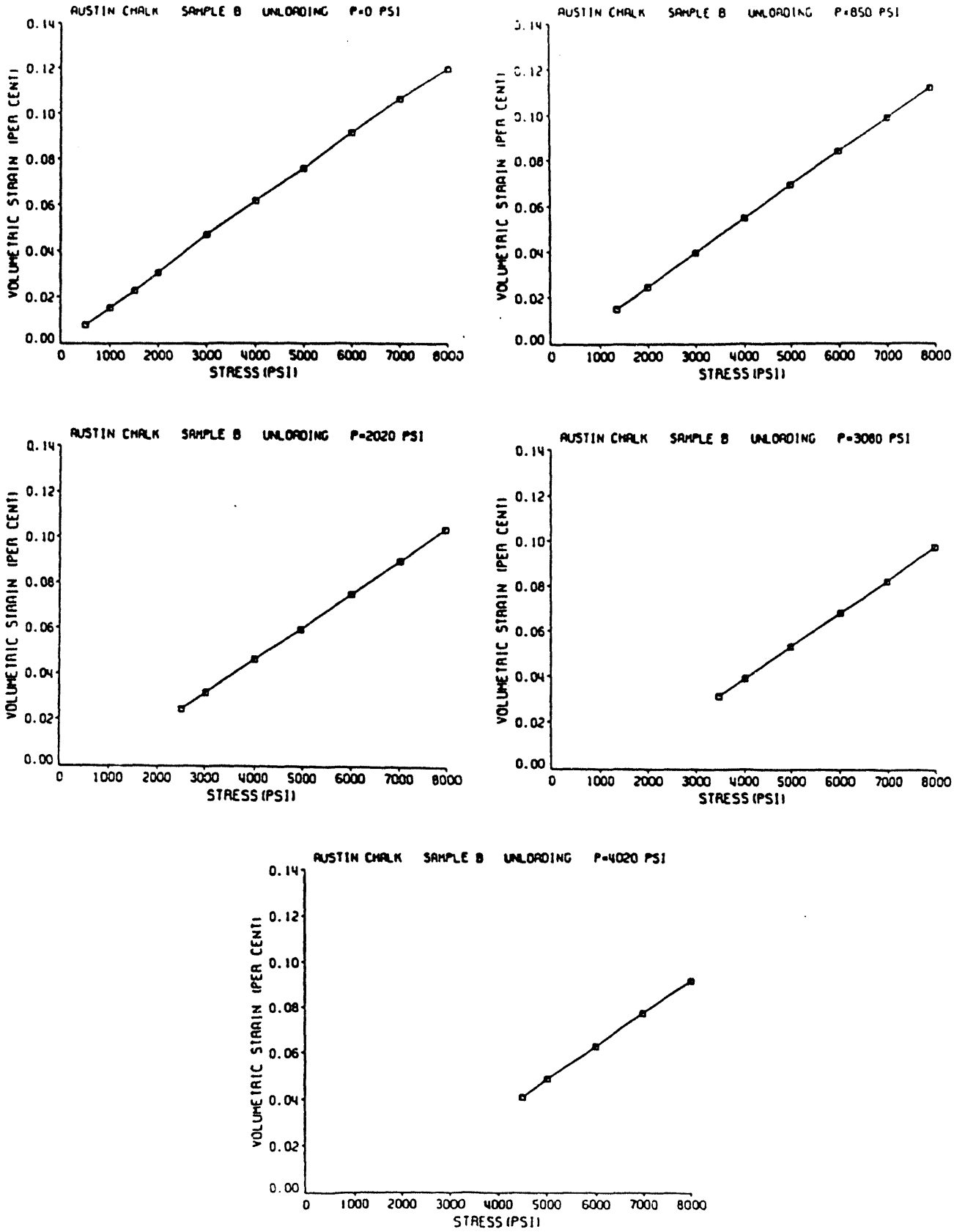

Figure 6 Volumetric strain data, sample B, unloading

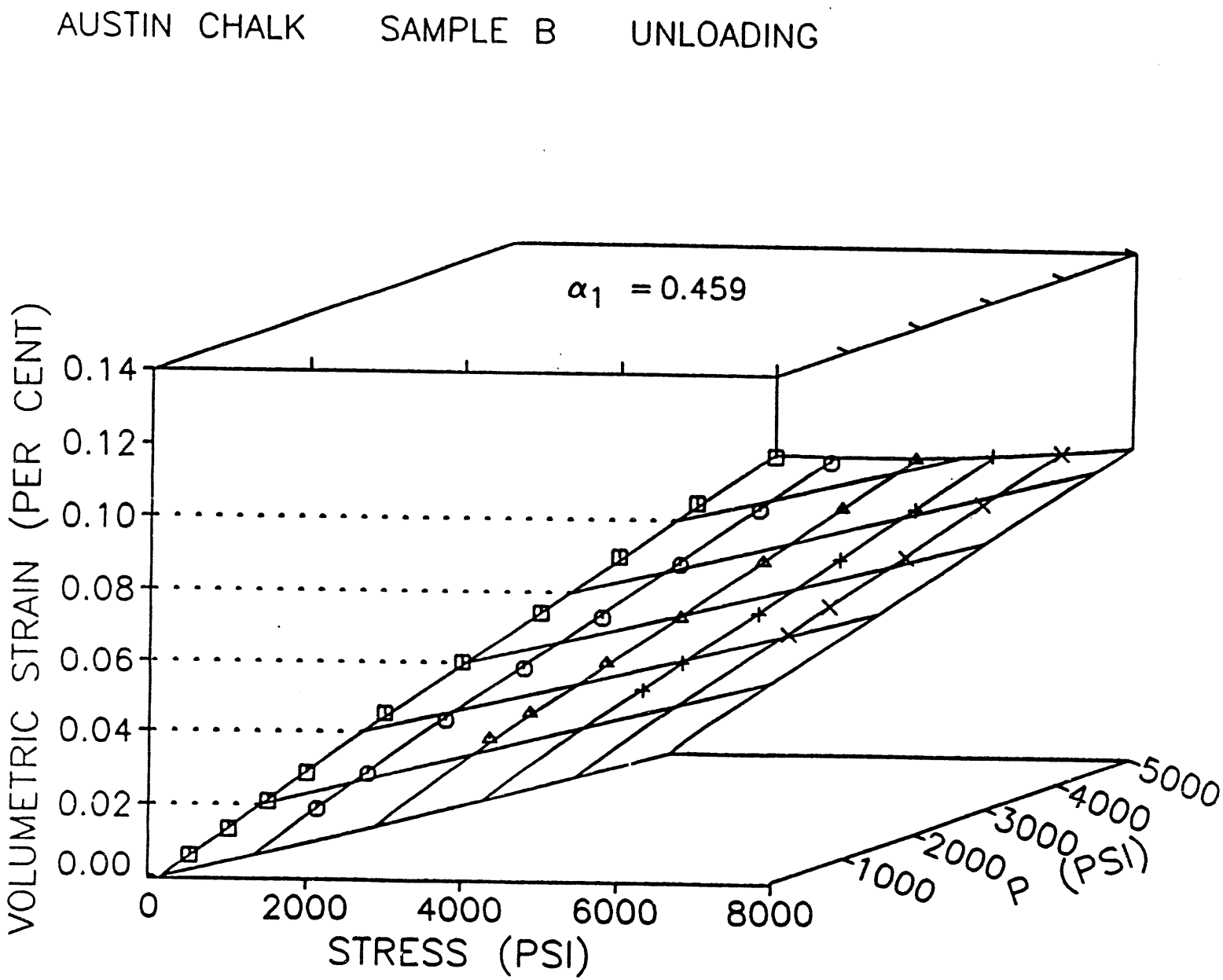

Figure 7 **Response surface, sample B, unloading**

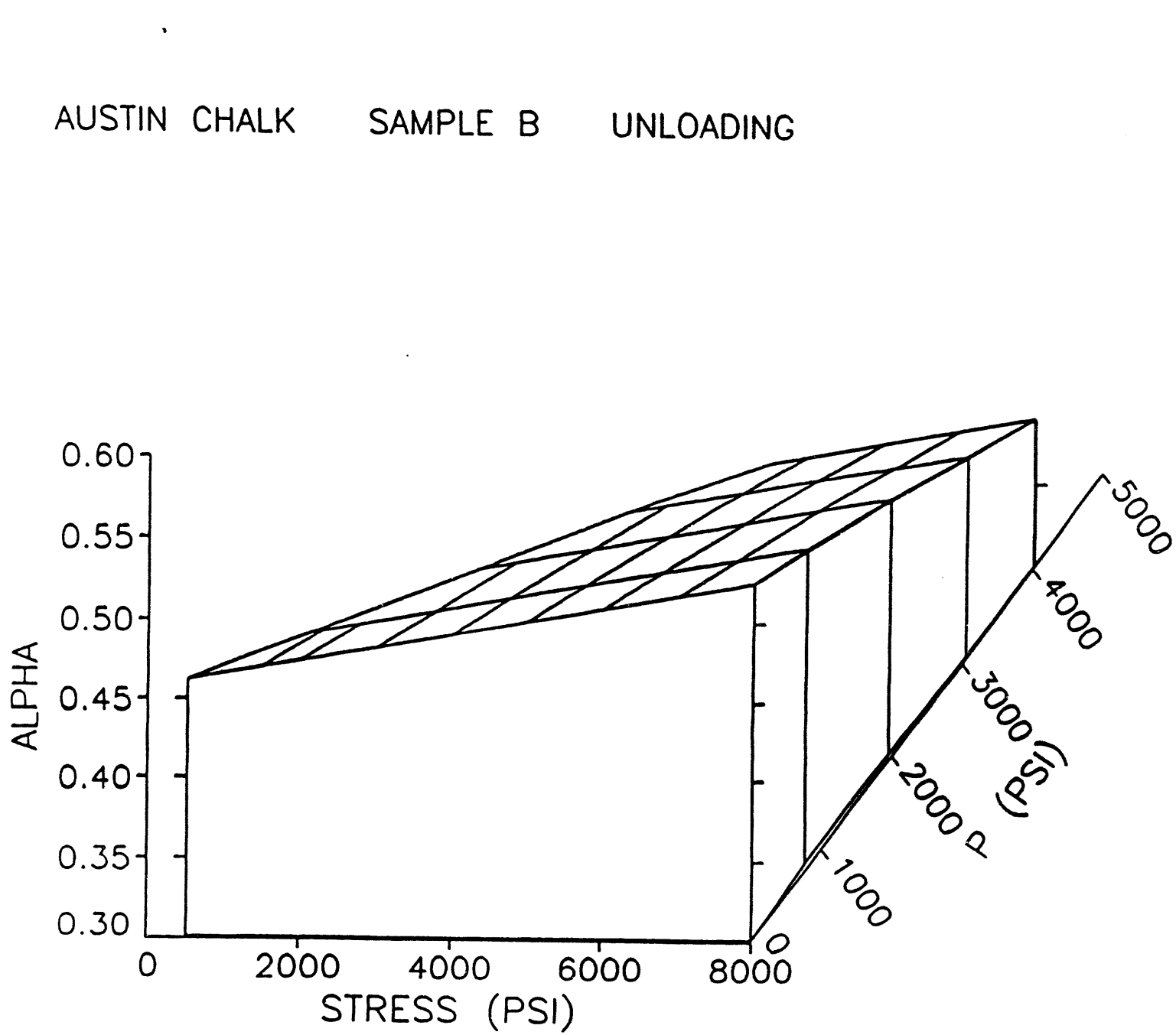

Figure 8 **α surface, sample B, unloading**

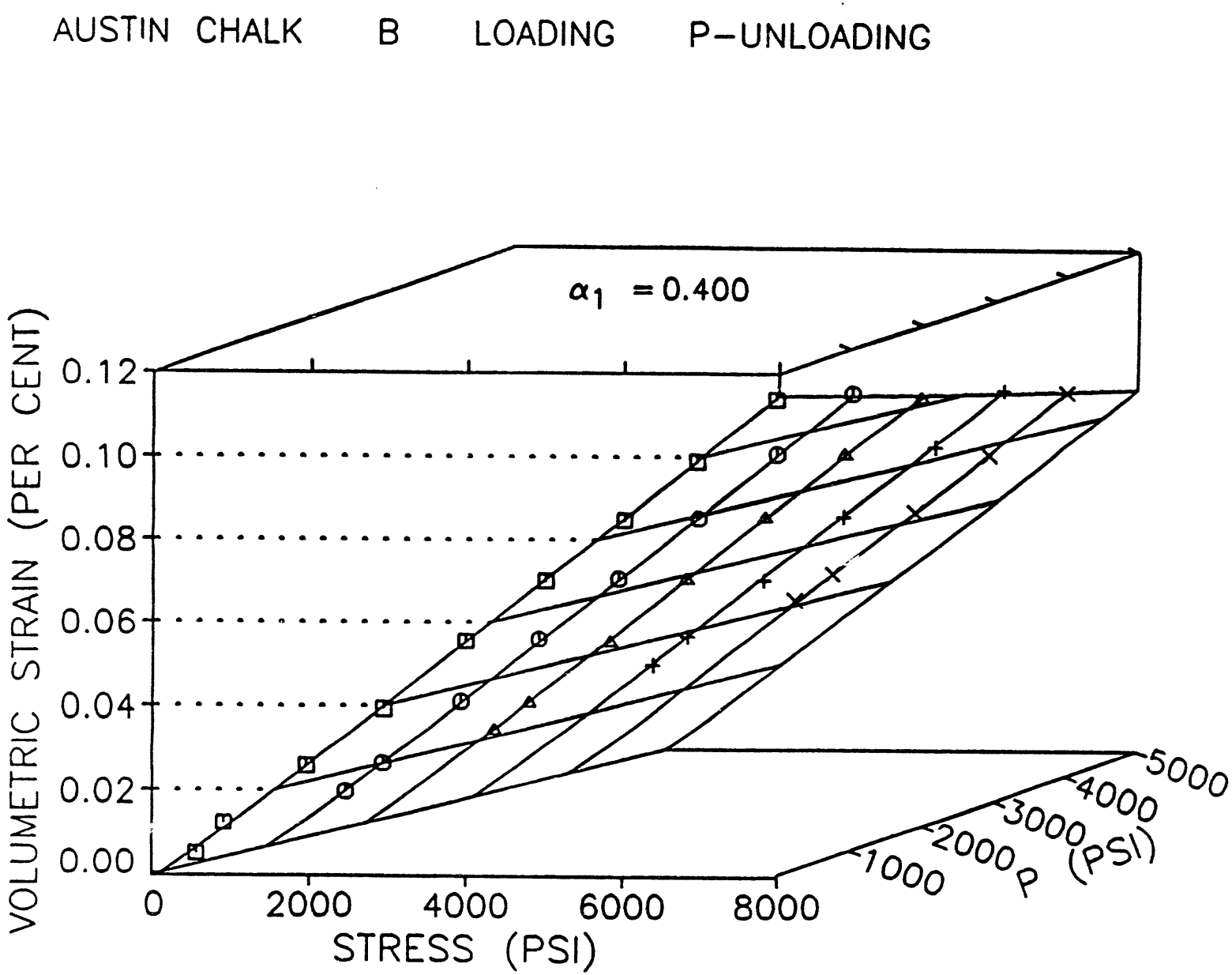

Figure 9 **Response surface, sample B, stress loading, pore pressure, unloading**

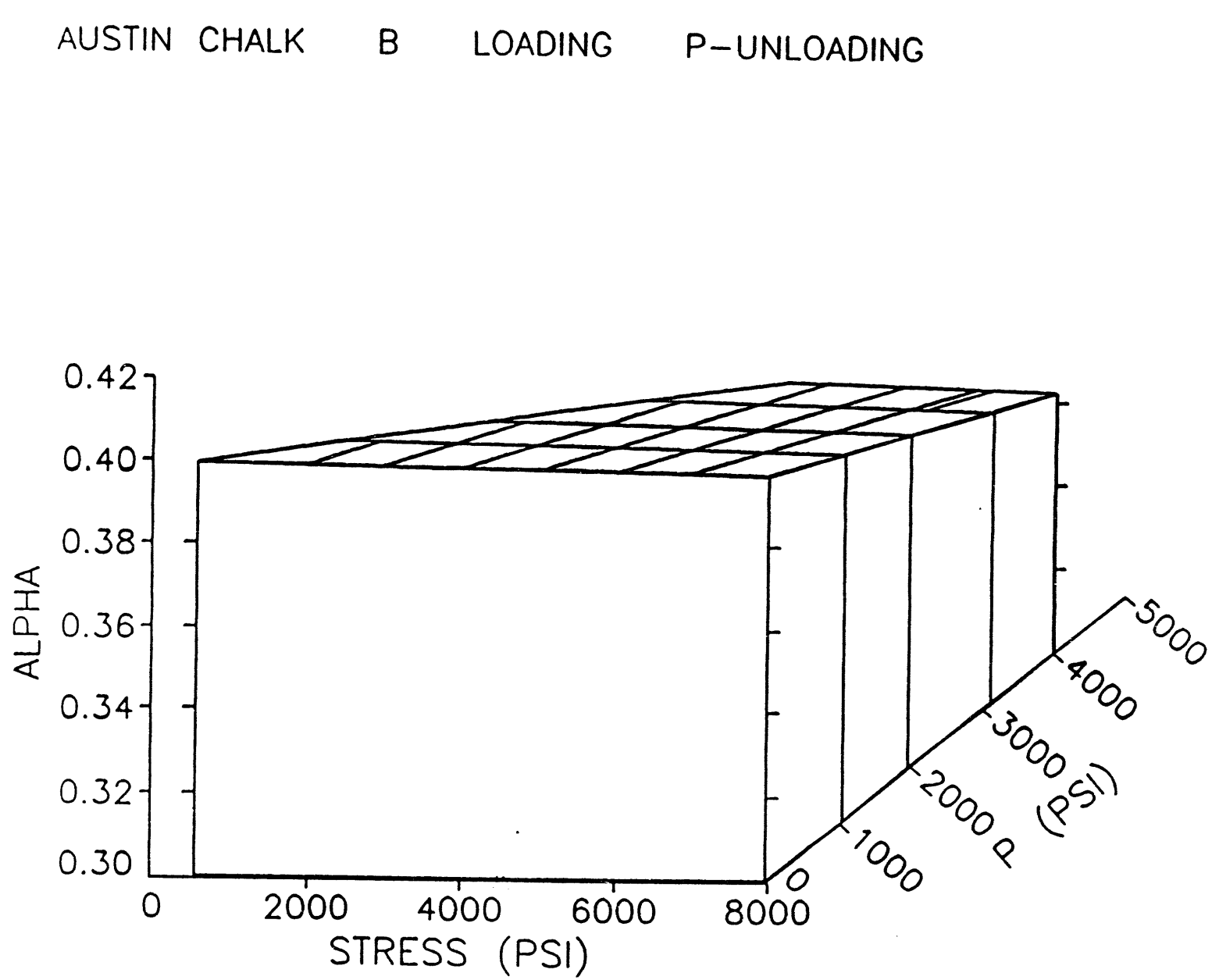

Figure 10 α surface, sample B, stress loading, pore pressure unloading

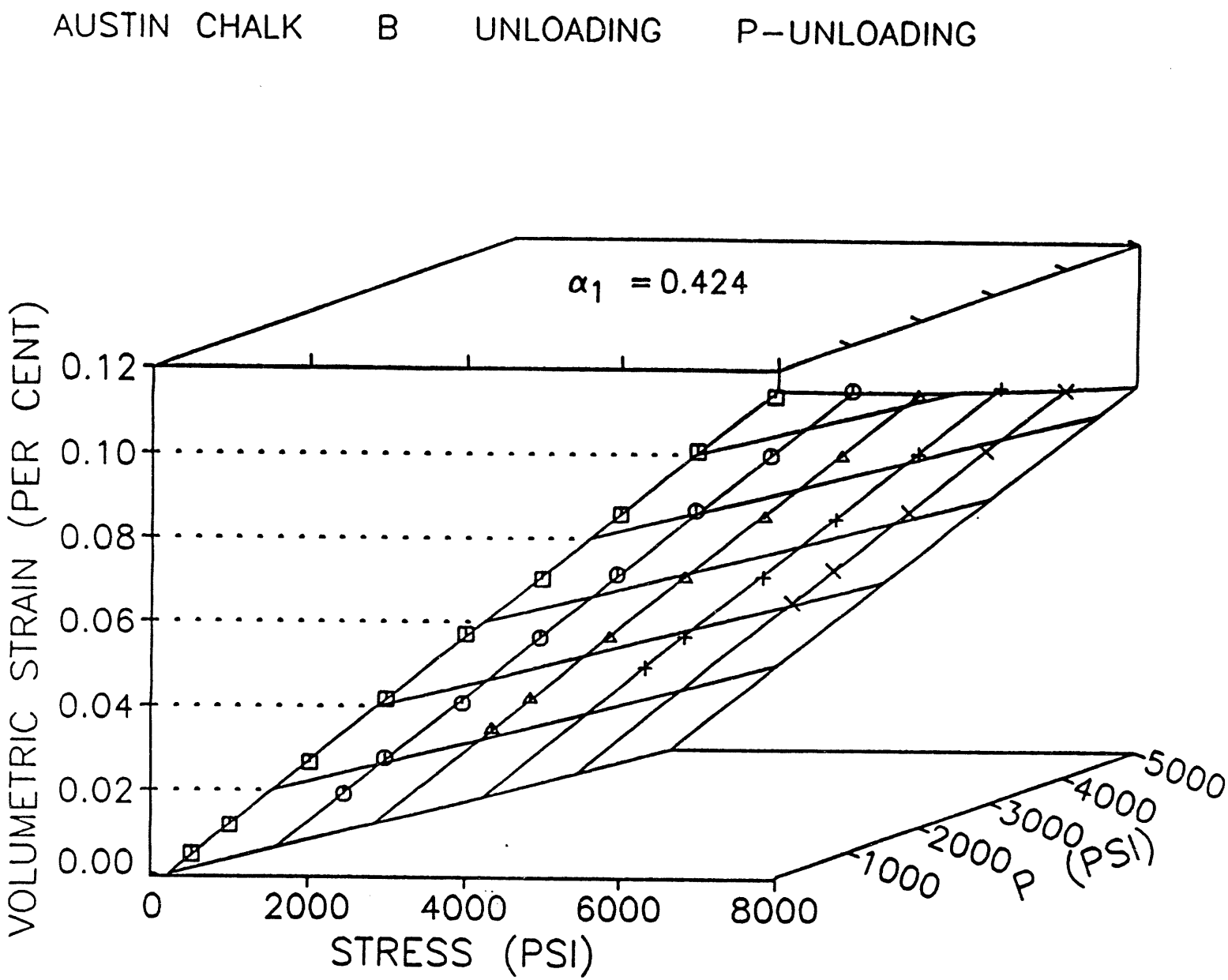

Figure 11 Response surface, sample B, stress unloading, pore pressure unloading

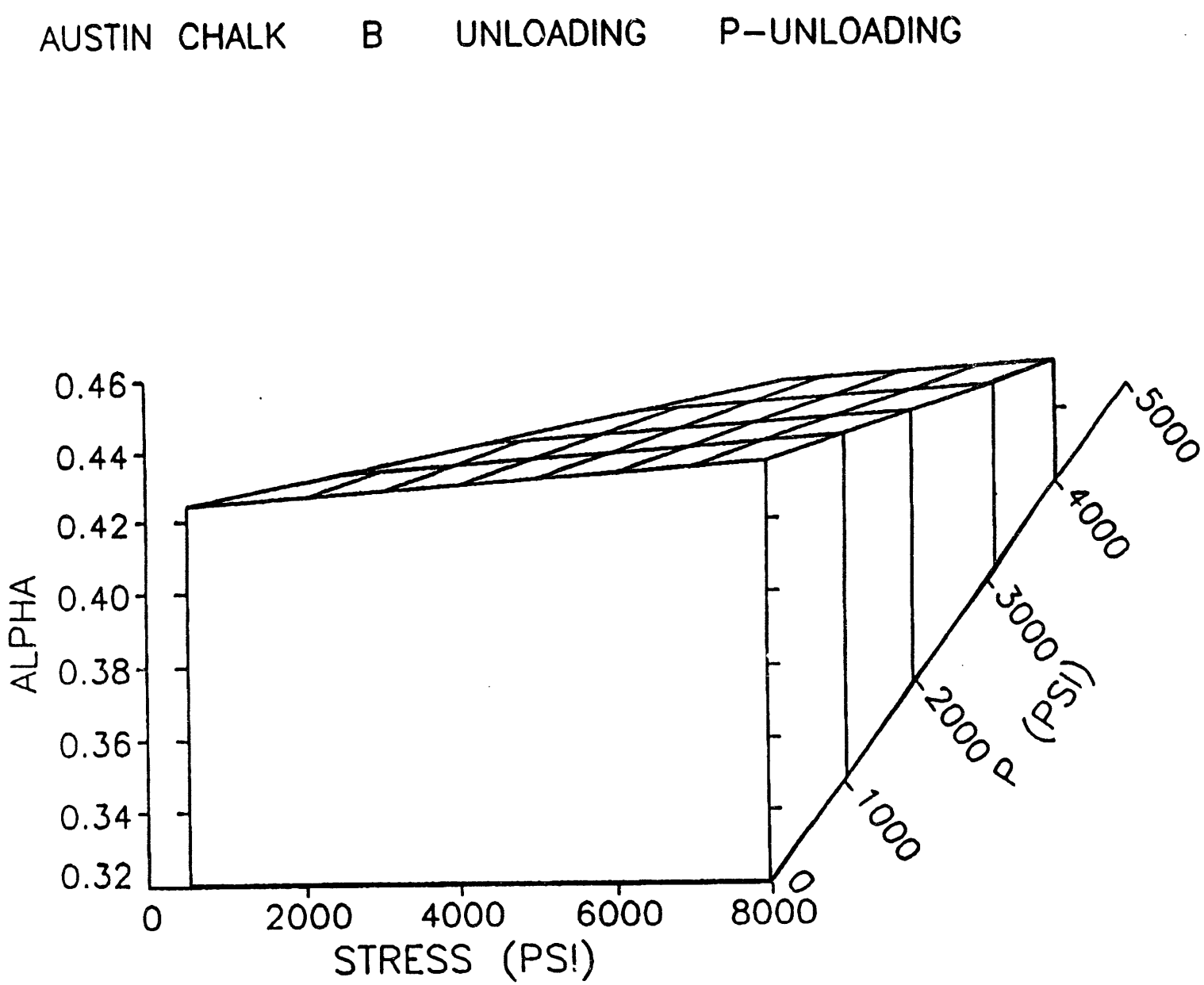

Figure 12 α surface, sample B, stress unloading, pore pressure unloading

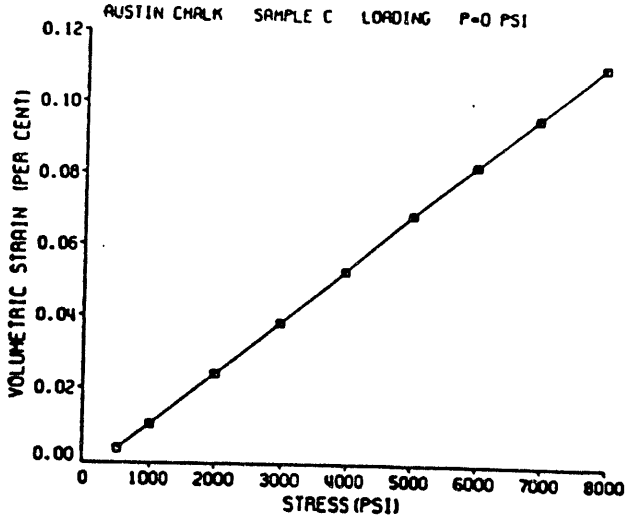

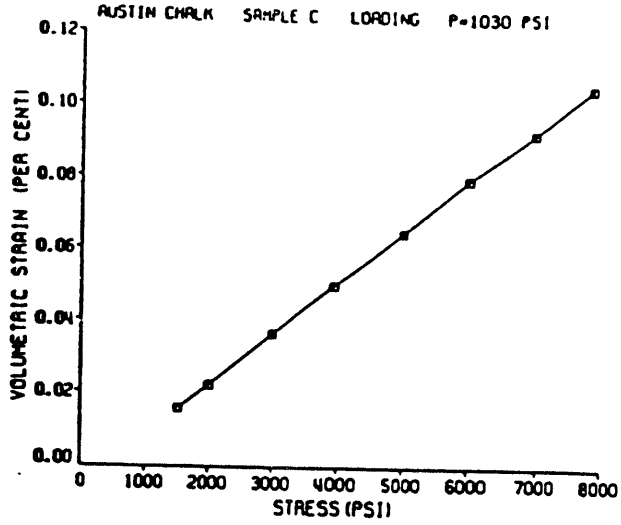

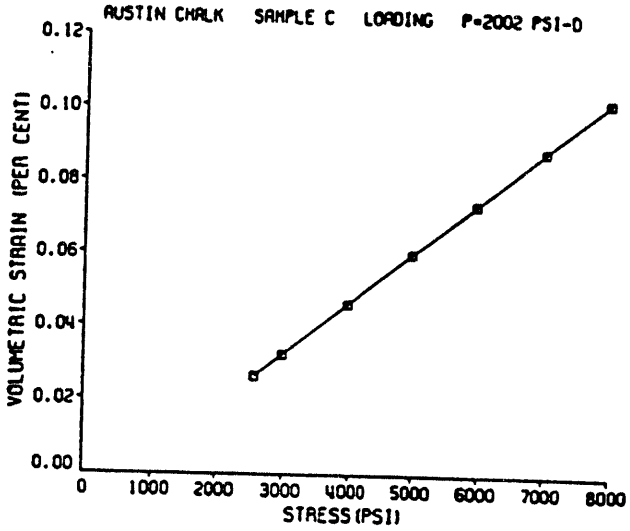

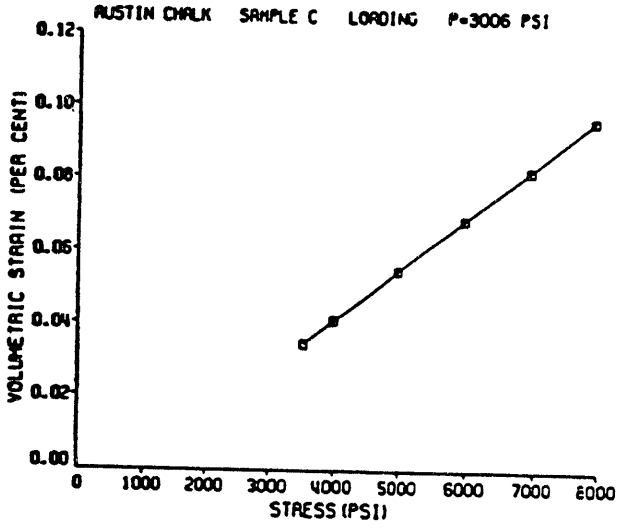

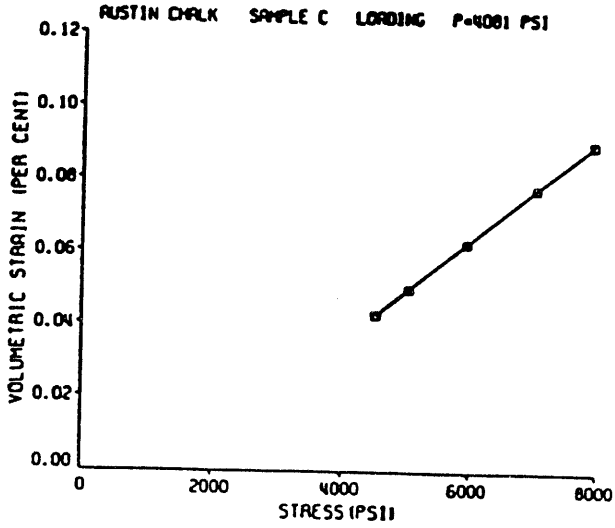

Figure 13 Volumetric strain data, sample C, loading

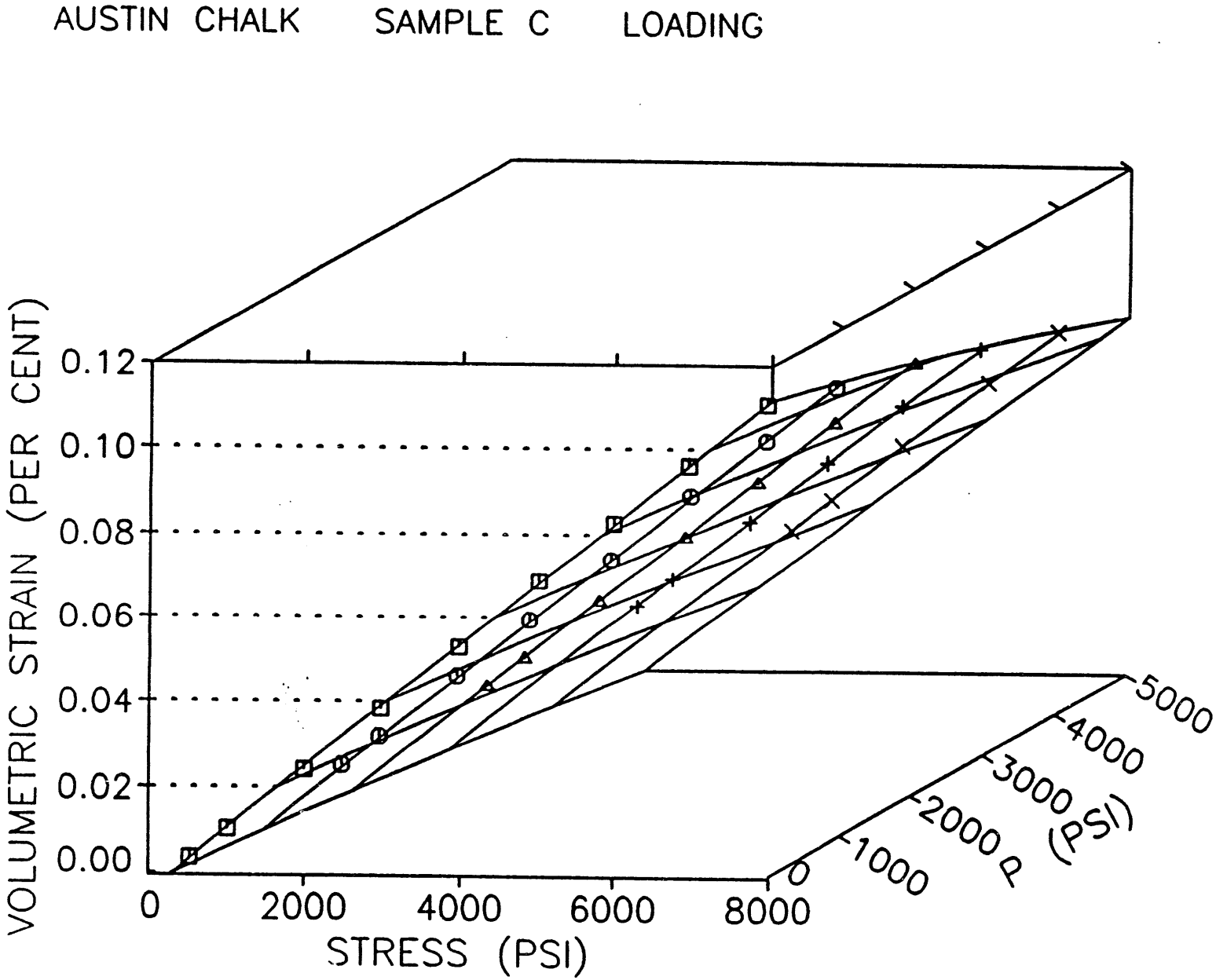

Figure 14 Response surface, sample C, loading

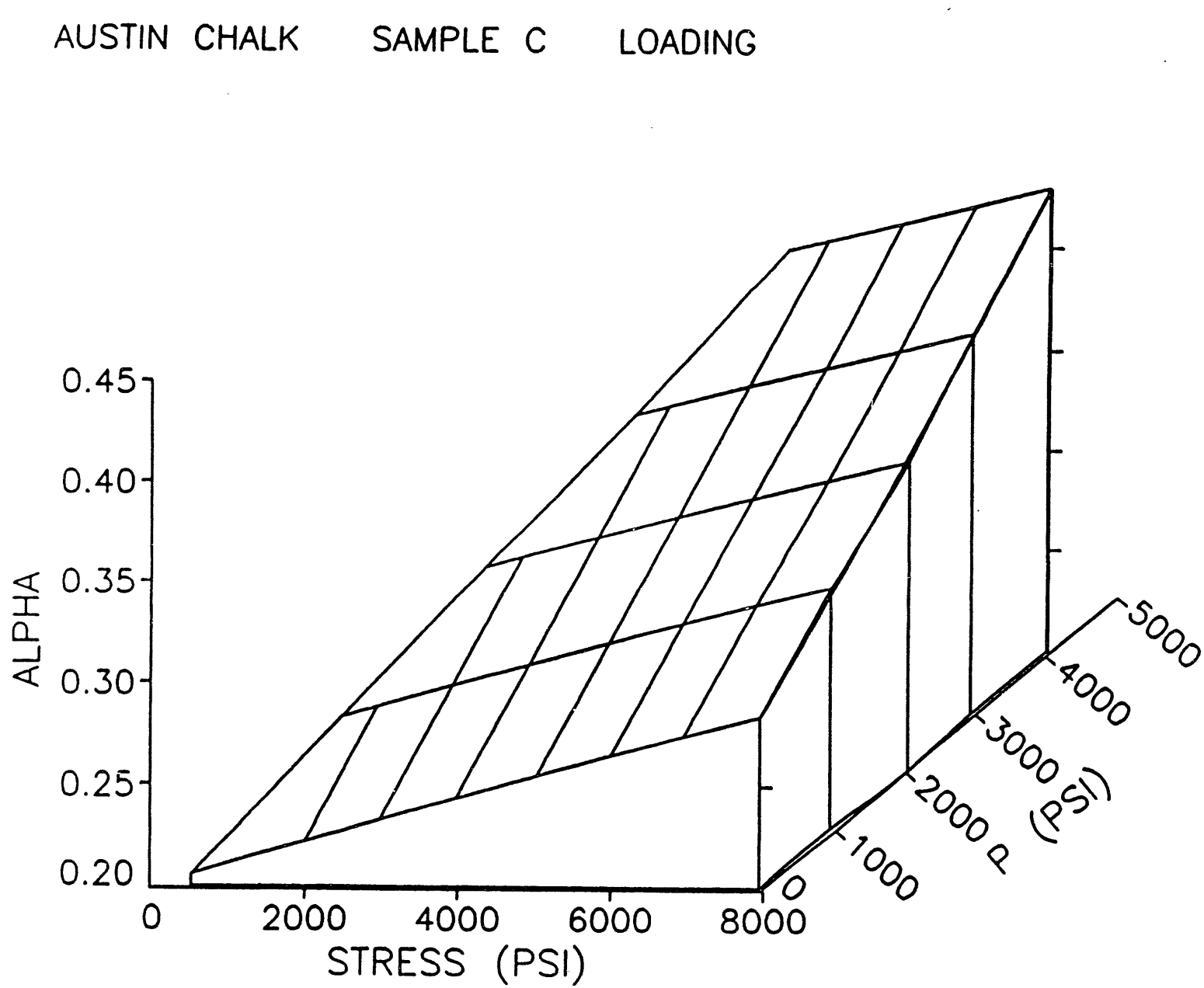

Figure 15 α surface, sample C, loading

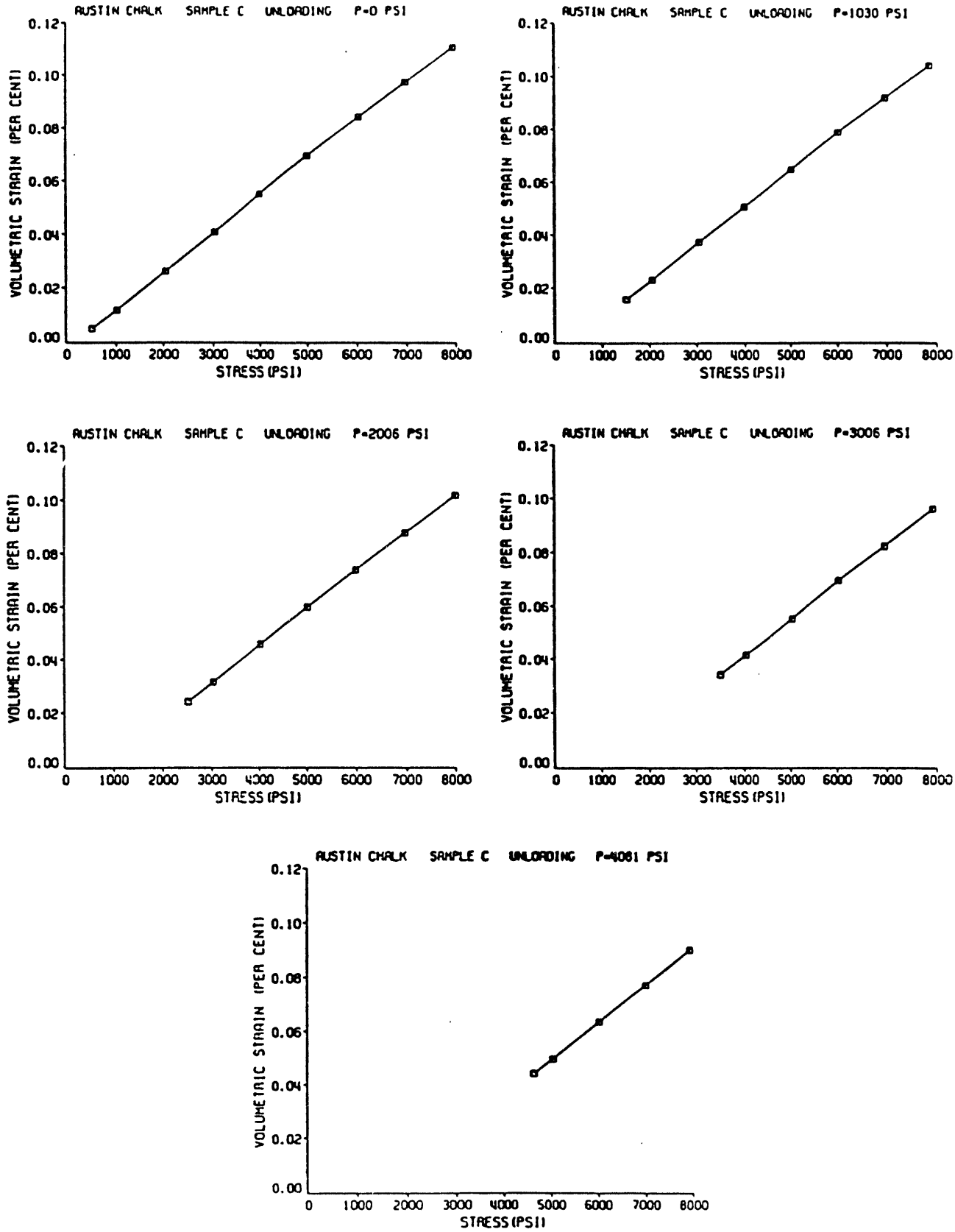

Figure 16 Volumetric strain data, sample C, unloading

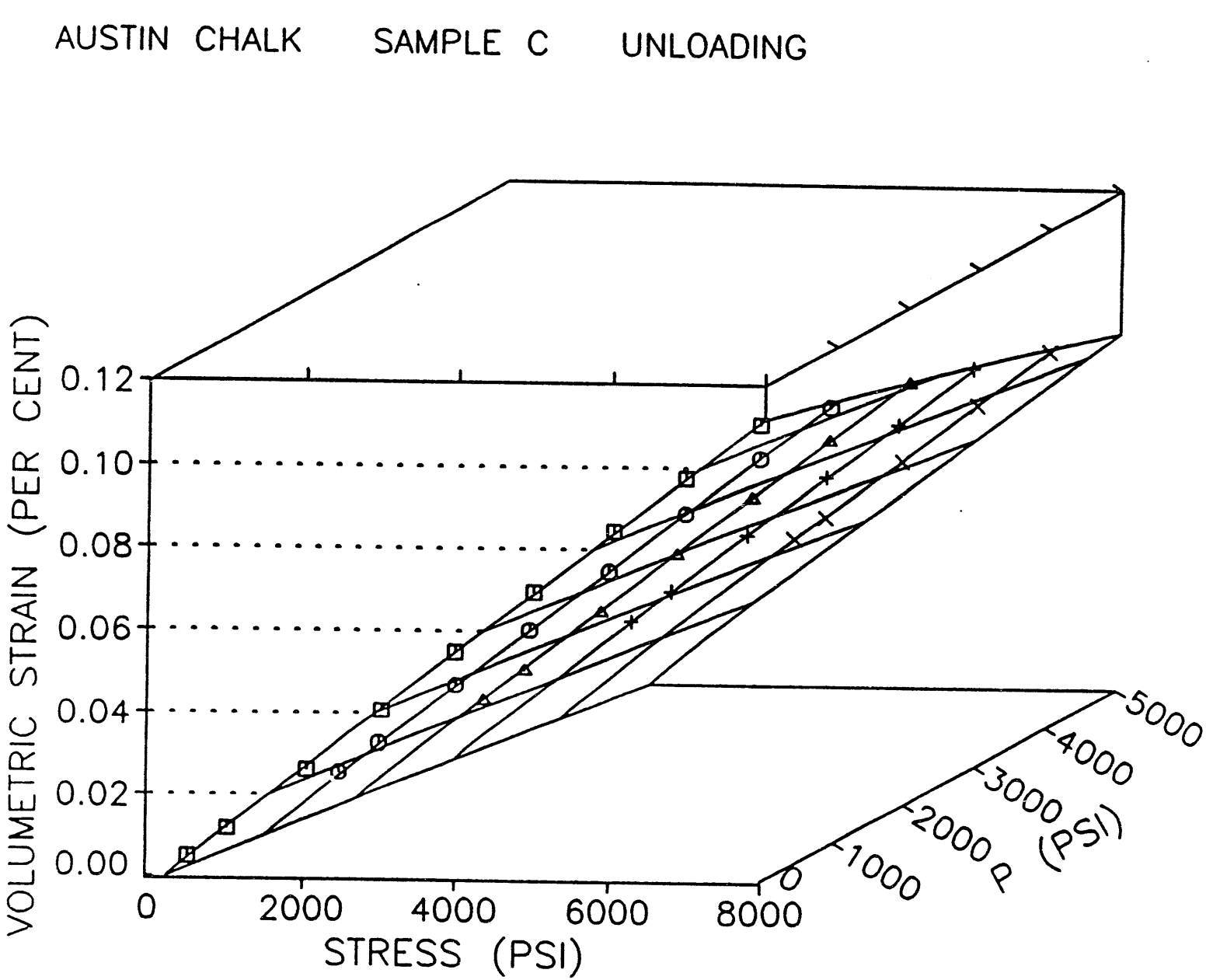

Figure 17 Response surface, sample C, unloading

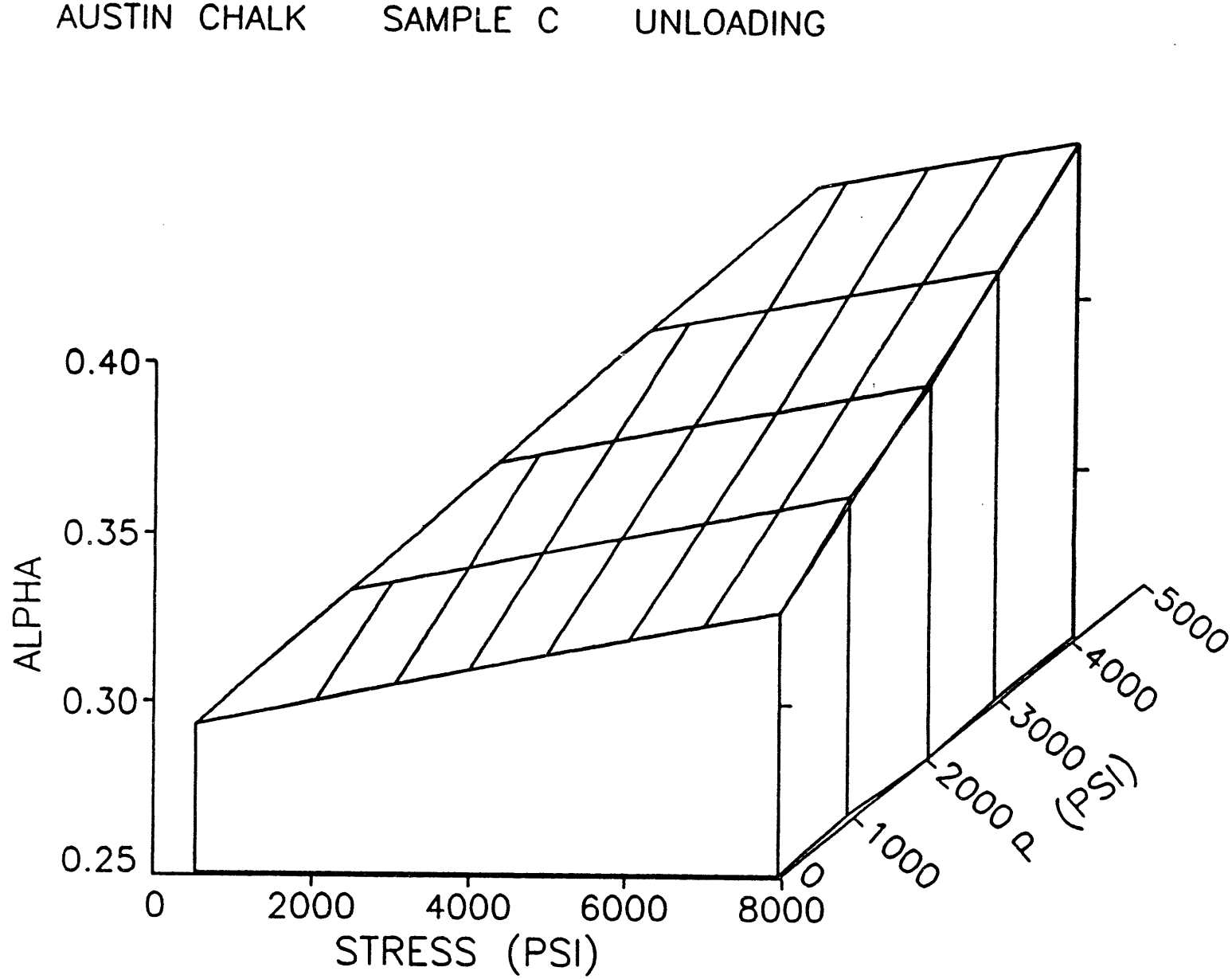

Figure 18 α surface, sample C, unloading

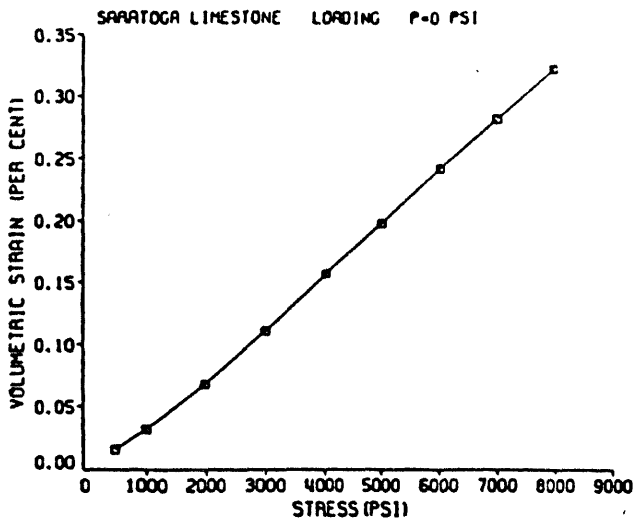

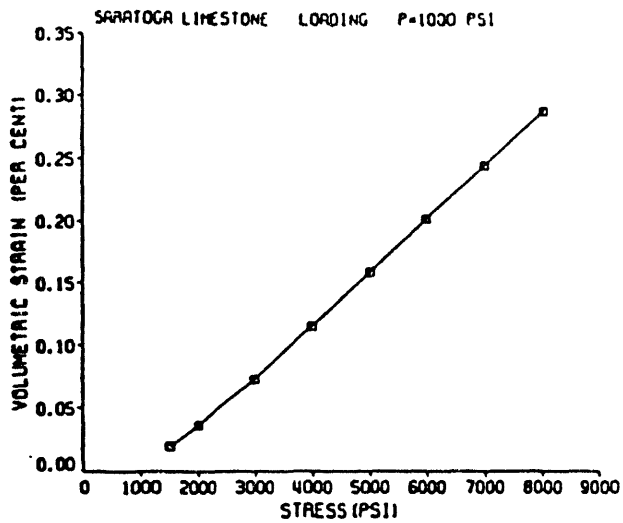

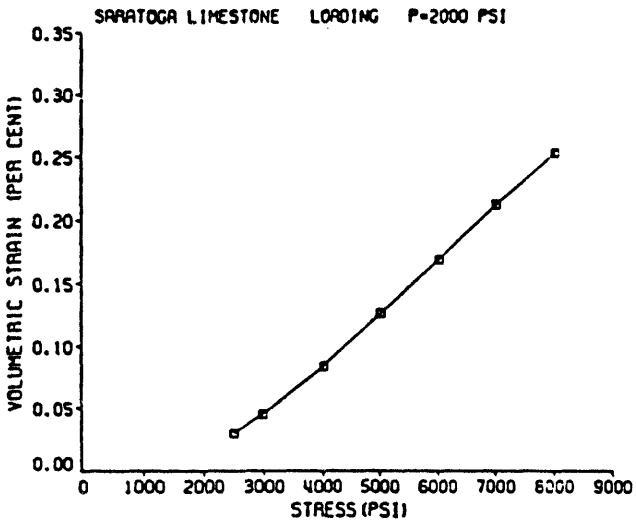

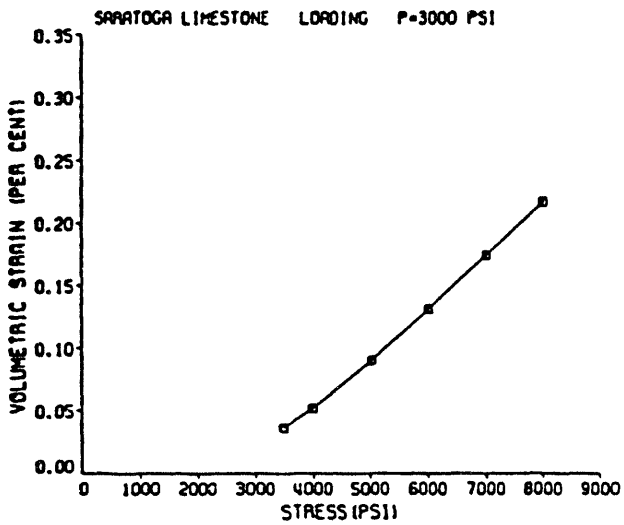

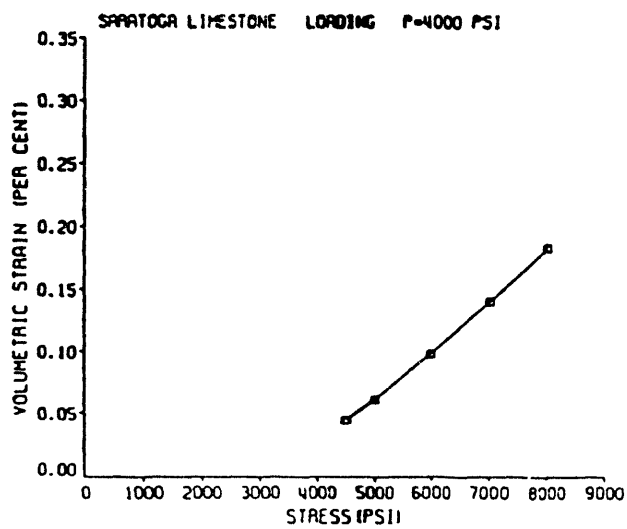

Figure 19 Volumetric strain data, Saratoga limestone, loading

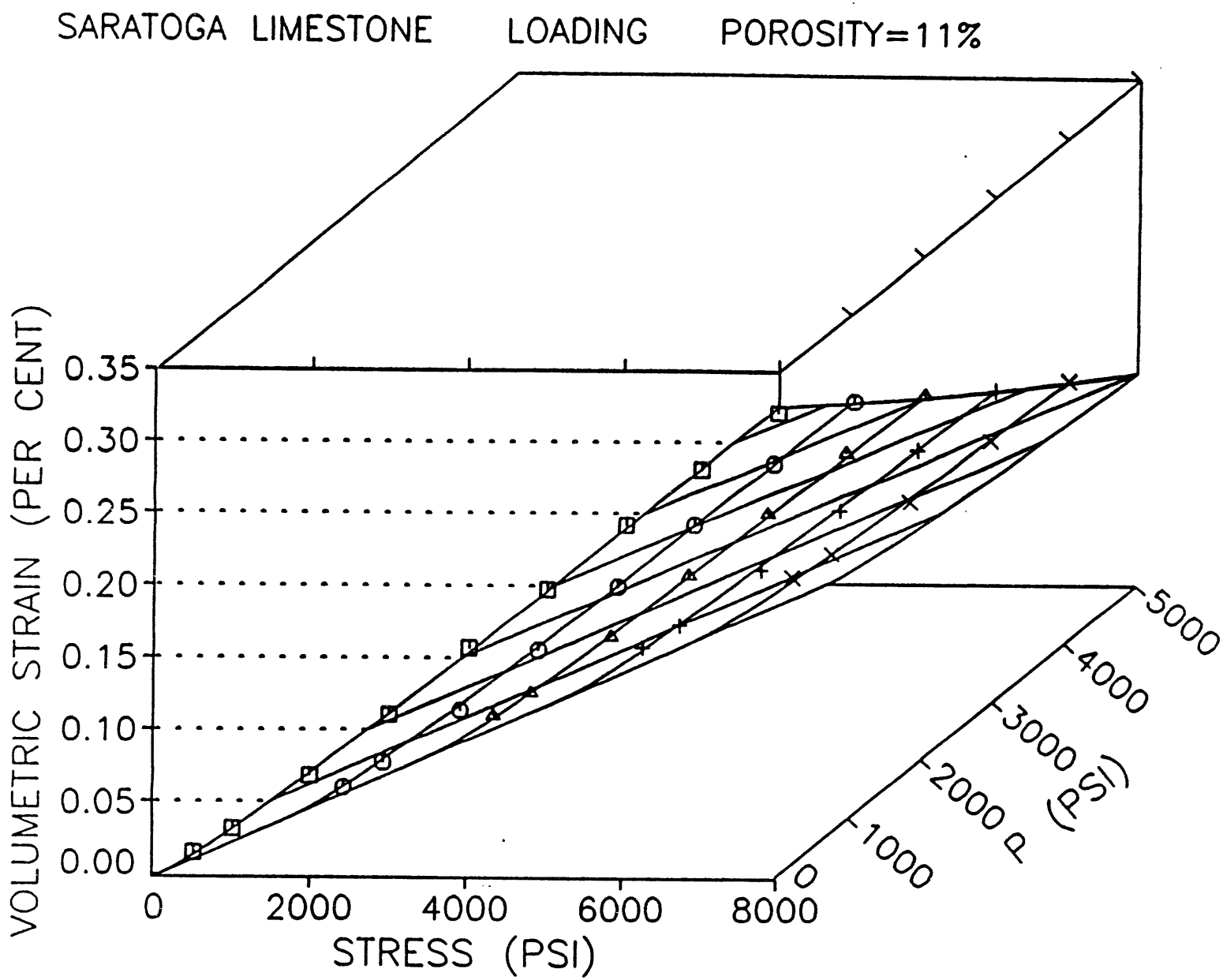

Figure 20 Response surface, Saratoga limestone, loading

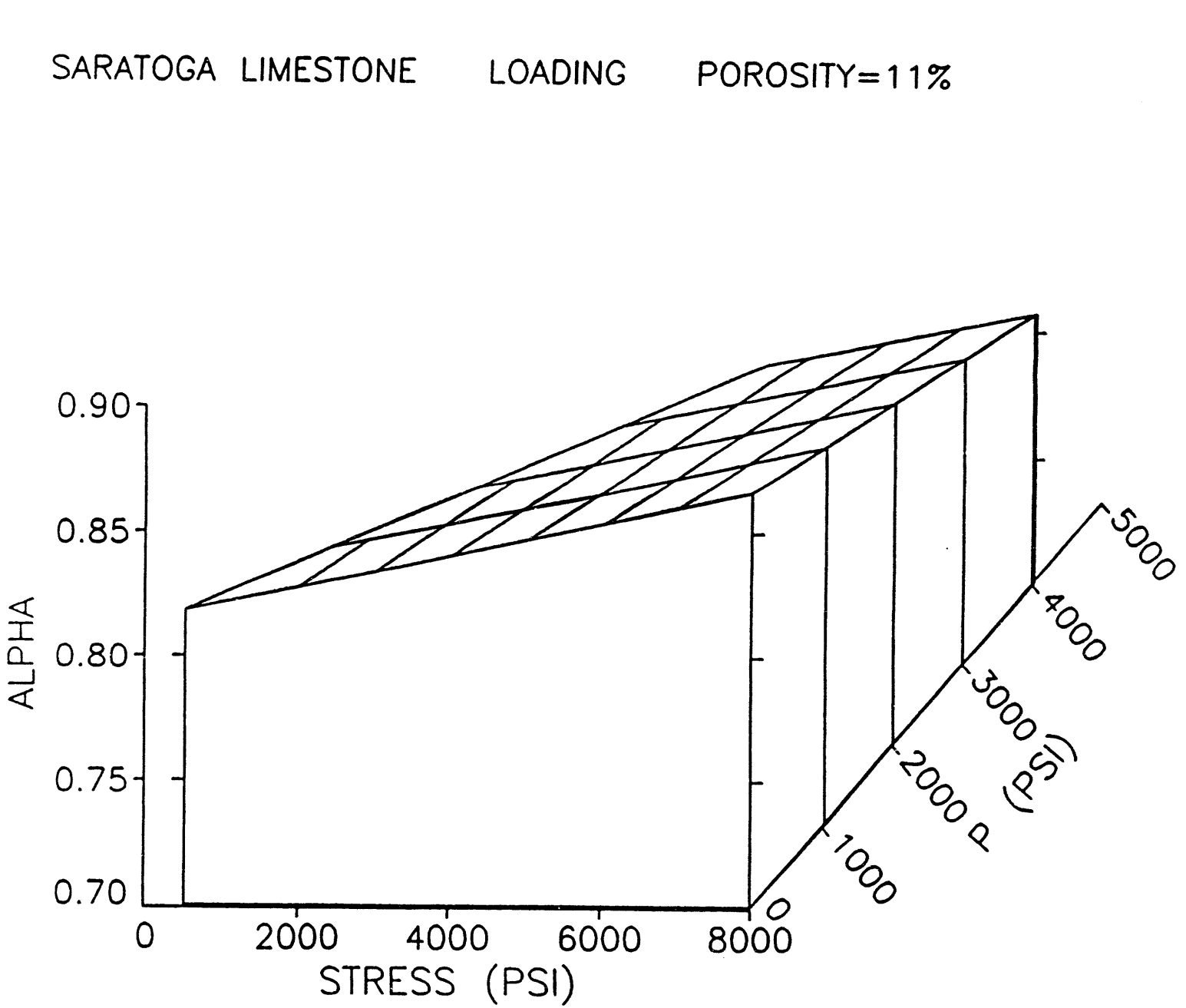

Figure 21 α **surface, Saratoga limestone, loading**

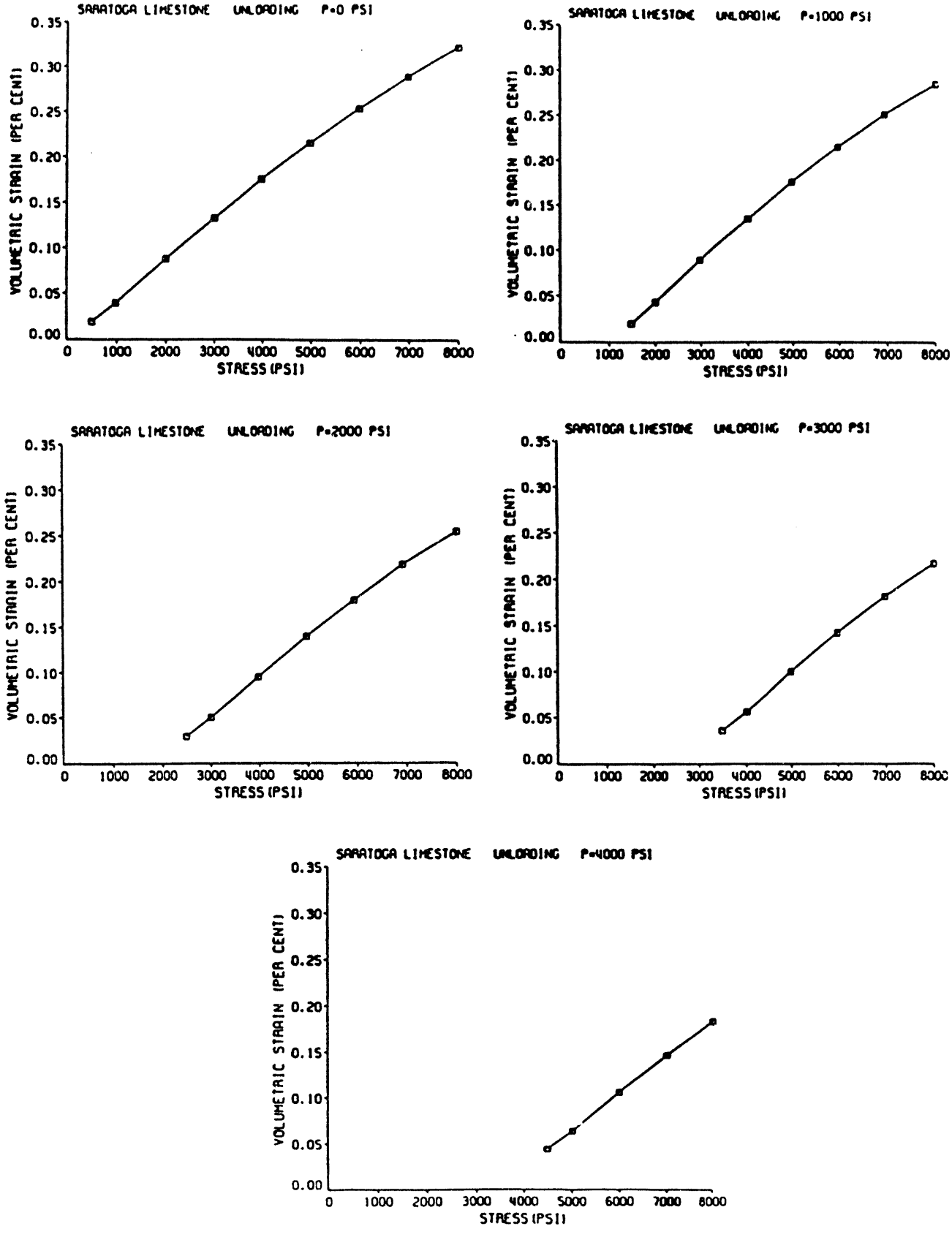

Figure 22 Volumetric strain data, Saratoga limestone, unloading

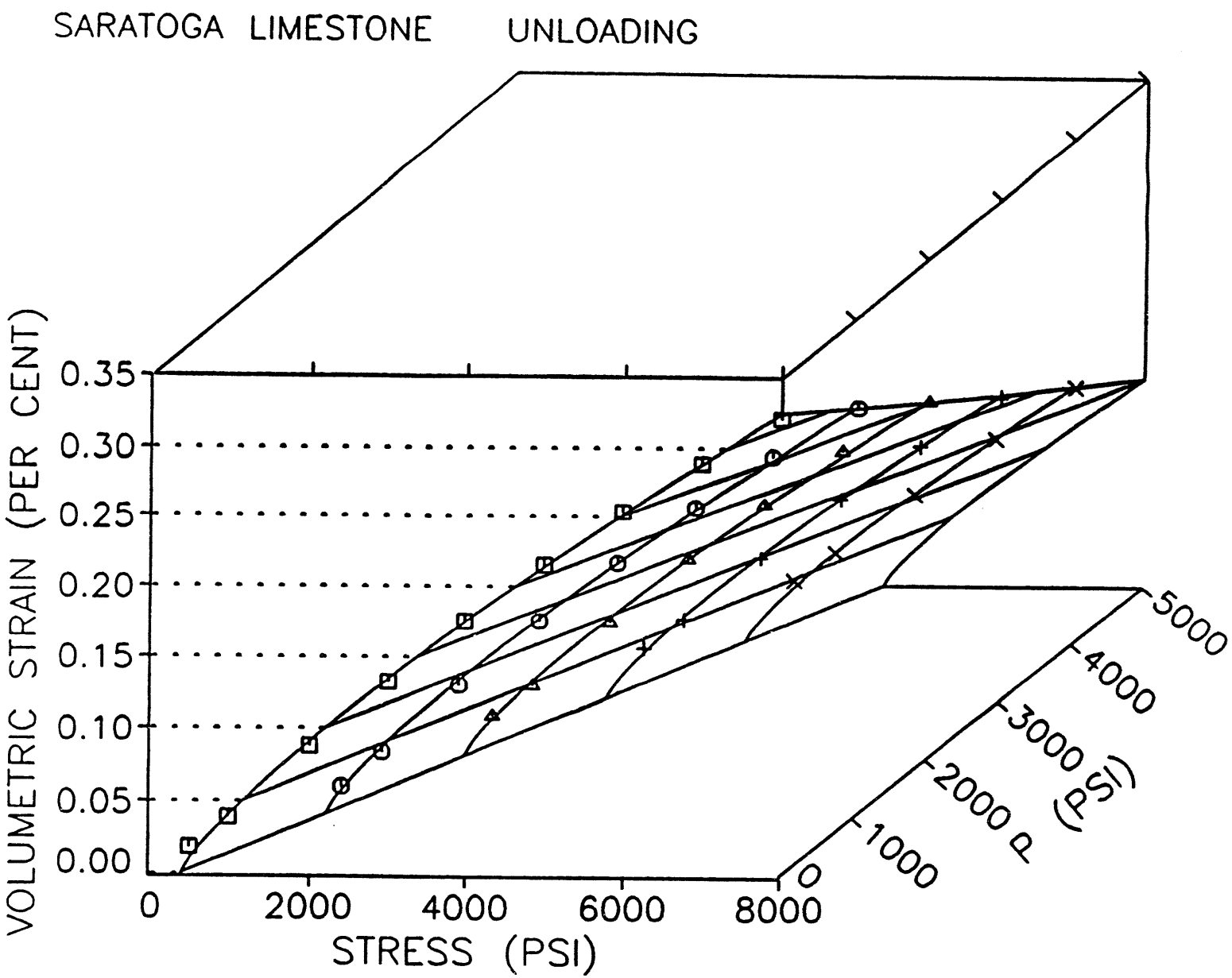

Figure 23 Response surface, Saratoga limestone, unloading

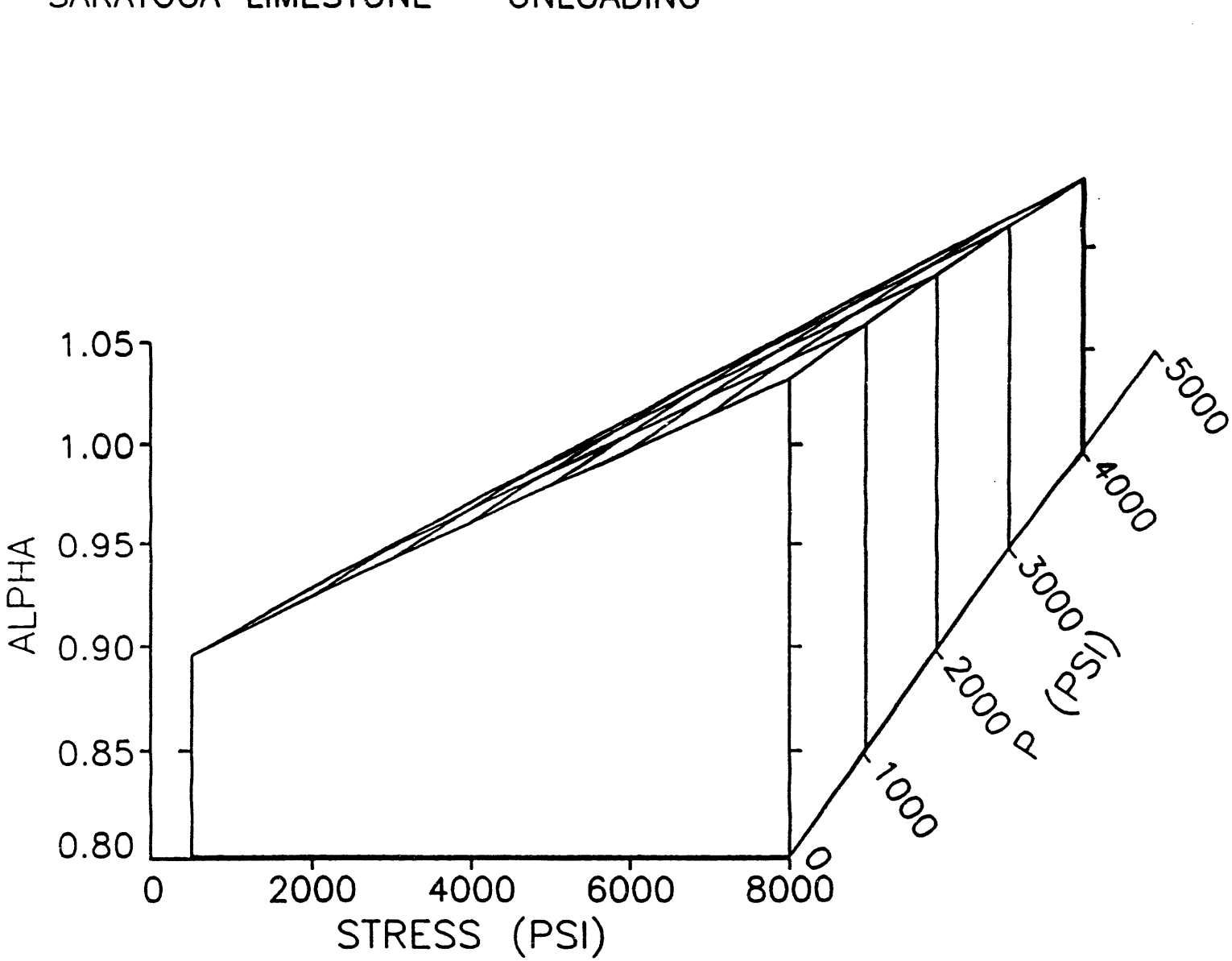

Figure 24 α surface, Saratoga limestone, unloading

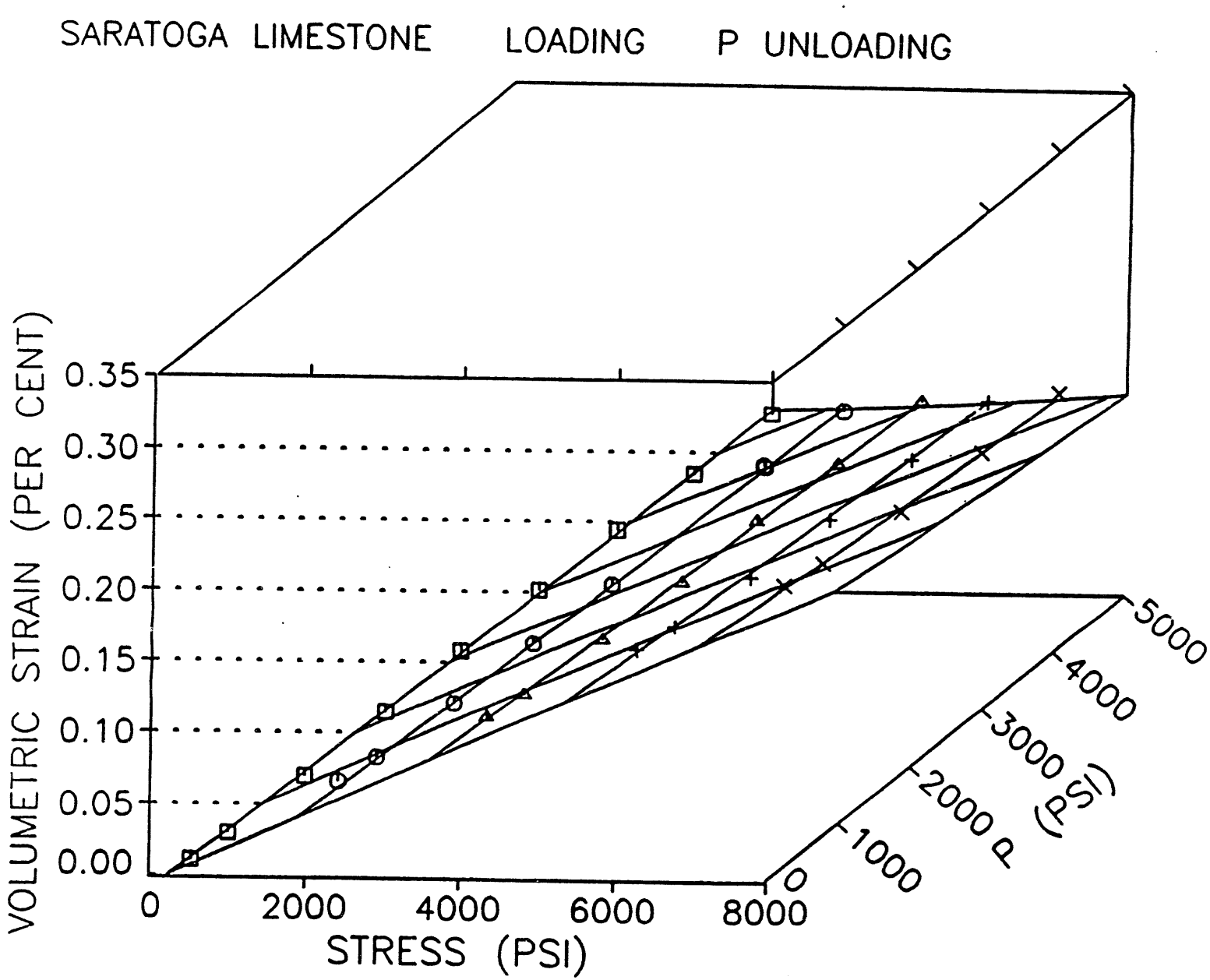

Figure 25 Response surface, Saratoga limestone, stress loading, pore pressure unloading

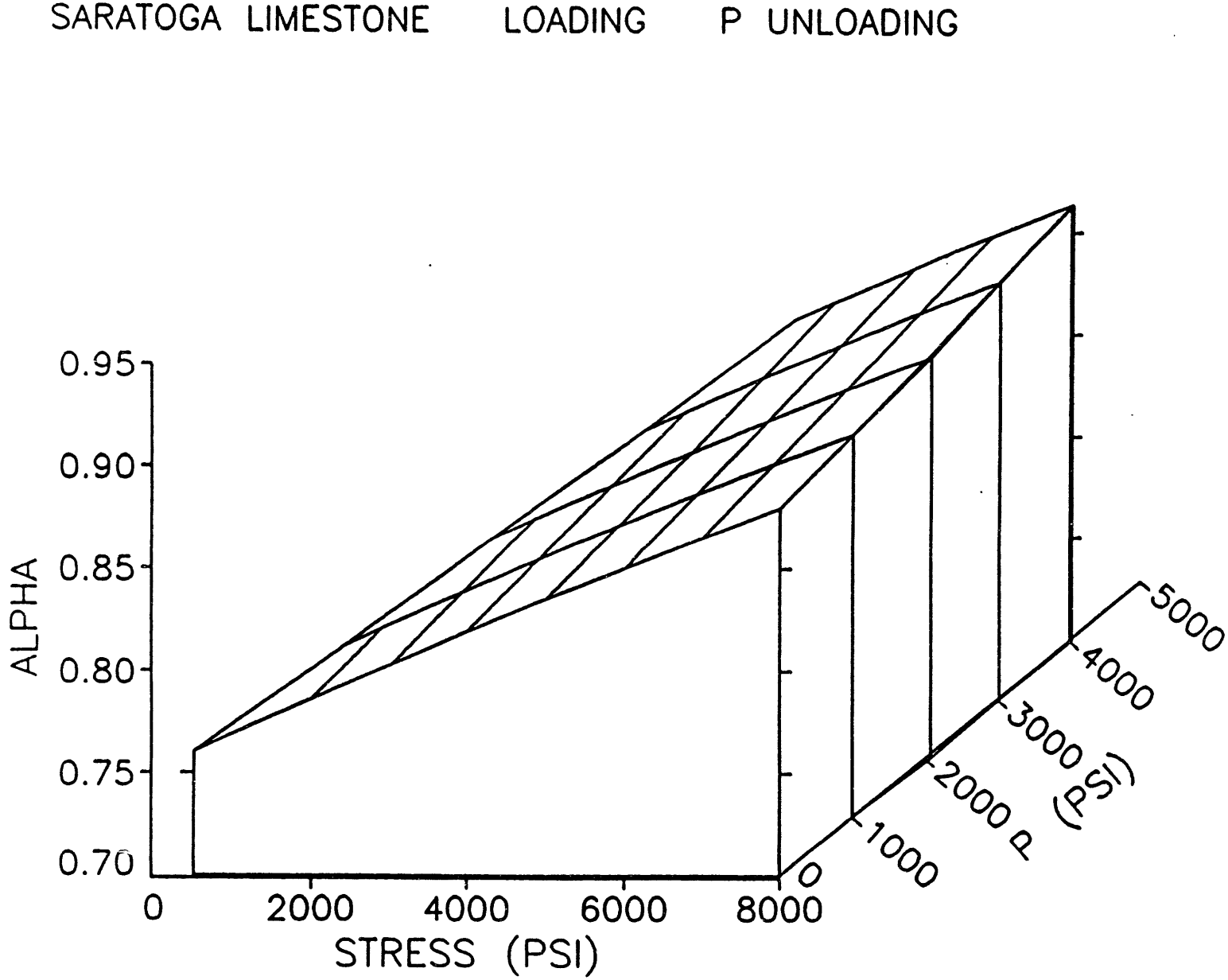

Figure 26 α **surface, Saratoga limestone, stress loading, pore pressure unloading**

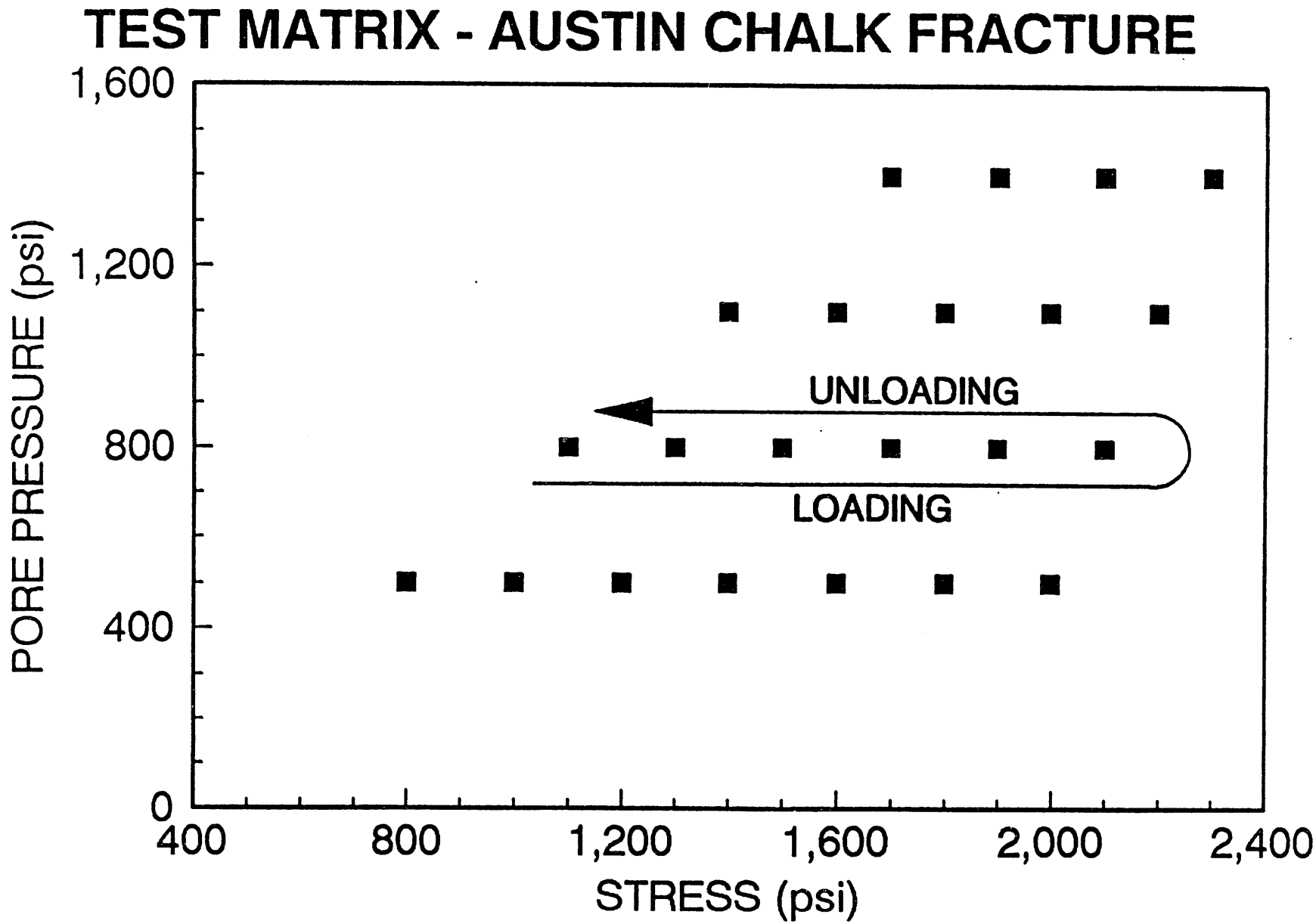

Figure 27 Design matrix, conductivity

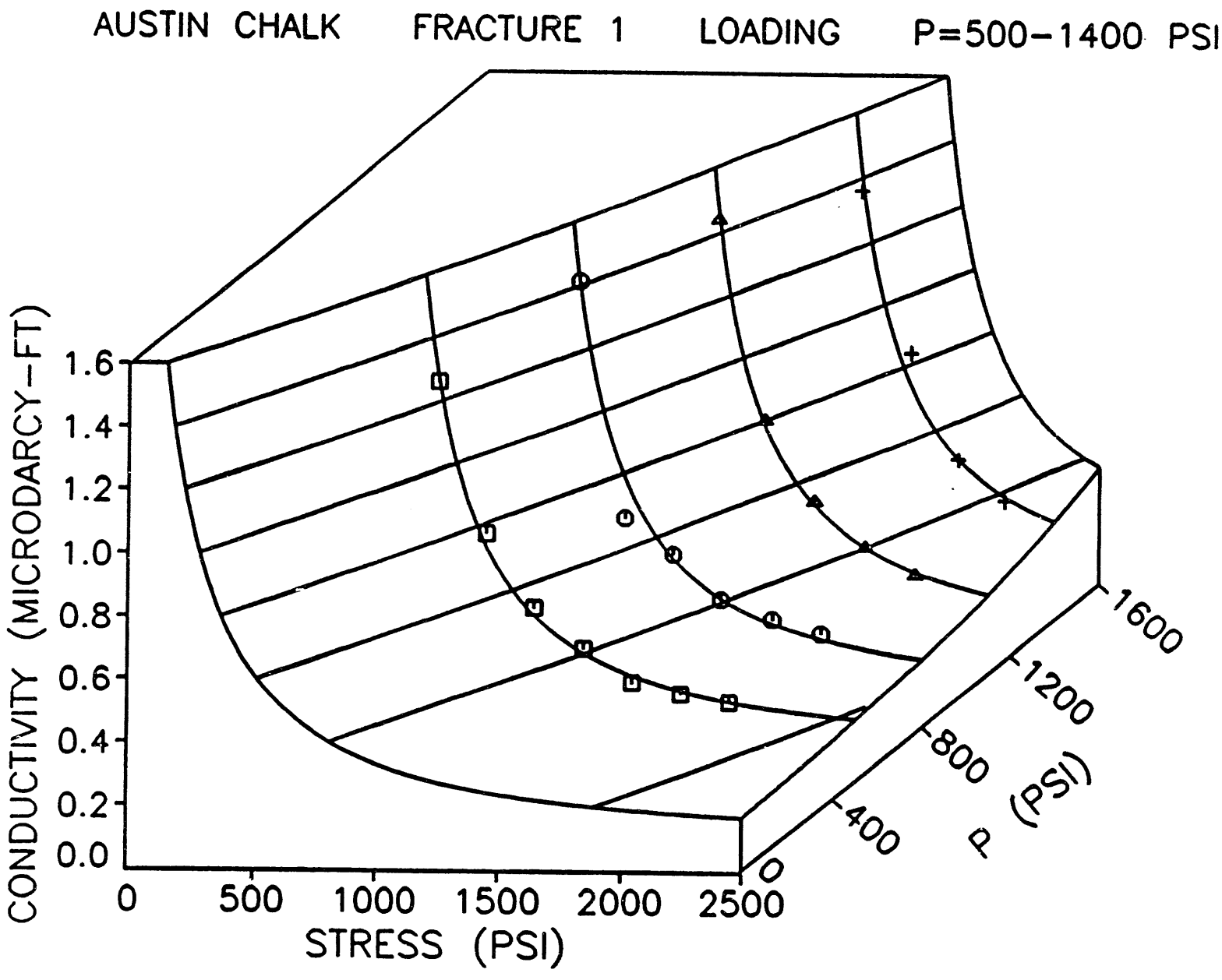

Figure 28 Response surface, fracture 1, loading

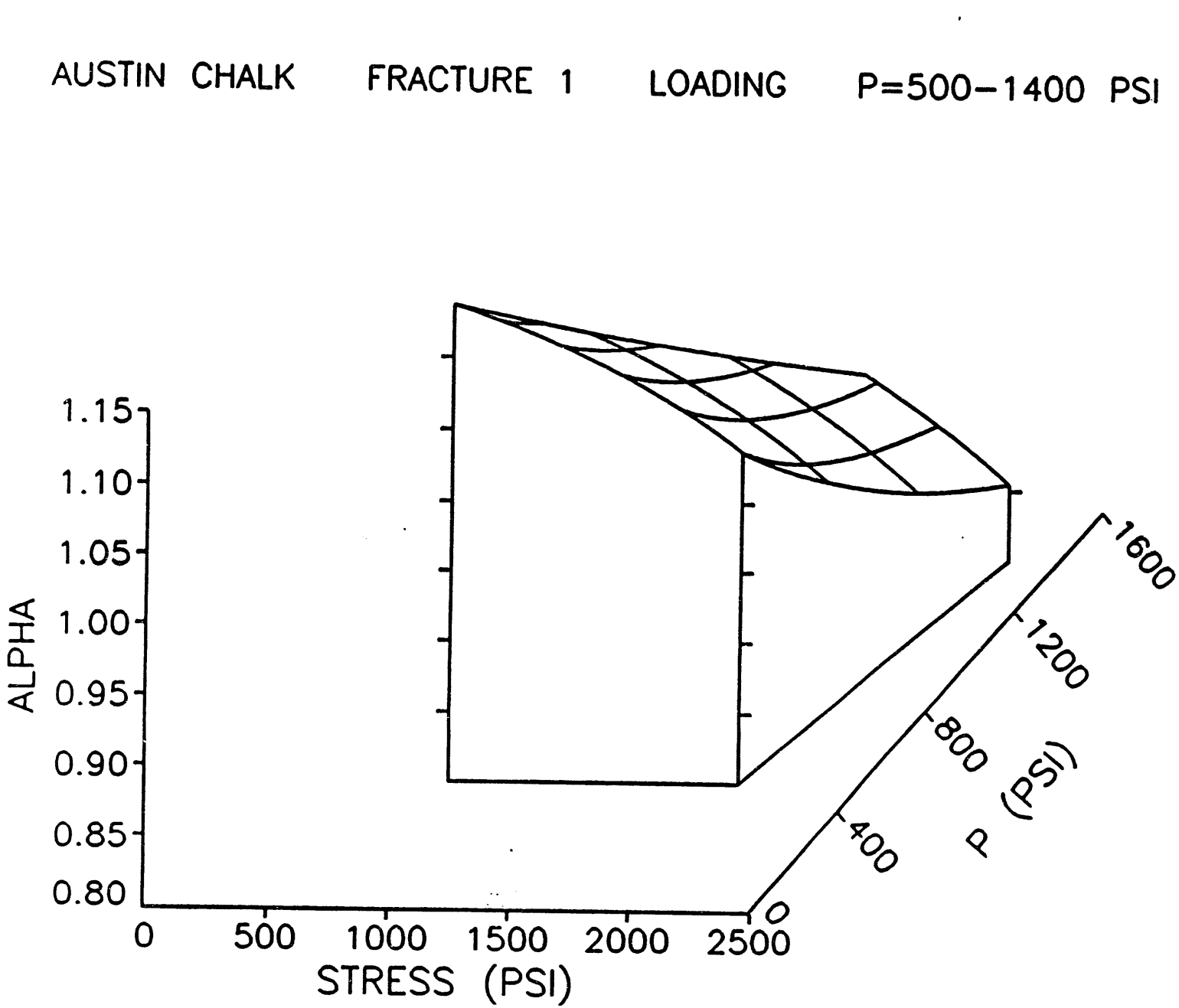

Figure 29 α surface, fracture 1, loading

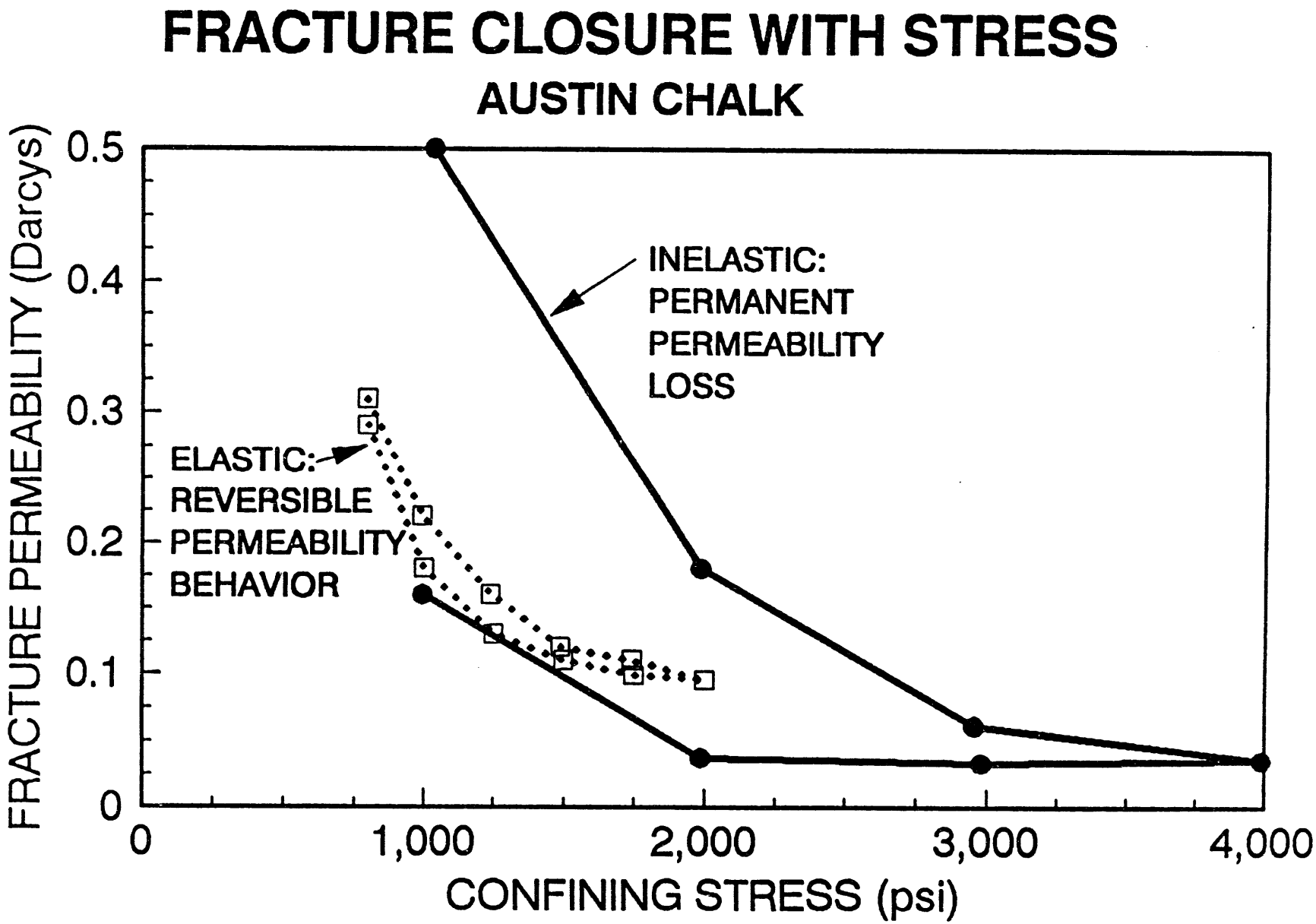

Figure 30 Closure behavior, fracture 1

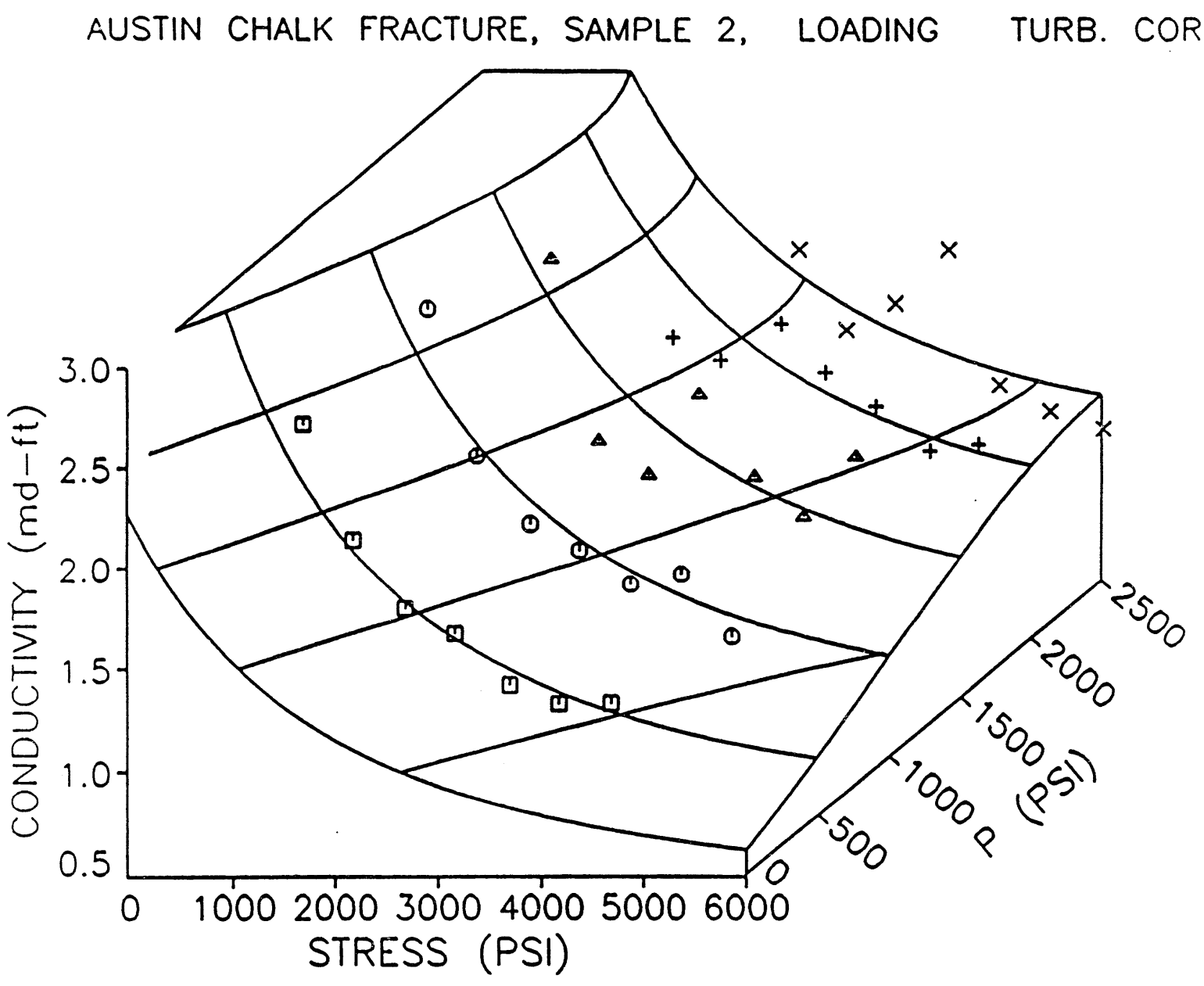

Figure 31 Response surface, fracture 2, loading

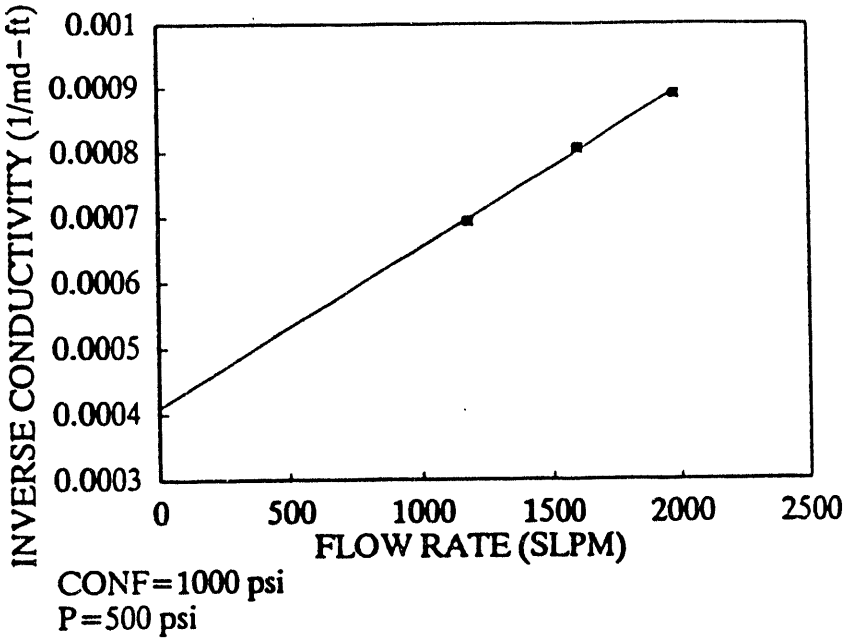

Figure 32 Turbulence data

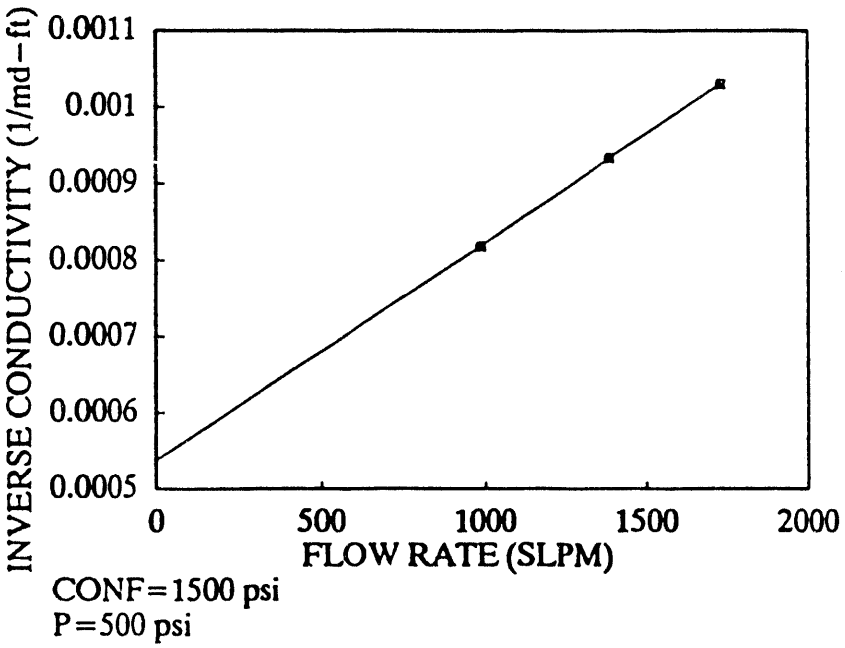

Figure 33 Turbulence data

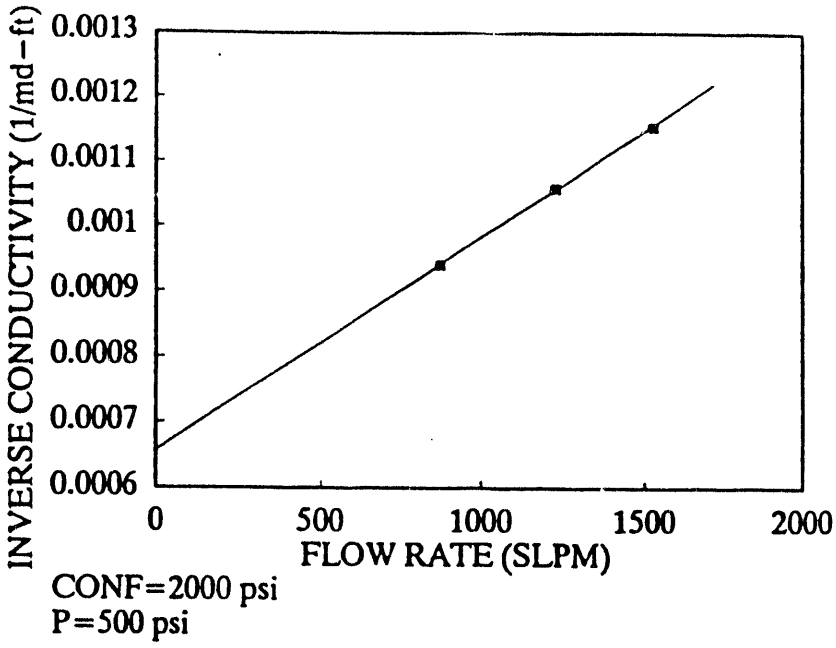

Figure 34 Turbulence data

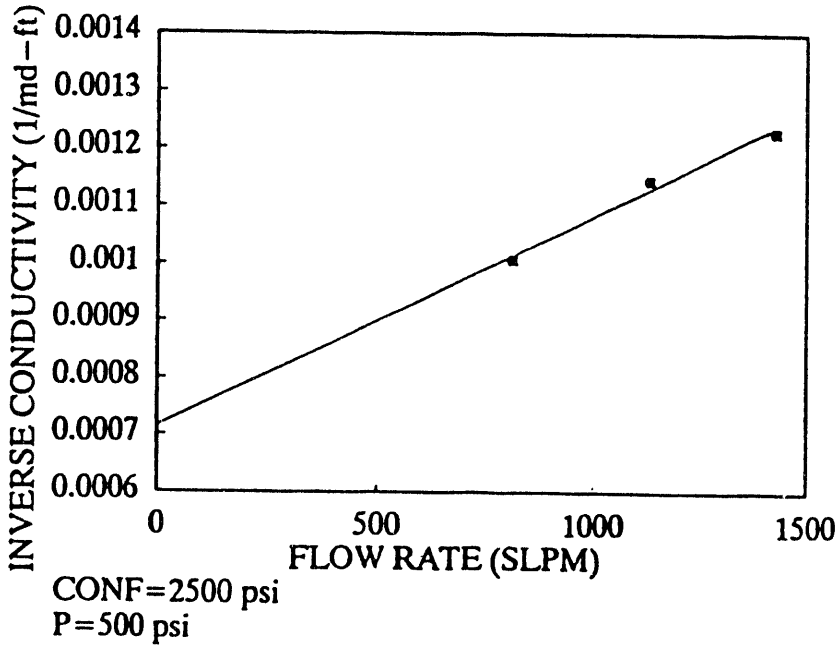

Figure 35 Turbulence data

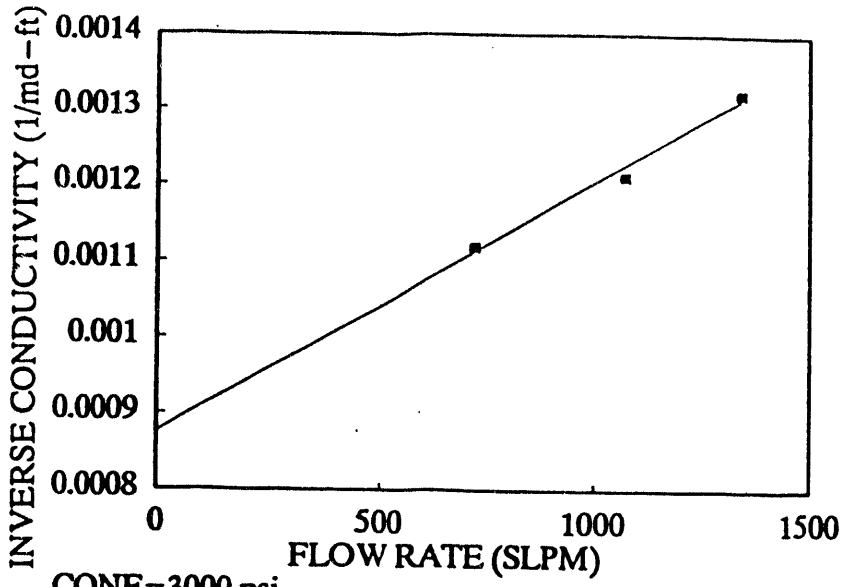

Figure 36 Turbulence data

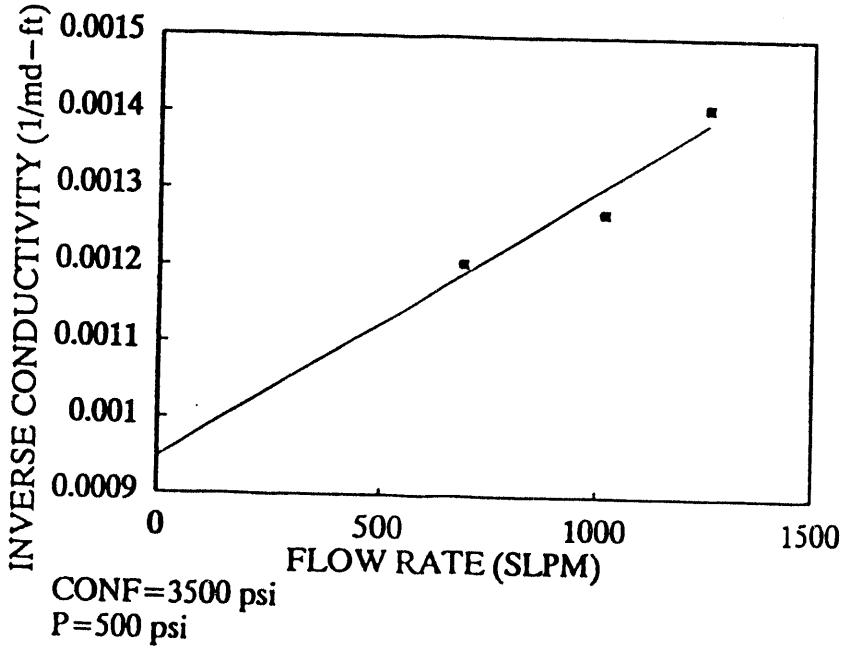

Figure 37 Turbulence data

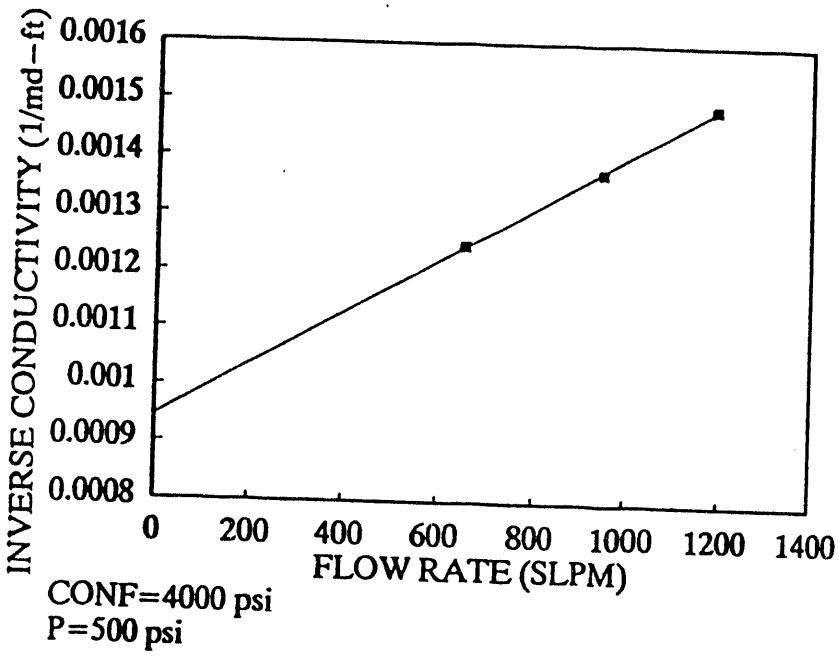

Figure 38 Turbulence data

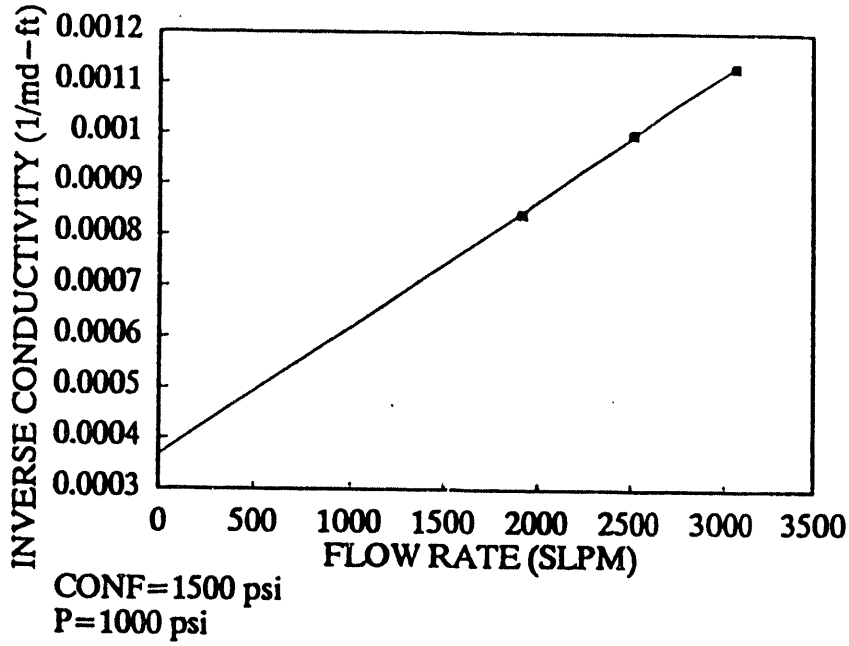

Figure 39 Turbulence data

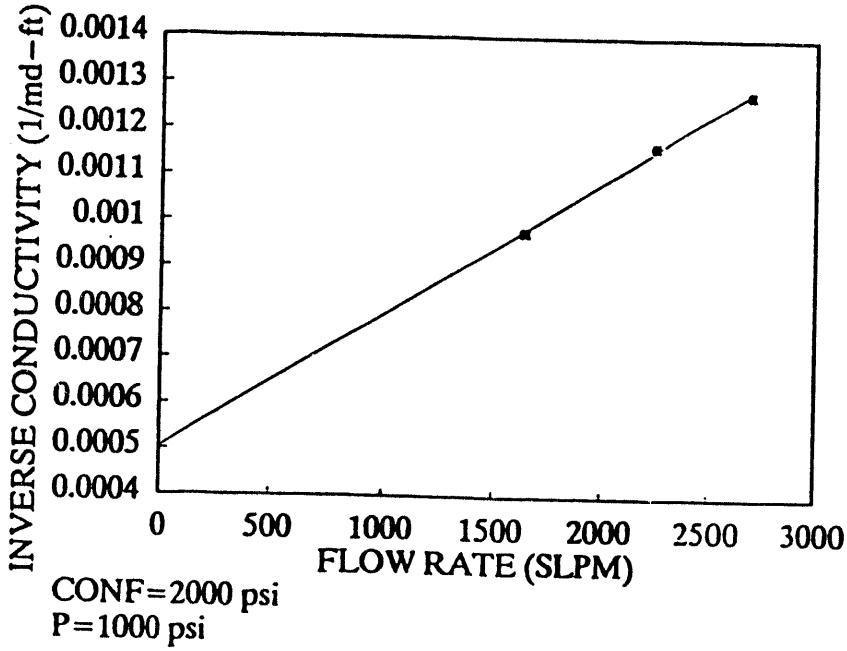

Figure 40 Turbulence data

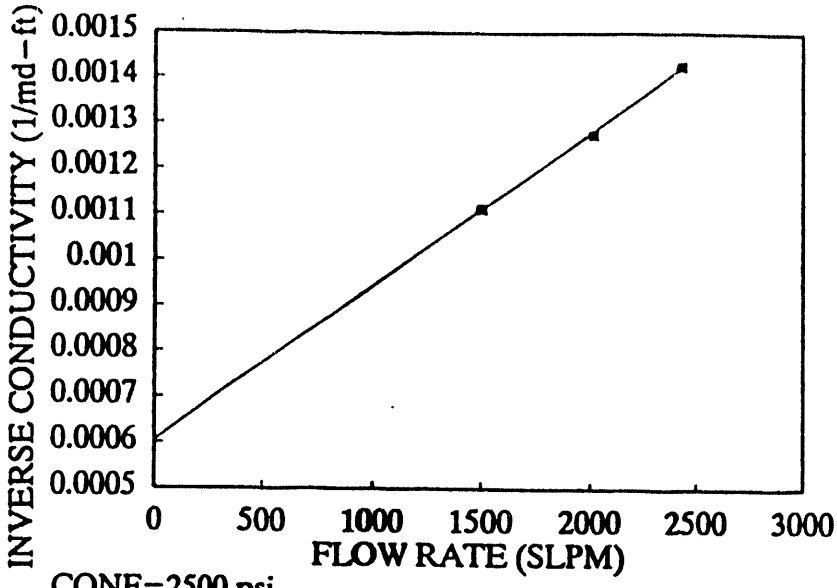

Figure 41 Turbulence data

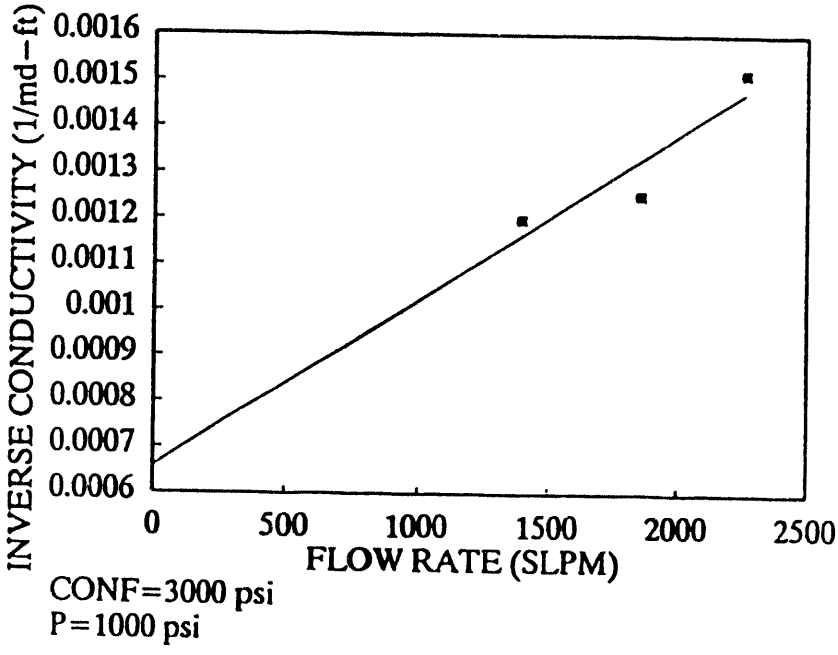

Figure 42 Turbulence data

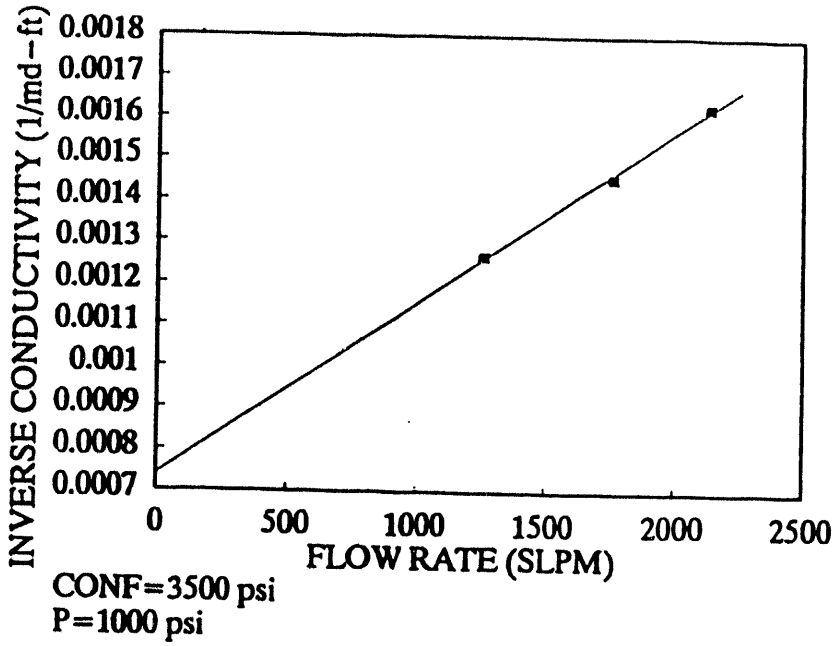

Figure 43 Turbulence data

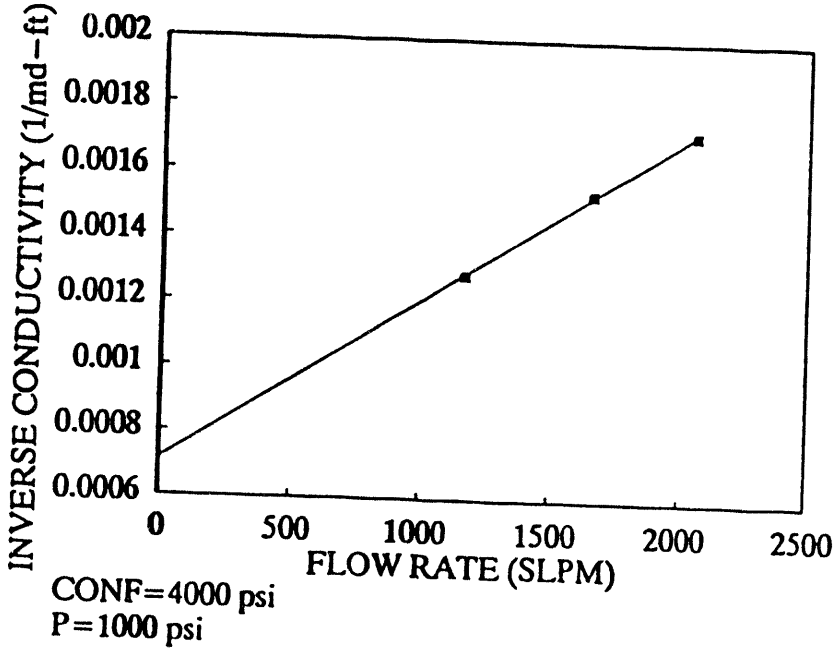

Figure 44 Turbulence data

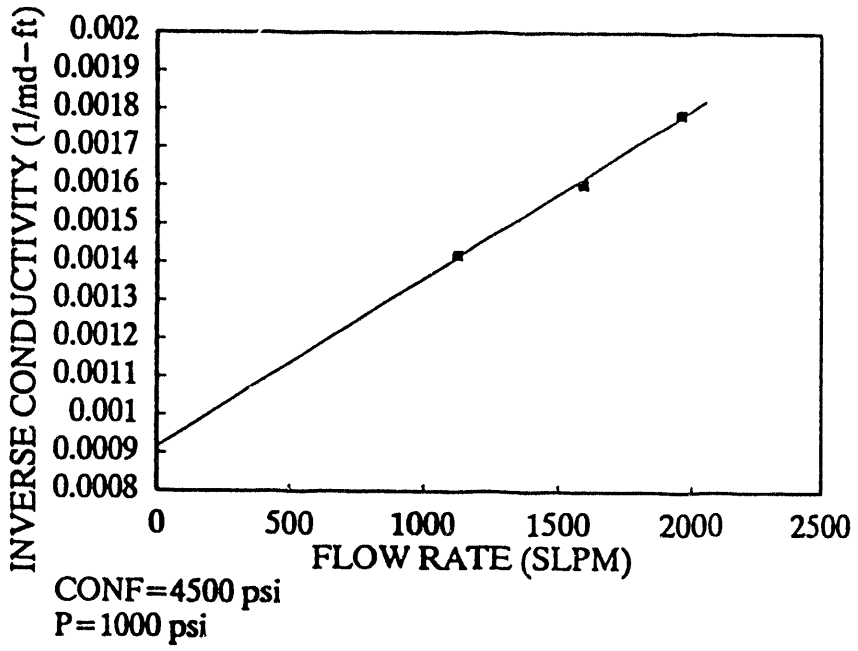

Figure 45 Turbulence data

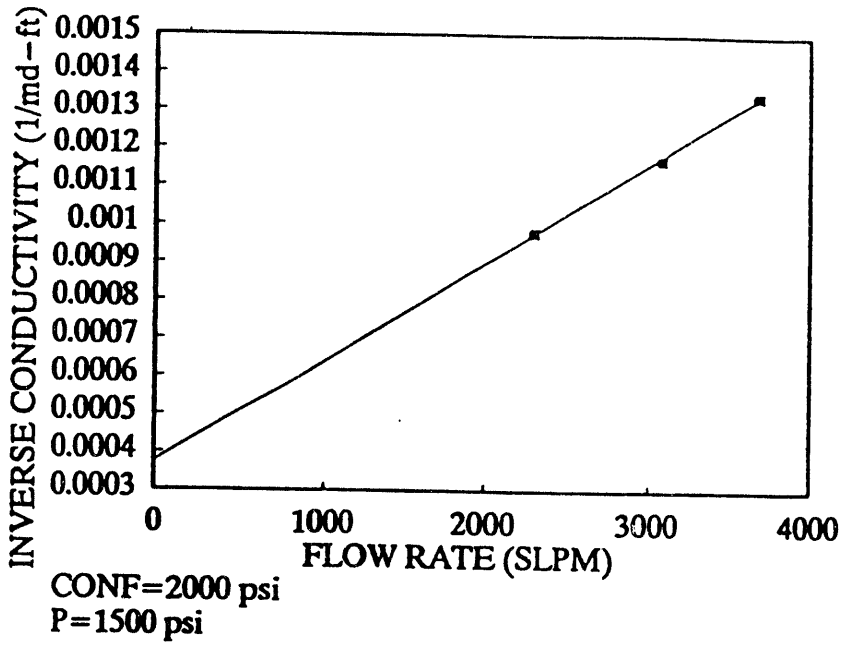

Figure 46 Turbulence data

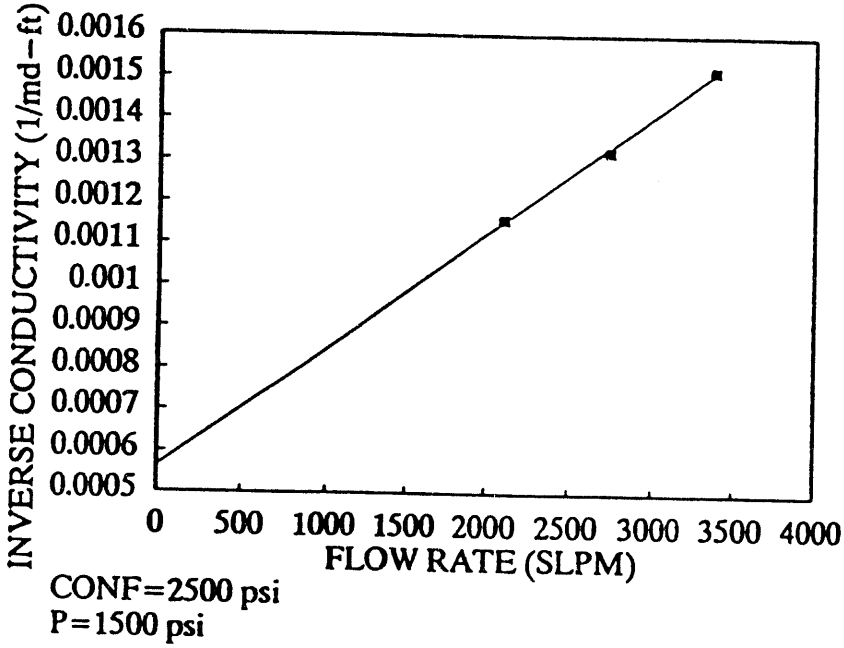

Figure 47 Turbulence data

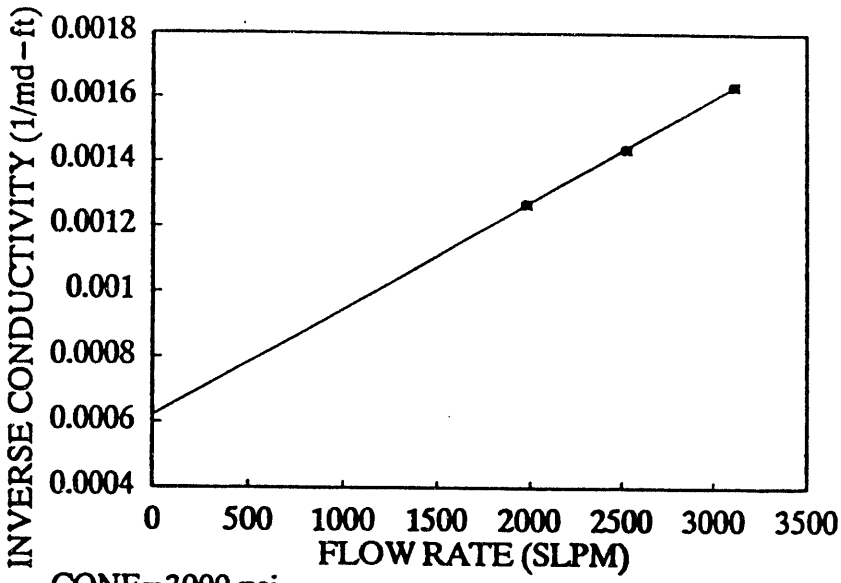

Figure 48 Turbulence data

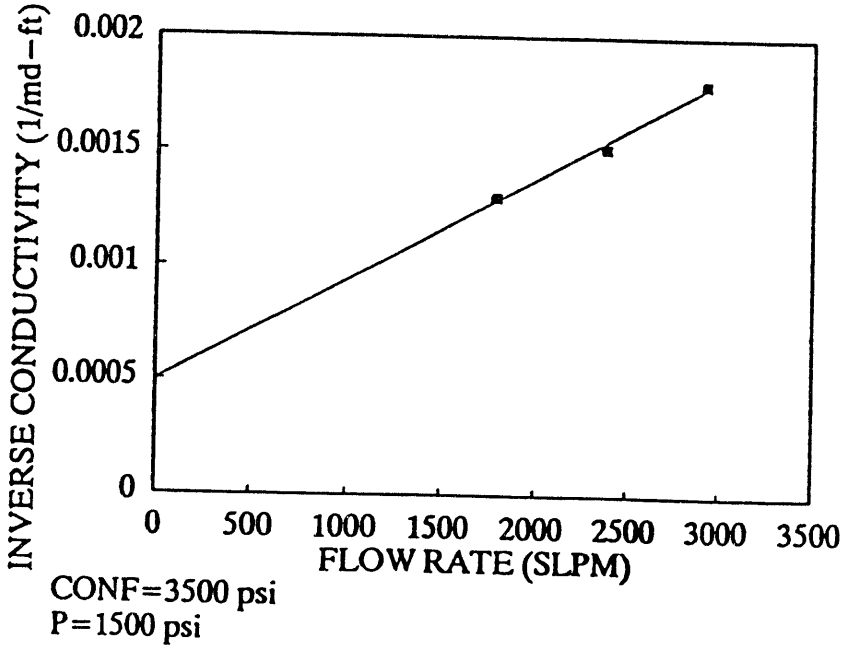

Figure 49 Turbulence data

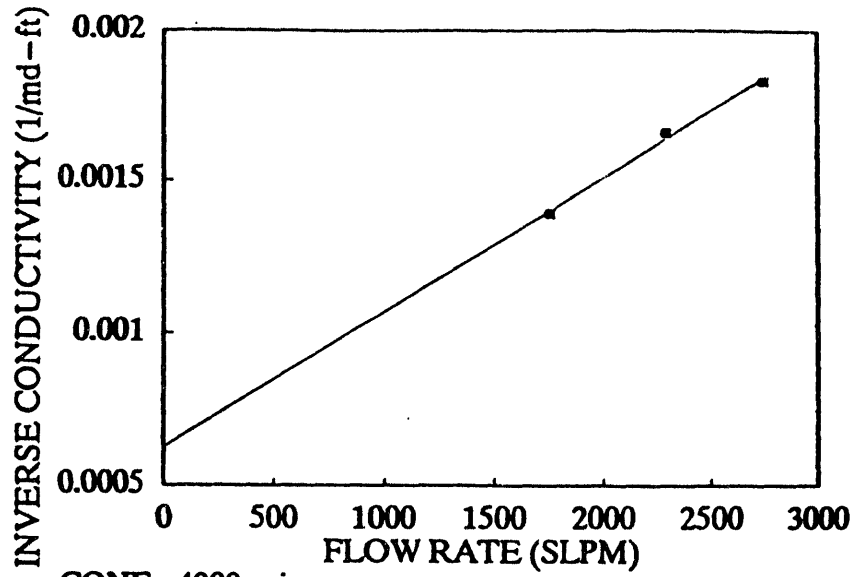

Figure 50 Turbulence data

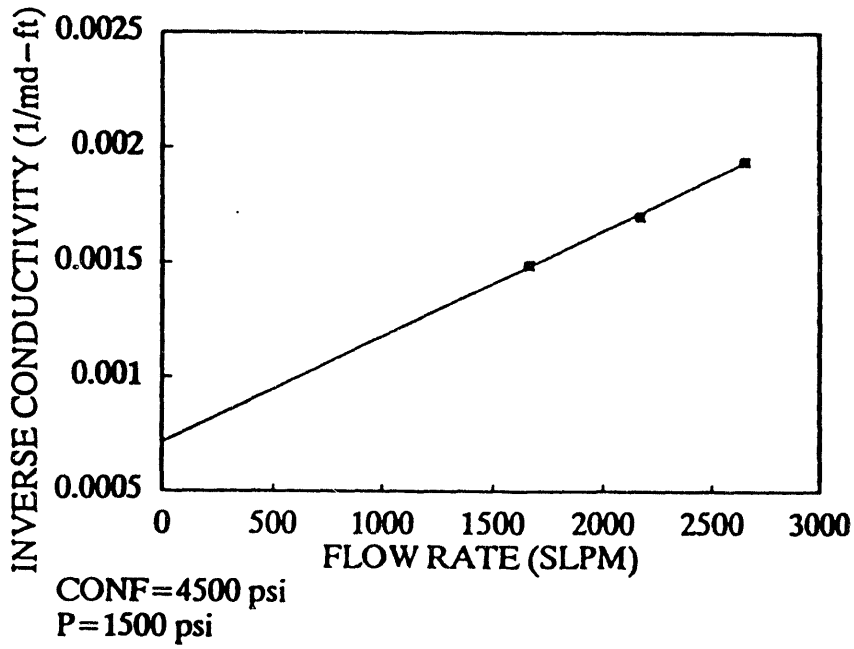

Figure 51 Turbulence data

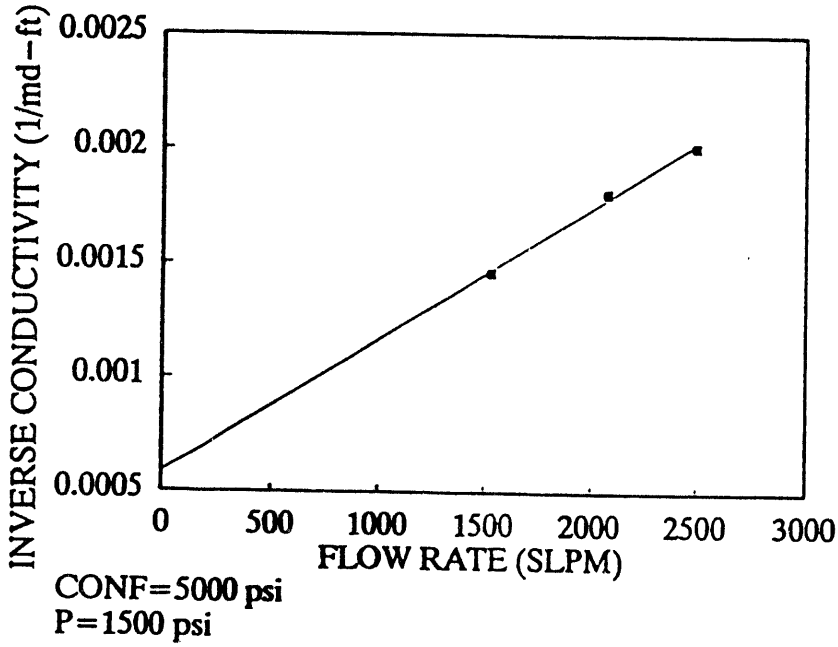

Figure 52 Turbulence data

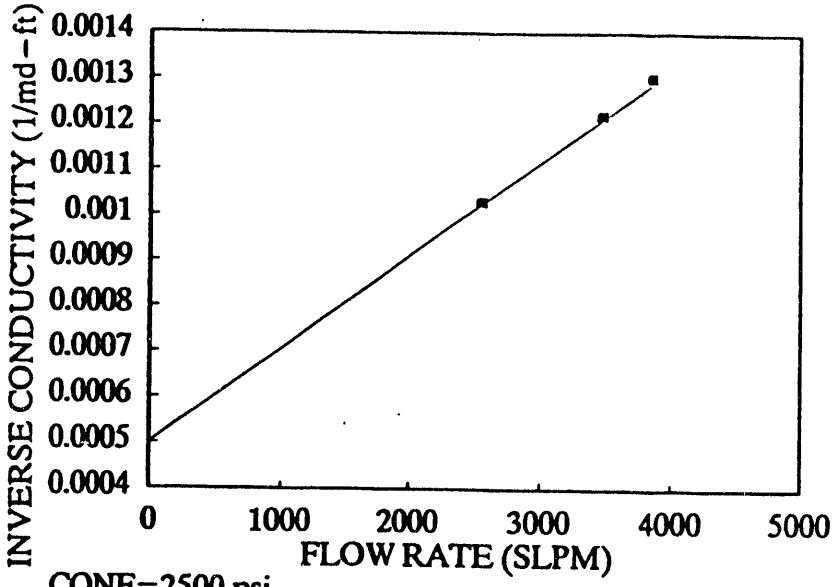

Figure 53 Turbulence data

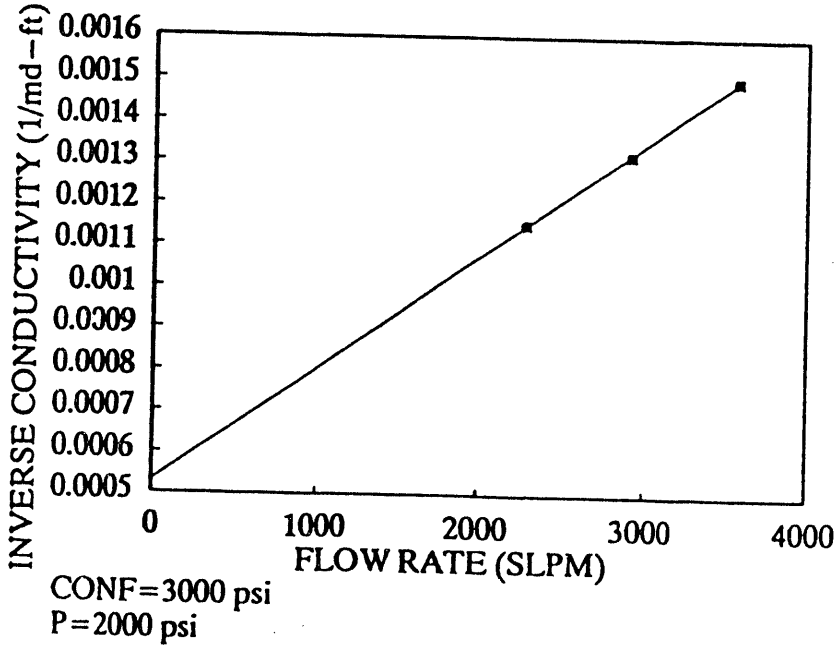

Figure 54 Turbulence data

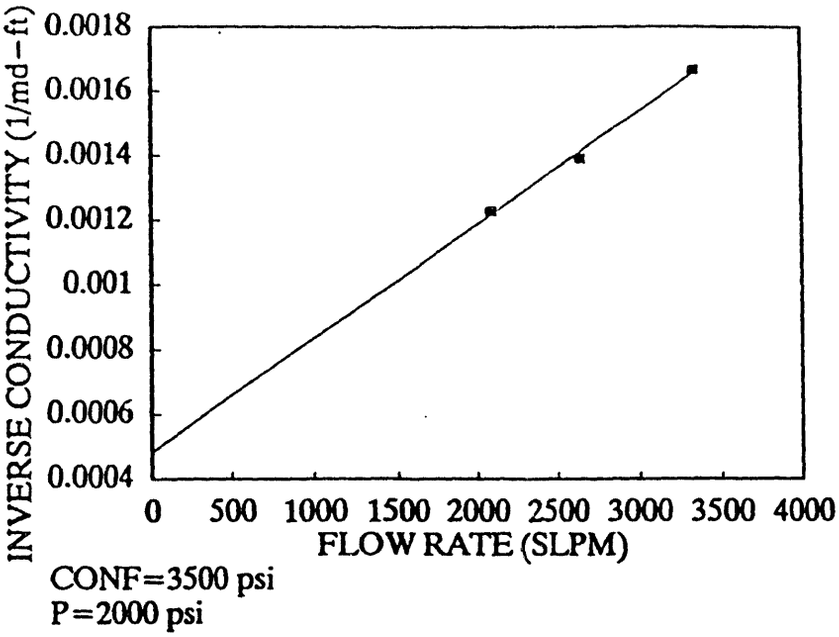

Figure 55 Turbulence data

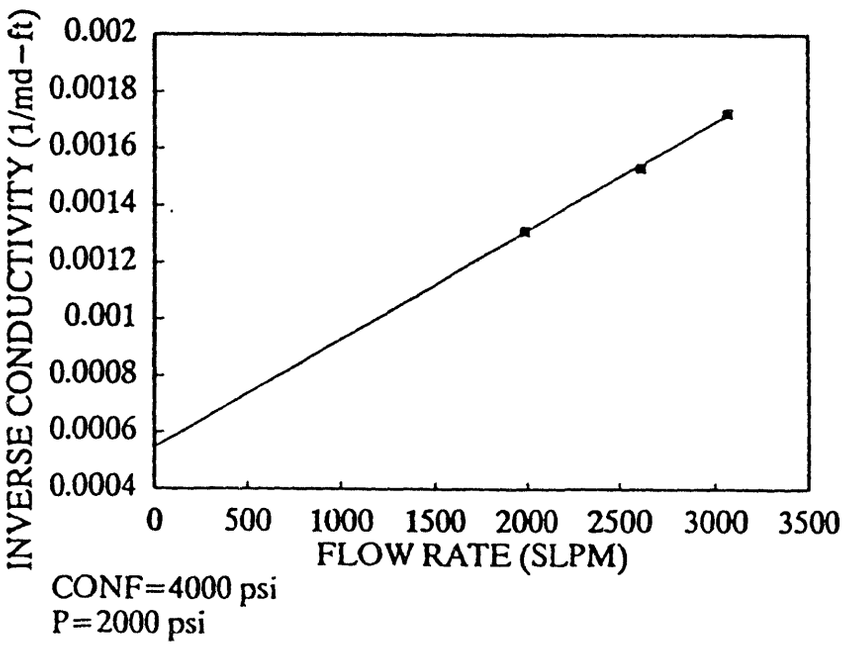

Figure 56 Turbulence data

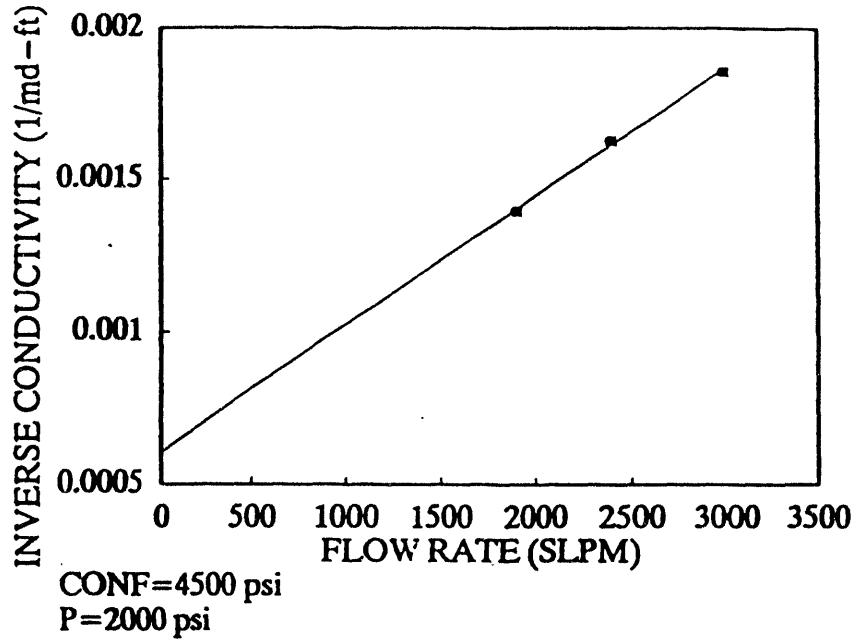

Figure 57 Turbulence data

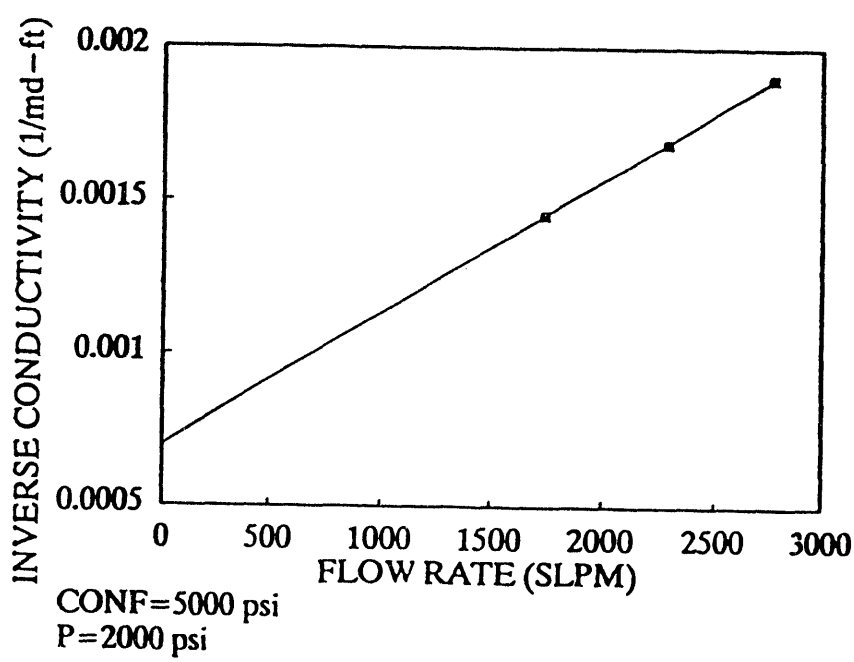

Figure 58 Turbulence data

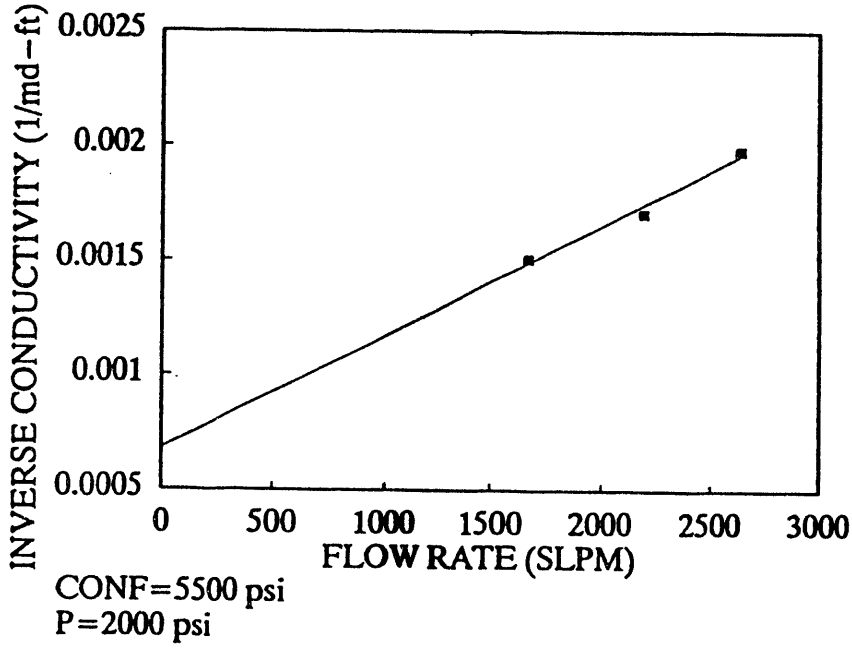

Figure 59 Turbulence data

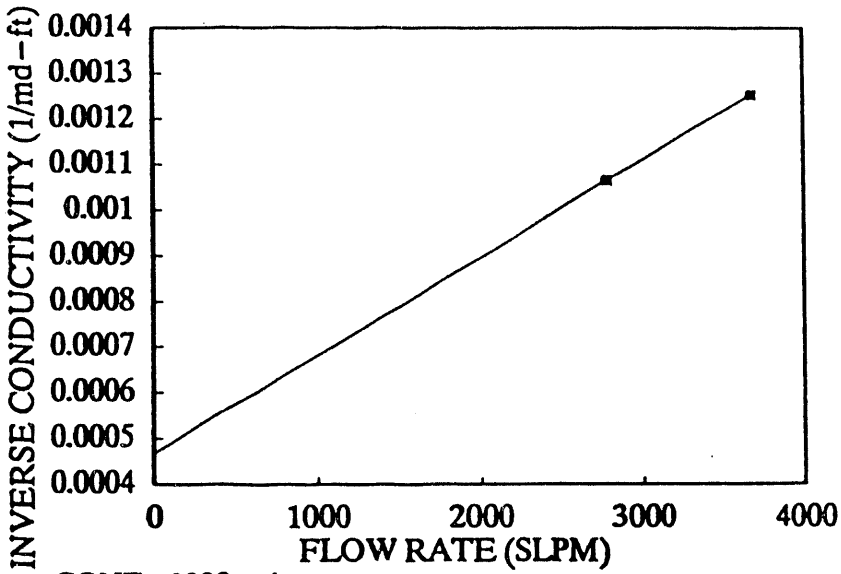

CONF=3000 psi
P=2500 psi

Figure 60 Turbulence data

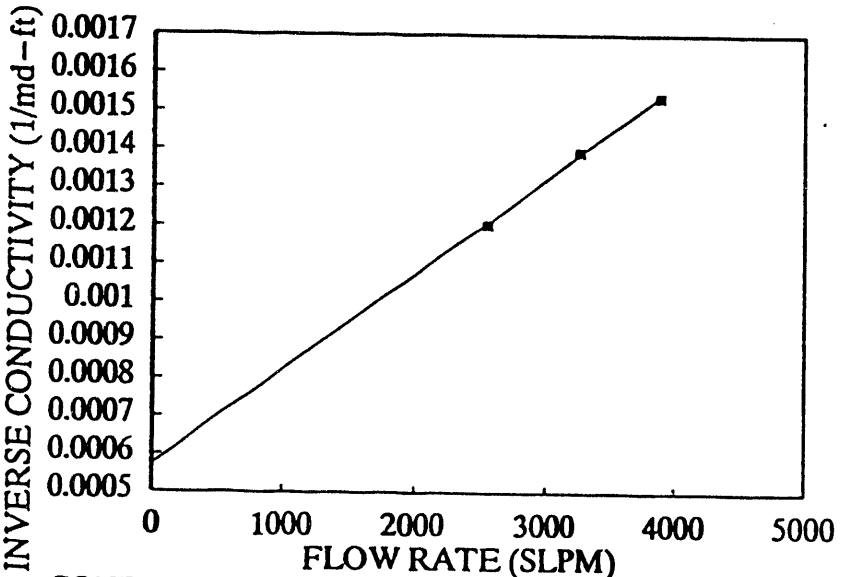

CONF=3500 psi
P=2500 psi

Figure 61 Turbulence data

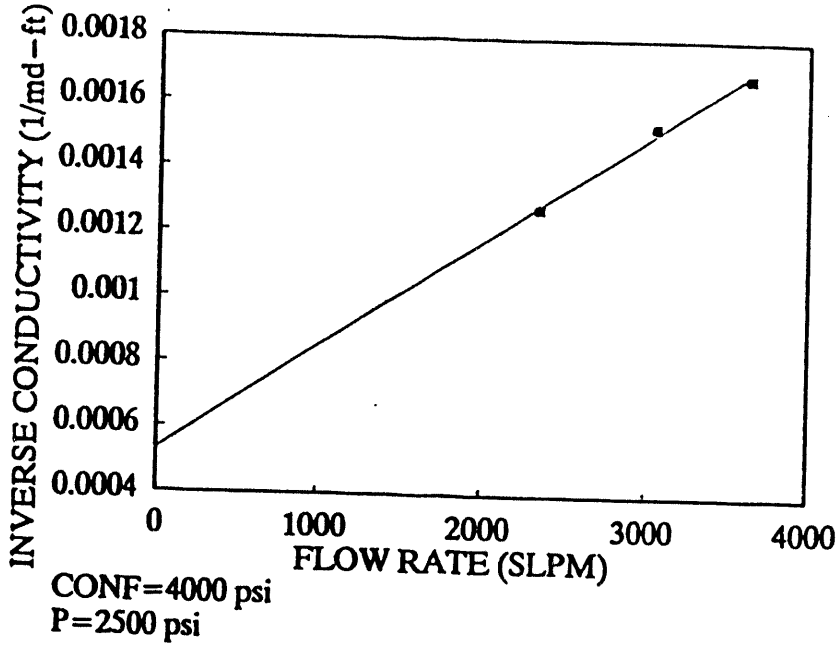

Figure 62 Turbulence data

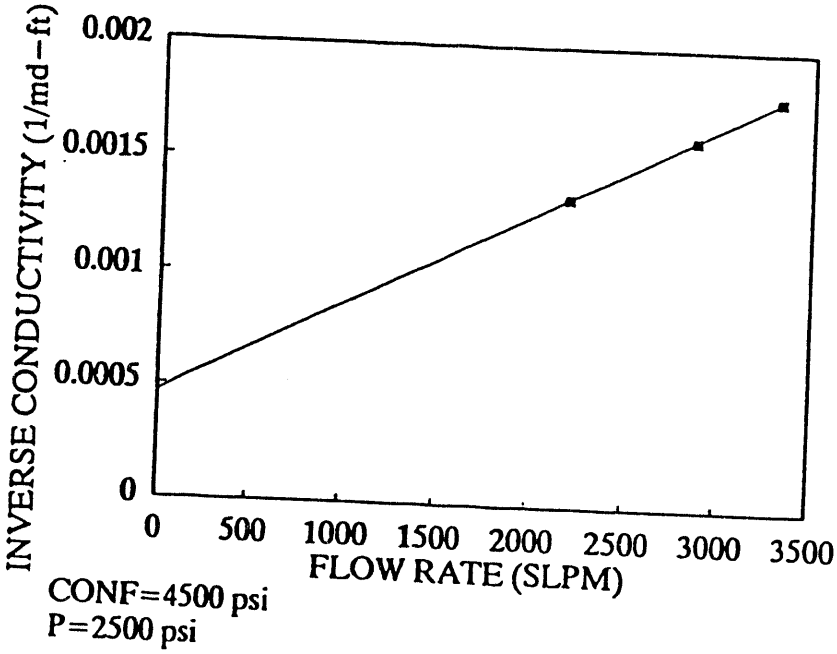

Figure 63 Turbulence data

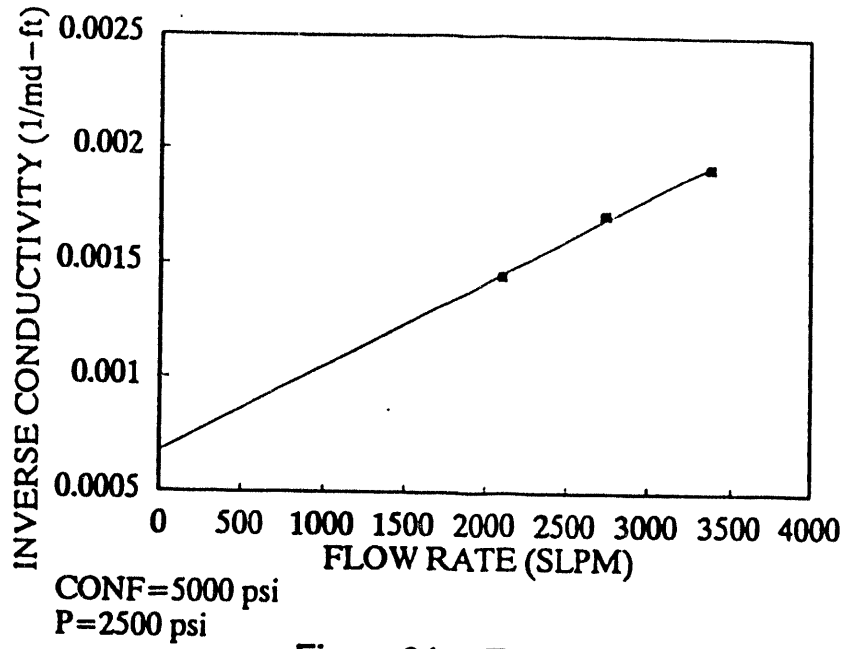

Figure 64 Turbulence data

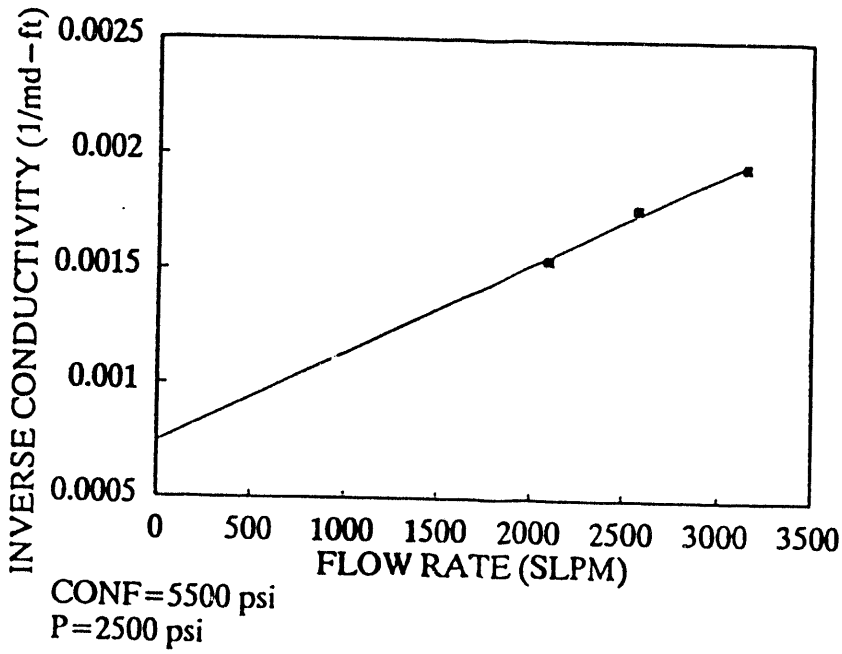

Figure 65 Turbulence data

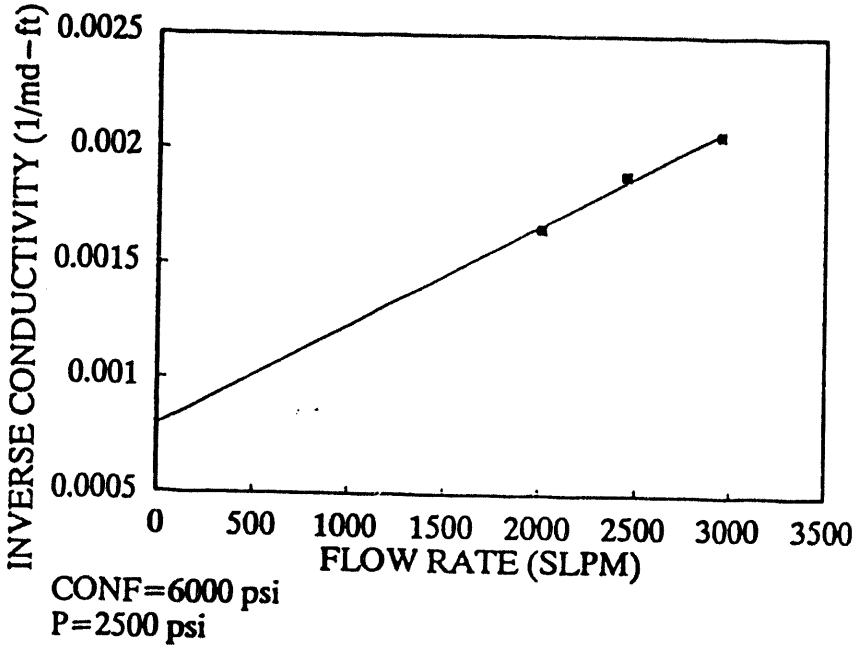

Figure 66 Turbulence data

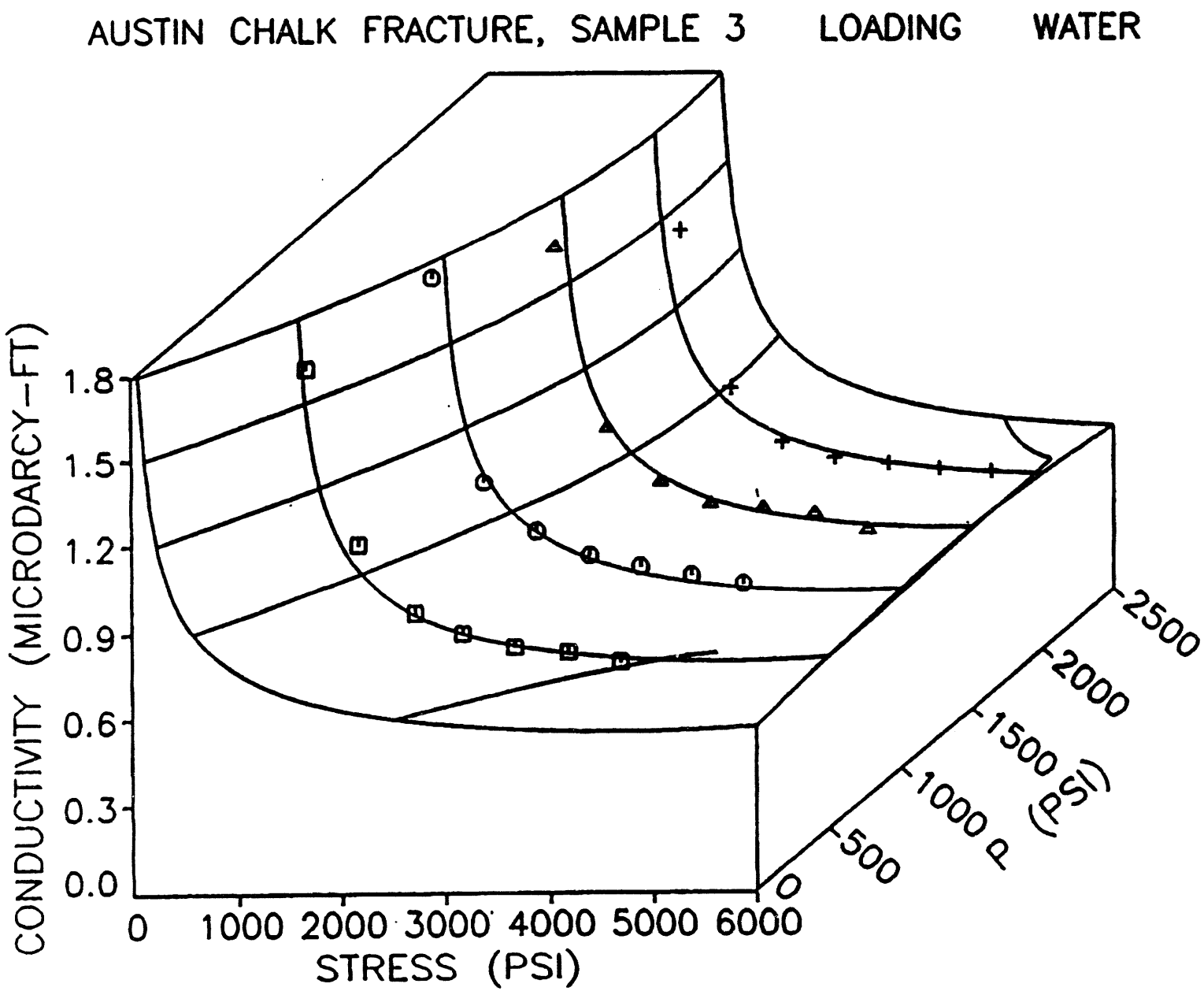

Figure 67 Response surface, sample B, water test fluid

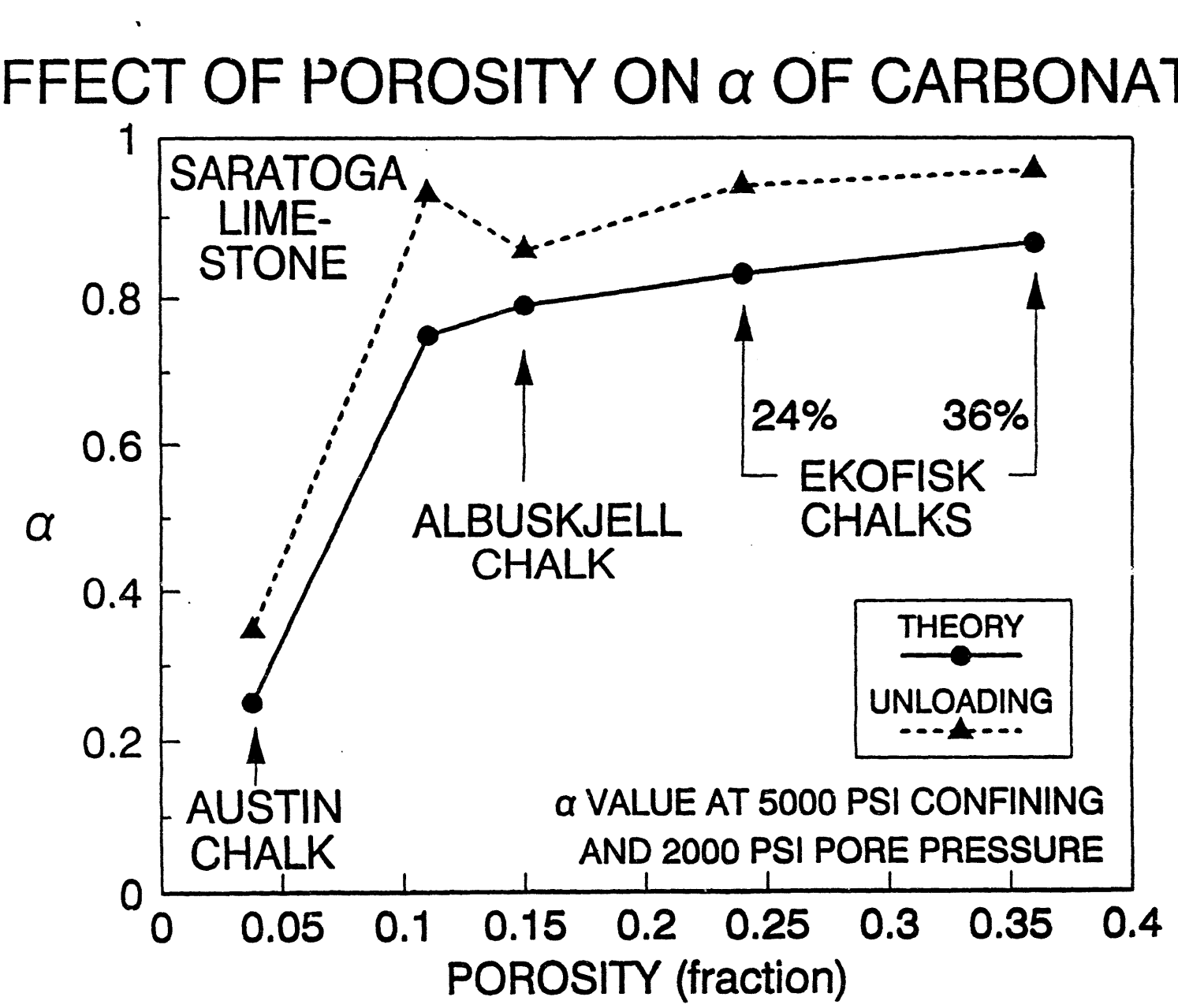

Figure 68 Variation of α with porosity

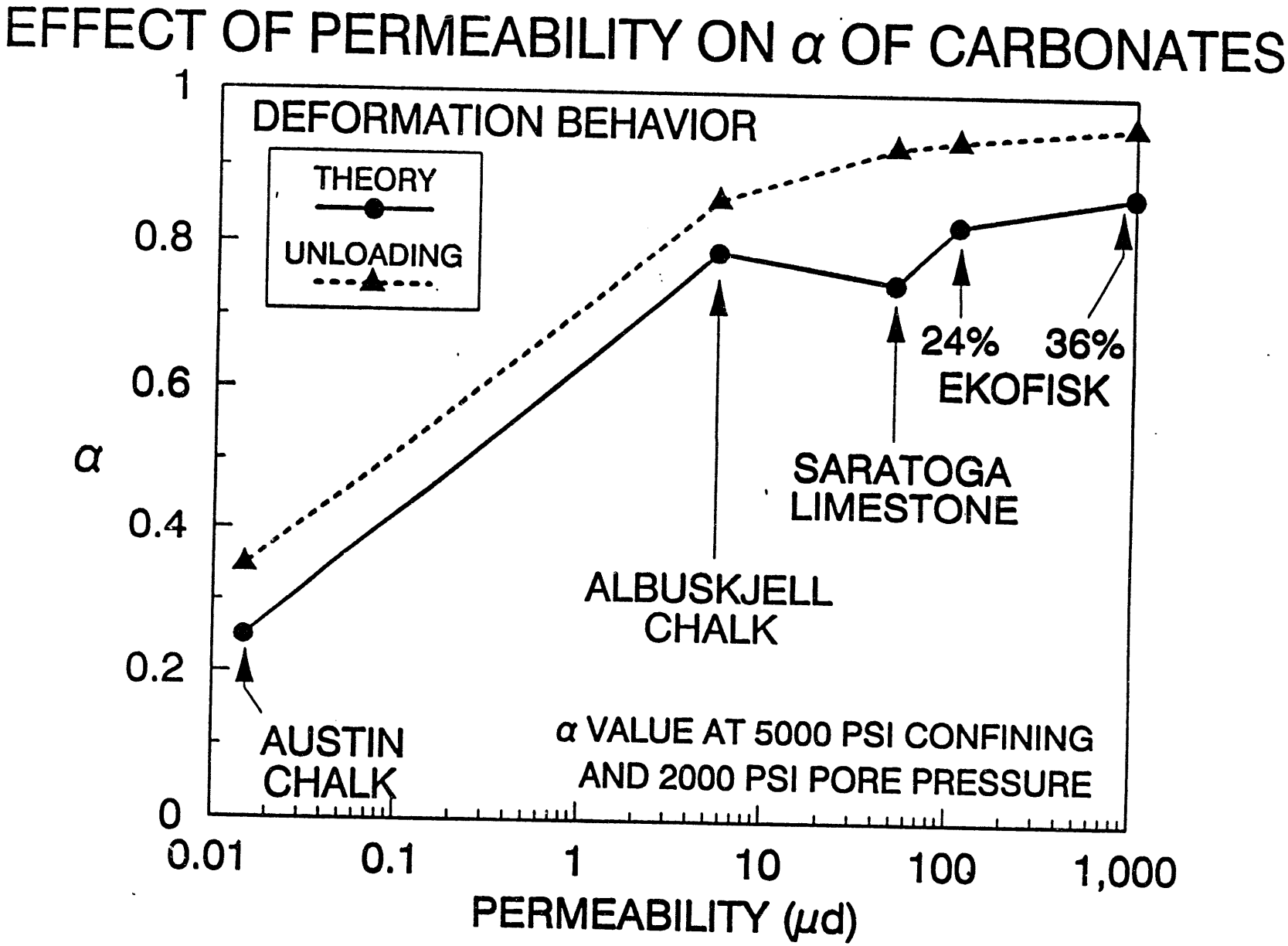

Figure 69 Variation of α with permeability

Table 1 Raw strain data for sample B, loading

STRESS	PRESSURE	EPS-AXIAL	EPS-CIRC.
500.000	0.000	0.007	0.069
1000.000	0.000	0.046	0.115
1500.000	0.000	0.092	0.167
2000.000	0.000	0.137	0.217
3000.000	0.000	0.224	0.317
4000.000	0.000	0.319	0.420
5000.000	0.000	0.414	0.524
6000.000	0.000	0.508	0.631
7000.000	0.000	0.613	0.743
8000.000	0.000	0.707	0.843

Table 2 Raw strain data for sample B, loading

STRESS	PRESSURE	EPS-AXIAL	EPS-CIRC.
1351.000	849.000	0.046	0.122
2005.000	847.000	0.108	0.191
2997.000	845.000	0.197	0.291
3996.000	848.000	0.288	0.391
5000.000	849.000	0.378	0.494
6003.000	849.000	0.471	0.597
6988.000	849.000	0.561	0.698
7928.000	849.000	0.652	0.797

Table 3 Raw strain data for sample B, loading

STRESS	PRESSURE	EPS-AXIAL	EPS-CIRC.
2506.000	2019.000	0.120	0.195
2954.000	2019.000	0.152	0.236
3968.000	2019.000	0.253	0.341
5017.000	2019.000	0.346	0.441
6014.000	2019.000	0.437	0.545
6997.000	2019.000	0.522	0.648
7945.000	2020.000	0.614	0.748

Table 4 Raw strain data for sample B, loading

STRESS	PRESSURE	EPS-AXIAL	EPS-CIRC.
3511.860	3083.210	0.166	0.253
4049.030	3084.090	0.212	0.306
5021.710	3083.920	0.291	0.409
5997.950	3083.710	0.380	0.500
7072.080	3084.790	0.479	0.616
7968.920	3084.990	0.561	0.711

Table 5 Raw strain data for sample B, loading

STRESS	PRESSURE	EPS-AXIAL	EPS-CIRC.
4515.860	4021.040	0.223	0.319
4999.720	4022.510	0.262	0.363
6029.290	4022.510	0.347	0.473
6987.000	4022.130	0.435	0.565

Table 6 Volumetric strain data for sample B, loading

STRESS	PRESSURE	VOL STRN
500	0	0.00555
1000	0	0.0121
1500	0	0.0196
2000	0	0.02685
3000	0	0.0412
4000	0	0.05625
5000	0	0.0714
6000	0	0.0868
7000	0	0.10325
8000	0	0.11795
1351	849	0.0128
2005	847	0.0228
2997	845	0.03725
3996	848	0.0518
5000	849	0.0666
6003	849	0.08155
6988	849	0.09615
7928	849	0.1106
2506	2019	0.0238
2954	2019	0.0295
3968	2019	0.04505
5017	2019	0.0597
6014	2019	0.07465
6997	2019	0.0892
7945	2020	0.1038
3512	3083	0.03189
4049	3084	0.03952
5022	3084	0.05369
5998	3084	0.06731
7072	3085	0.08384
7969	3085	0.097435
4516	4021	0.041355
5000	4023	0.04768
6029	4023	0.062885
6987	4022	0.076585
7988	4022	0.091765

Table 7 Raw strain data for sample B, unloading

STRESS	PRESSURE	EPS-AXIAL	EPS-CIRC.
500.000	0.000	0.009	0.072
1000.000	0.000	0.056	0.123
1500.000	0.000	0.102	0.175
2000.000	0.000	0.151	0.228
3000.000	0.000	0.256	0.342
4000.000	0.000	0.348	0.444
5000.000	0.000	0.439	0.540
6000.000	0.000	0.539	0.648
7000.000	0.000	0.631	0.750
8000.000	0.000	0.707	0.843

Table 8 Raw strain data for sample B, unloading

STRESS	PRESSURE	EPS-AXIAL	EPS-CIRC.
1353.000	849.000	0.050	0.122
2003.000	849.000	0.108	0.189
3010.000	849.000	0.200	0.292
4013.000	849.000	0.294	0.396
5010.000	847.000	0.386	0.496
6010.000	849.000	0.483	0.597
7025.000	849.000	0.575	0.702
7928.000	849.000	0.652	0.797

Table 9 Raw strain data for sample B, unloading

STRESS	PRESSURE	EPS-AXIAL	EPS-CIRC.
2505.000	2019.000	0.125	0.198
3023.000	2018.000	0.169	0.250
3998.000	2018.000	0.263	0.349
4951.000	2019.000	0.337	0.442
6004.000	2018.000	0.443	0.547
7007.000	2019.000	0.537	0.647
7944.000	2020.000	0.614	0.748

Table 10 Raw strain data for sample B, unloading

STRESS	PRESSURE	EPS-AXIAL	EPS-CIRC.
3480.800	3085.780	0.158	0.250
3999.610	3084.090	0.213	0.301
4978.040	3083.870	0.296	0.401
6007.410	3084.290	0.394	0.504
6967.280	3084.880	0.477	0.600
7968.920	3084.990	0.561	0.711

Table 11 Raw strain data for sample B, unloading

STRESS	PRESSURE	EPS-AXIAL	EPS-CIRC.
4502.030	4022.250	0.221	0.315
5019.870	4022.130	0.270	0.370
5996.270	4021.650	0.358	0.464
6985.690	4022.850	0.448	0.566
7988.100	4022.170	0.526	0.672

Table 12 Volumetric strain data for sample B, unloading

STRESS	PRESSURE	VOL STRN
500	0	0.00595
1000	0	0.0134
1500	0	0.0209
2000	0	0.02865
3000	0	0.0453
4000	0	0.0601
5000	0	0.07425
6000	0	0.09005
7000	0	0.10485
8000	0	0.11795
1353	849	0.013
2003	849	0.0226
3010	849	0.0375
4013	849	0.0526
5010	847	0.0672
6010	849	0.08215
7025	849	0.09725
7928	849	0.1106
2505	2019	0.02435
3023	2018	0.03175
3998	2018	0.04635
4951	2019	0.05935
6004	2018	0.07515
7007	2019	0.08985
7944	2020	0.1038
3481	3086	0.03118
4000	3084	0.03903
4978	3084	0.053165
6007	3084	0.06841
6967	3085	0.082195
7969	3085	0.097435
4502	4022	0.04089
5020	4022	0.04878
5996	4022	0.062595
6986	4023	0.077295
7988	4022	0.091765

Table 13 Raw strain data for sample B, loading, pressure unloading

STRESS	PRESSURE	EPS-AXIAL	EPS-CIRC.
540.000	0.000	0.007	0.062
891.090	0.000	0.053	0.113
1963.960	0.000	0.132	0.209
2946.160	0.000	0.223	0.299
3989.550	0.000	0.320	0.411
5016.330	0.000	0.407	0.513
6013.440	0.000	0.502	0.614
6950.840	0.000	0.581	0.716
7970.100	0.000	0.683	0.814

Table 14 Raw strain data for sample B, loading, pressure unloading

STRESS	PRESSURE	EPS-AXIAL	EPS-CIRC.
1504.510	1041.270	0.072	0.116
1981.490	1040.540	0.100	0.169
2974.480	1040.240	0.187	0.272
3973.340	1040.420	0.288	0.371
4985.240	1040.550	0.379	0.470
6017.920	1040.130	0.458	0.578
7025.050	1040.980	0.559	0.683
7991.740	1040.900	0.645	0.785

Table 15 Raw strain data for sample B, loading, pressure unloading

STRESS	PRESSURE	EPS-AXIAL	EPS-CIRC.
2517.600	1998.730	0.121	0.181
2967.470	1999.160	0.155	0.228
3994.090	1998.700	0.234	0.332
4981.050	1999.190	0.328	0.436
5991.780	1999.490	0.417	0.543
7012.730	1999.870	0.513	0.647
7962.920	1999.960	0.606	0.736

Table 16 Raw strain data for sample B, loading, pressure unloading

STRESS	PRESSURE	EPS-AXIAL	EPS-CIRC.
3561.880	3069.900	0.166	0.248
4011.780	3070.090	0.199	0.300
4997.990	3069.930	0.288	0.390
6013.780	3069.540	0.384	0.498
7164.500	3070.010	0.482	0.618
8047.030	3069.930	0.570	0.711

Table 17 Raw strain data for sample B, loading, pressure unloading

STRESS	PRESSURE	EPS-AXIAL	EPS-CIRC.
4515.860	4021.040	0.223	0.319
4999.720	4022.510	0.262	0.363
6029.290	4022.510	0.347	0.473
6987.000	4022.130	0.435	0.565
7988.100	4022.170	0.526	0.672

Table 18 Volumetric strain data for sample B, loading pressure unloading

STRESS	PRESSURE	VOL STRN
540	0	0.00484
891	0	0.01225
1964	0	0.0258
2946	0	0.039355
3990	0	0.055395
5016	0	0.069925
6013	0	0.08476
6951	0	0.098925
7970	0	0.113885
1505	1041	0.013475
1981	1041	0.02021
2974	1040	0.034835
3973	1040	0.04973
4985	1041	0.064235
6018	1040	0.07898
7025	1041	0.094505
7992	1041	0.109075
2518	1999	0.022505
2967	1999	0.02883
3994	1999	0.04326
4981	1999	0.05835
5992	1999	0.07348
7013	2000	0.088665
7963	2000	0.102245
3562	3070	0.031395
4012	3070	0.03821
4998	3070	0.05173
6014	3070	0.06733
7165	3070	0.08415
8047	3070	0.097875
4516	4021	0.041355
5000	4023	0.04768
6029	4023	0.062885
6987	4022	0.076585
7988	4022	0.091765

Table 19 Raw strain data for sample B, unloading, pressure unloading

STRESS	PRESSURE	EPS-AXIAL	EPS-CIRC.
495.210	0.000	0.007	0.060
993.640	0.000	0.052	0.108
2024.180	0.000	0.142	0.212
3004.990	0.000	0.233	0.318
4003.050	0.000	0.333	0.421
4990.200	0.000	0.422	0.510
5998.700	0.000	0.512	0.619
6989.400	0.000	0.605	0.722
7970.100	0.000	0.683	0.814

Table 20 Raw strain data for sample B, unloading, pressure unloading

STRESS	PRESSURE	EPS-AXIAL	EPS-CIRC.
1507.410	1040.000	0.058	0.117
2033.330	1040.150	0.099	0.181
3009.710	1040.500	0.189	0.268
4004.070	1040.680	0.288	0.373
5005.440	1040.490	0.385	0.478
6012.090	1041.010	0.483	0.581
6957.490	1040.820	0.562	0.672
7991.740	1040.900	0.645	0.785

Table 21 Raw strain data for sample B, unloading, pressure unloading

STRESS	PRESSURE	EPS-AXIAL	EPS-CIRC.
2505.490	1997.860	0.110	0.189
3002.940	1998.190	0.159	0.238
4025.200	1998.600	0.251	0.336
5002.420	1999.350	0.340	0.435
6003.000	1999.000	0.431	0.534
6977.490	2000.200	0.519	0.635
7962.920	1999.960	0.606	0.736

Table 22 Raw strain data for sample B, unloading, pressure unloading

STRESS	PRESSURE	EPS-AXIAL	EPS-CIRC.
3511.600	3069.140	0.157	0.247
4017.370	3069.780	0.213	0.293
5009.500	3070.320	0.297	0.395
5929.650	3070.940	0.385	0.489
6987.340	3069.630	0.480	0.597
8047.030	3069.930	0.570	0.711

Table 23 Raw strain data for sample B, unloading, pressure unloading

STRESS	PRESSURE	EPS-AXIAL	EPS-CIRC.
4502.030	4022.250	0.221	0.315
5019.870	4022.130	0.270	0.370
5996.270	4021.650	0.358	0.464
6985.690	4022.850	0.448	0.566
7988.100	4022.170	0.526	0.672

Table 24 Volumetric strain data for sample B, unloading, pressure unloading

STRESS	PRESSURE	VOL STRN
495	0	0.00466
994	0	0.01172
2024	0	0.02661
3005	0	0.041695
4003	0	0.05705
4990	0	0.07038
5999	0	0.08581
6989	0	0.100775
7970	0	0.113885
1507	1040	0.012935
2033	1040	0.02136
3010	1041	0.03454
4004	1041	0.05002
5005	1040	0.065355
6012	1041	0.080535
6957	1041	0.0936
7992	1041	0.109075
2505	1998	0.0227
3003	1998	0.03003
4025	1999	0.044455
5002	1999	0.05884
6003	1999	0.07325
6977	2000	0.08774
7963	2000	0.102245
3512	3069	0.030905
4017	3070	0.038225
5010	3070	0.052685
5930	3071	0.06645
6987	3070	0.082025
8047	3070	0.097875
4502	4022	0.04089
5020	4022	0.04878
5996	4022	0.062595
6986	4023	0.077295
7988	4022	0.091765

Table 25 Raw strain data for sample C, loading

STRESS	PRESSURE	EPS-AXIAL	EPS-CIRC.
507.000	0.000	0.033	0.019
1003.000	0.000	0.077	0.063
1995.000	0.000	0.168	0.157
2975.000	0.000	0.255	0.255
3970.000	0.000	0.342	0.357
5016.000	0.000	0.440	0.468
5988.000	0.000	0.518	0.567
6944.000	0.000	0.598	0.662
7949.000	0.000	0.682	0.765

Table 26 Raw strain data for sample C, loading

STRESS	PRESSURE	EPS-AXIAL	EPS-CIRC.
1530.000	1031.000	0.092	0.108
2006.000	1030.000	0.132	0.154
3002.000	1030.000	0.219	0.253
3949.000	1030.000	0.300	0.346
5007.000	1030.000	0.388	0.449
6023.000	1030.000	0.478	0.553
6988.000	1030.000	0.552	0.647
7886.000	1030.000	0.627	0.738

Table 27 Raw strain data for sample C, loading

STRESS	PRESSURE	EPS-AXIAL	EPS-CIRC.
2498.000	2006.000	0.148	0.171
2986.000	2006.000	0.188	0.217
3961.000	2006.000	0.270	0.314
5060.000	2006.000	0.362	0.422
5986.000	2006.000	0.438	0.512
6974.000	2006.000	0.521	0.612
8010.000	2006.000	0.606	0.715

Table 28 Raw strain data for sample C, loading

STRESS	PRESSURE	EPS-AXIAL	EPS-CIRC.
3528.000	3007.000	0.207	0.240
3983.000	3006.000	0.240	0.288
4967.000	3006.000	0.321	0.385
5962.000	3006.000	0.404	0.483
6934.000	3006.000	0.484	0.578
7923.000	3006.000	0.567	0.677

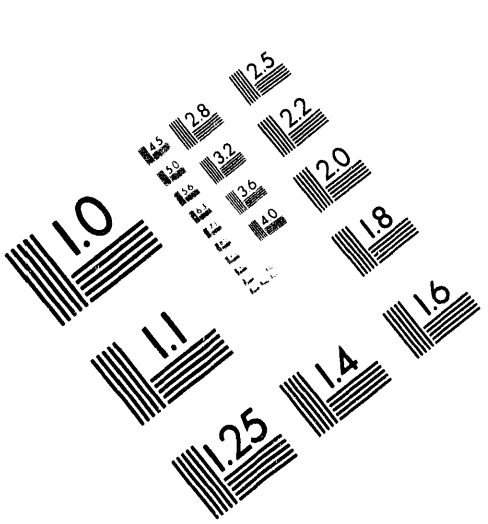

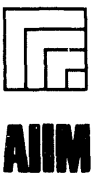

Association for Information and Image Management
1100 Wayne Avenue, Suite 1100
Silver Spring, Maryland 20910
301/587-8202

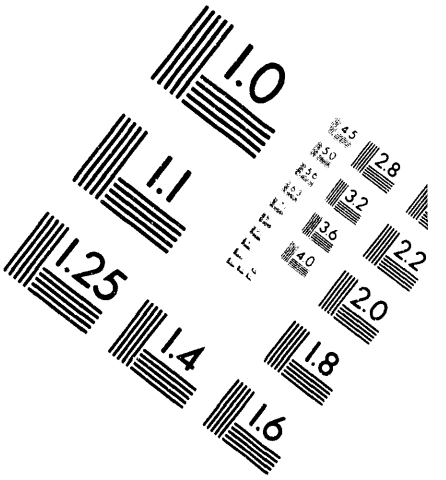

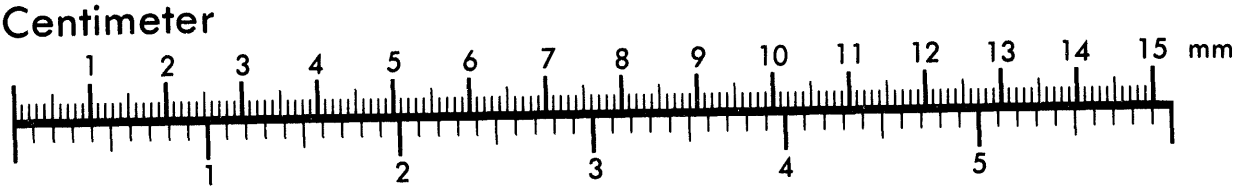

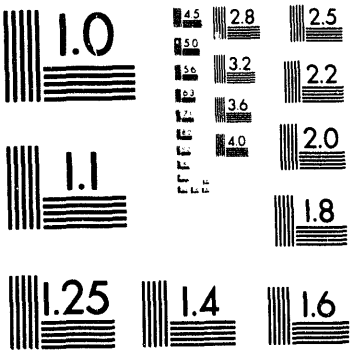

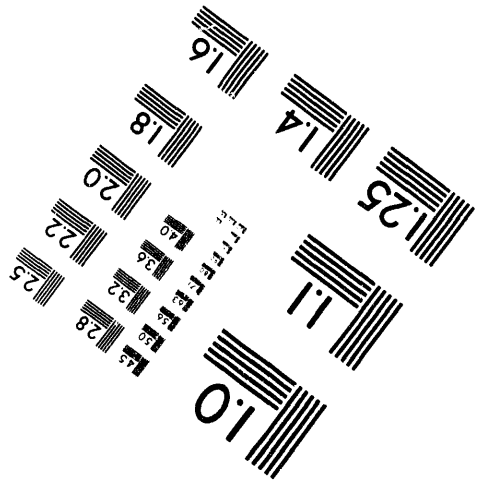

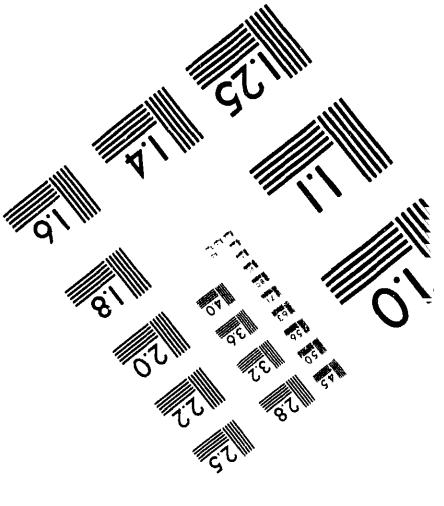

MANUFACTURED TO AIIM STANDARDS
BY APPLIED IMAGE, INC.

2 of 2

Table 29 Raw strain data for sample C, loading

STRESS	PRESSURE	EPS-AXIAL	EPS-CIRC.
451[illegible]000	4082.000	0.257	0.296
5033.000	4082.000	0.290	0.351
5950.000	4082.000	0.364	0.442
7047.000	4081.000	0.455	0.549
7929.000	4081.000	0.528	0.637

Table 30 Volumetric strain data for sample C, loading

STRESS	PRESSURE	VOL STRN
507	0	0.00355
1003	0	0.01015
1995	0	0.0241
2975	0	0.03825
3970	0	0.0528
5016	0	0.0688
5988	0	0.0826
6944	0	0.0961
7949	0	0.1106
1530	1031	0.0154
2006	1030	0.022
3002	1030	0.03625
3949	1030	0.0496
5007	1030	0.0643
6023	1030	0.0792
6988	1030	0.0923
7886	1030	0.10515
2498	2006	0.0245
2986	2006	0.0311
3961	2006	0.0449
5060	2006	0.0603
5986	2006	0.0731
6974	2006	0.08725
8010	2006	0.1018
3528	3007	0.03435
3983	3006	0.0408
4967	3006	0.05455
5962	3006	0.0685
6934	3006	0.082
7923	3006	0.09605
4516	4082	0.04245
5033	4082	0.0496
5950	4082	0.0624
7047	4081	0.07765
7929	4081	0.0901

Table 31 Raw strain data for sample C, unloading

STRESS	PRESSURE	EPS-AXIAL	EPS-CIRC.
510.000	0.000	0.035	0.031
1019.000	0.000	0.081	0.076
2043.000	0.000	0.171	0.176
3030.000	0.000	0.262	0.276
3986.000	0.000	0.347	0.375
4990.000	0.000	0.440	0.476
6034.000	0.000	0.532	0.578
6974.000	0.000	0.611	0.669
7949.000	0.000	0.682	0.765

Table 32 Raw strain data for sample C, unloading

STRESS	PRESSURE	EPS-AXIAL	EPS-CIRC.
1525.000	1030.000	0.089	0.113
2051.000	1030.000	0.133	0.163
3046.000	1030.000	0.218	0.263
3992.000	1030.000	0.300	0.355
5022.000	1030.000	0.390	0.454
6027.000	1030.000	0.480	0.551
6996.000	1030.000	0.560	0.647
7886.000	1030.000	0.627	0.738

Table 33 Raw strain data for sample C, unloading

STRESS	PRESSURE	EPS-AXIAL	EPS-CIRC.
2511.000	2006.000	0.144	0.170
3034.000	2006.000	0.188	0.221
4025.000	2006.000	0.274	0.321
5018.000	2006.000	0.362	0.417
6002.000	2006.000	0.449	0.513
6980.000	2006.000	0.532	0.612
8010.000	2006.000	0.606	0.715

Table 34 Raw strain data for sample C, unloading

STRESS	PRESSURE	EPS-AXIAL	EPS-CIRC.
3511.000	3006.000	0.201	0.240
4037.000	3006.000	0.247	0.291
5025.000	3006.000	0.334	0.385
6029.000	3006.000	0.421	0.485
6953.000	3006.000	0.496	0.575
7923.000	3006.000	0.567	0.677

Table 35 Raw strain data for sample C, unloading

STRESS	PRESSURE	EPS-AXIAL	EPS-CIRC.
4638.000	4081.000	0.266	0.309
5033.000	4081.000	0.299	0.346
6019.000	4081.000	0.383	0.443
6994.000	4081.000	0.462	0.540
7929.000	4081.000	0.528	0.637

Table 36 Volumetric strain data for sample C, unloading

STRESS	PRESSURE	VOL STRN
510	0	0.00485
1019	0	0.01165
2043	0	0.02615
3030	0	0.0407
3986	0	0.05485
4990	0	0.0696
6034	0	0.0844
6974	0	0.09745
7949	0	0.1106
1525	1030	0.01575
2051	1030	0.02295
3046	1030	0.0372
3992	1030	0.0505
5022	1030	0.0649
6027	1030	0.0791
6996	1030	0.0927
7886	1030	0.10515
2511	2006	0.0242
3034	2006	0.0315
4025	2006	0.0458
5018	2006	0.0598
6002	2006	0.07375
6980	2006	0.0878
8010	2006	0.1018
3511	3006	0.03405
4037	3006	0.04145
5025	3006	0.0552
6029	3006	0.06955
6953	3006	0.0823
7923	3006	0.09605
4638	4081	0.0442
5033	4081	0.04955
6019	4081	0.06345
6994	4081	0.0771
7929	4081	0.0901

Table 37 Raw strain data for Saratoga limestone, loading

STRESS	PRESSURE	EPS-AXIAL	EPS-CIRC.
500.940	0.000	0.114	0.091
998.000	0.000	0.224	0.201
1990.050	0.000	0.481	0.438
3009.450	0.000	0.764	0.722
4030.730	0.000	1.075	1.028
5032.840	0.000	1.328	1.311
6040.420	0.000	1.609	1.617
7018.160	0.000	1.868	1.882
7996.500	0.000	2.123	2.151

Table 38 Raw strain data for Saratoga limestone, loading

STRESS	PRESSURE	EPS-AXIAL	EPS-CIRC.
1496.910	1011.210	0.145	0.118
2002.880	1011.350	0.250	0.235
2992.210	1010.820	0.499	0.477
3987.620	1011.400	0.775	0.757
5006.500	1011.940	1.055	1.057
5998.490	1011.880	1.334	1.348
7010.340	1012.320	1.617	1.642
8032.140	1012.620	1.894	1.937

Table 39 Raw strain data for Saratoga limestone, loading

STRESS	PRESSURE	EPS-AXIAL	EPS-CIRC.
2507.990	1999.600	0.220	0.181
2985.920	1999.250	0.308	0.295
4011.040	1999.470	0.561	0.558
5026.730	2000.340	0.839	0.848
6025.390	2001.330	1.120	1.134
7022.770	2001.740	1.409	1.421
8019.880	2002.410	1.670	1.701

Table 40 Raw strain data for Saratoga limestone, loading

STRESS	PRESSURE	EPS-AXIAL	EPS-CIRC.
3503.630	2998.560	0.258	0.231
3989.460	2999.800	0.354	0.337
5030.030	3000.520	0.590	0.605
6021.420	3002.720	0.864	0.881
7013.860	3004.190	1.142	1.171
8009.480	3005.740	1.419	1.454

Table 41 Raw strain data for Saratoga limestone, loading

STRESS	PRESSURE	EPS-AXIAL	EPS-CIRC.
4503.990	4004.810	0.310	0.292
5003.180	4006.150	0.405	0.406
5995.690	4007.340	0.637	0.655
7032.910	4007.820	0.913	0.946
8027.580	4008.590	1.199	1.232

Table 42 Volumetric strain data for Saratoga limestone, loading

STRESS	PRESSURE	VOL STRN
501	0	0.01486
998	0	0.03131
1990	0	0.067815
3009	0	0.110385
4031	0	0.15661
5033	0	0.197525
6040	0	0.242135
7018	0	0.281605
7996.5	0	0.321185
1497	1011	0.01903
2003	1011	0.03605
2992	1011	0.072595
3988	1011	0.11442
5006.5	1012	0.158465
5998.5	1012	0.201505
7010	1012	0.245065
8032	1013	0.28837
2508	2000	0.029115
2986	1999	0.044865
4011	1999.5	0.083855
5027	2000	0.126745
6025	2001	0.16942
7023	2002	0.212495
8020	2002	0.25355
3504	2999	0.036025
3989.5	3000	0.051335
5030	3000.5	0.09
6021	3003	0.131315
7014	3004	0.17423
8009.5	3006	0.21635
4504	4005	0.044645
5003	4006	0.06085
5996	4007	0.09735
7033	4008	0.14028
8028	4009	0.183095

Table 43 Raw strain data for Saratoga limestone, unloading

STRESS	PRESSURE	EPS-AXIAL	EPS-CIRC.
486.220	0.000	0.142	0.115
977.310	0.000	0.300	0.240
2001.280	0.000	0.631	0.561
3003.510	0.000	0.934	0.858
3980.400	0.000	1.216	1.143
4982.760	0.000	1.484	1.410
5976.710	0.000	1.724	1.673
6981.660	0.000	1.935	1.922
7996.500	0.000	2.123	2.151

Table 44 Raw strain data for Saratoga limestone, unloading

STRESS	PRESSURE	EPS-AXIAL	EPS-CIRC.
1482.350	1009.650	0.148	0.119
2000.940	1010.340	0.327	0.266
2982.020	1011.190	0.637	0.576
3997.170	1011.240	0.948	0.873
4985.350	1011.610	1.218	1.153
5975.850	1012.070	1.470	1.421
6950.480	1012.010	1.697	1.685
8032.140	1012.620	1.894	1.937

Table 45 Raw strain data for Saratoga limestone, unloading

STRESS	PRESSURE	EPS-AXIAL	EPS-CIRC.
2501.630	1997.810	0.214	0.176
3006.870	1997.790	0.363	0.314
3982.920	1999.290	0.675	0.604
4975.780	1999.690	0.970	0.904
5947.010	2000.590	1.225	1.176
6933.050	2001.170	1.461	1.447
8019.880	2002.410	1.670	1.701

Table 46 Raw strain data for Saratoga limestone, unloading

STRESS	PRESSURE	EPS-AXIAL	EPS-CIRC.
3500.180	3000.240	0.256	0.227
4004.590	3001.220	0.401	0.358
4985.680	3001.770	0.699	0.648
5994.650	3002.750	0.980	0.931
6991.030	3004.480	1.214	1.205
8009.480	3005.740	1.419	1.454

Table 47 Raw strain data for Saratoga limestone, unloading

STRESS	PRESSURE	EPS-AXIAL	EPS-CIRC.
4493.050	4001.900	0.303	0.284
5015.890	4002.480	0.442	0.412
6003.500	4004.820	0.730	0.692
7023.490	4006.770	0.980	0.973
8027.580	4008.590	1.199	1.232

Table 48 Volumetric strain data for Saratoga limestone, unloading

STRESS	PRESSURE	VOL STRN
486	0	0.018595
977	0	0.039005
2001	0	0.087585
3004	0	0.132465
3980	0	0.175085
4982	0	0.215225
5977	0	0.253505
6982	0	0.288975
7997	0	0.321185
1482	1010	0.019275
2001	1010	0.04296
2982	1011	0.089415
3997	1011	0.13473
4985	1011	0.176185
5976	1012	0.21562
6958	1012	0.25336
8032	1013	0.28837
2502	1998	0.02831
3007	1998	0.049575
3983	1999	0.094185
4976	2000	0.13896
5947	2001	0.178895
6933	2001	0.217785
8020	2002	0.25355
3500	3000	0.03546
4005	3001	0.05578
4986	3002	0.099745
5995	3003	0.142105
6991	3004	0.181195
8009	3006	0.21635
4493	4002	0.043525
5016	4002	0.06325
6004	4005	0.10571
7023	4007	0.14628
8028	4009	0.183095

Table 49 Raw strain data for Saratoga limestone, loading, pressure unloading

STRESS	PRESSURE	EPS-AXIAL	EPS-CIRC.
507.400	0.000	0.068	0.074
987.140	0.000	0.195	0.200
1988.100	0.000	0.468	0.465
3021.840	0.000	0.766	0.761
3991.950	0.000	1.046	1.054
5000.580	0.000	1.329	1.352
5997.140	0.000	1.602	1.644
6991.510	0.000	1.860	1.918
7998.300	0.000	2.135	2.209

Table 50 Raw strain data for Saratoga limestone, loading, pressure unloading

STRESS	PRESSURE	EPS-AXIAL	EPS-CIRC.
1504.320	997.170	0.175	0.173
1999.270	997.250	0.278	0.288
2989.660	997.870	0.547	0.533
4016.320	998.410	0.815	0.822
5023.200	998.950	1.089	1.112
7001.440	999.090	1.635	1.681
6981.960	999.350	1.646	1.689
8003.800	999.530	1.900	1.949

Table 51 Raw strain data for Saratoga limestone, loading, pressure unloading

STRESS	PRESSURE	EPS-AXIAL	EPS-CIRC.
2501.150	1997.620	0.214	0.201
2986.390	1998.210	0.317	0.313
3993.190	1999.070	0.567	0.575
5019.190	1998.590	0.832	0.855
5982.130	1999.710	1.128	1.147
7017.820	2000.250	1.392	1.423
8078.850	2000.750	1.683	1.728

Table 52 Raw strain data for Saratoga limestone, loading, pressure unloading

STRESS	PRESSURE	EPS-AXIAL	EPS-CIRC.
3508.460	3001.630	0.276	0.244
4012.590	3002.060	0.379	0.363
4991.710	3003.980	0.597	0.605
6003.370	3003.990	0.865	0.883
7041.400	3004.910	1.152	1.175
8024.250	3005.590	1.425	1.457

Table 53 Raw strain data for Saratoga limestone, loading, pressure unloading

STRESS	PRESSURE	EPS-AXIAL	EPS-CIRC.
4503.990	4004.810	0.310	0.292
5003.180	4006.150	0.405	0.406
5995.690	4007.340	0.637	0.655
7032.910	4007.820	0.913	0.946
8027.580	4008.590	1.199	1.232

Table 54 Volumetric strain data for Saratoga limestone, loading, pressure unloading

STRESS	PRESSURE	VOL STRN
507	0	0.01076
987	0	0.02978
1988	0	0.069885
3022	0	0.11442
3992	0	0.15771
5001	0	0.201625
5997	0	0.24452
6992	0	0.28473
7998	0	0.32763
1504	997	0.026065
1999	997	0.042735
2990	998	0.08061
4016	998	0.12291
5023	999	0.16564
7001	999	0.249865
6982	999	0.251135
8004	1000	0.28986
2501	1998	0.0308
2986	1998	0.04714
3993	1999	0.08586
5019	1999	0.127085
5982	2000	0.17108
7018	2000	0.21188
8079	2001	0.2569
3508	3002	0.038225
4013	3002	0.05522
4992	3004	0.090325
6003	3004	0.13156
7041	3005	0.175165
8024	3005	0.21691
4504	4005	0.044645
5003	4006	0.06085
5996	4007	0.09735
7033	4008	0.14028
8028	4009	0.183095

Table 55 Raw strain data for Saratoga limestone, unloading, pressure unloading

STRESS	PRESSURE	EPS-AXIAL	EPS-CIRC.
503.770	0.000	0.162	0.156
1009.540	0.000	0.322	0.299
2015.560	0.000	0.647	0.609
3009.860	0.000	0.943	0.911
3972.640	0.000	1.190	1.158
5011.020	0.000	1.489	1.458
6009.040	0.000	1.739	1.725
6990.960	0.000	1.948	1.969
7998.300	0.000	2.135	2.209

Table 56 Raw strain data for Saratoga limestone, unloading, pressure unloading

STRESS	PRESSURE	EPS-AXIAL	EPS-CIRC.
1509.730	996.370	0.177	0.166
2021.780	995.330	0.327	0.302
3001.970	996.190	0.654	0.606
3993.990	997.480	0.951	0.904
4988.380	998.040	1.226	1.186
5996.660	998.750	1.480	1.450
6981.770	998.360	1.702	1.714
8003.800	999.530	1.900	1.949

Table 57 Raw strain data for Saratoga limestone, unloading, pressure unloading

STRESS	PRESSURE	EPS-AXIAL	EPS-CIRC.
2495.830	1998.600	0.221	0.206
3006.200	1998.320	0.366	0.332
4009.420	1997.760	0.667	0.624
5003.440	1998.960	0.968	0.918
6005.770	1999.860	1.235	1.196
7020.970	2000.090	1.466	1.461
8078.850	2000.750	1.683	1.728

Table 58 Raw strain data for Saratoga limestone, unloading, pressure unloading

STRESS	PRESSURE	EPS-AXIAL	EPS-CIRC.
3496.990	2999.310	0.263	0.235
3998.630	2999.810	0.401	0.369
5006.740	3000.520	0.703	0.645
6003.460	3002.460	0.979	0.933
6964.470	3004.070	1.210	1.197
8024.250	3005.590	1.425	1.457

Table 59 Raw strain data for Saratoga limestone, unloading, pressure unloading

STRESS	PRESSURE	EPS-AXIAL	EPS-CIRC.
4493.050	4001.900	0.303	0.284
5015.890	4002.480	0.442	0.412
6003.500	4004.820	0.730	0.692
7023.490	4006.770	0.980	0.973
8027.580	4008.590	1.199	1.232

Table 60 Volumetric strain data for Saratoga limestone, unloading, pressure unloading

STRESS	PRESSURE	VOL STRN
504	0	0.02367
1010	0	0.04599
2016	0	0.093275
3010	0	0.138295
3973	0	0.175335
5011	0	0.22023
6009	0	0.25949
6991	0	0.29435
7998	0	0.32763
1510	996	0.025405
2022	996	0.046545
3002	996	0.0933
3994	997	0.137955
4988	998	0.17985
5997	999	0.218965
6982	998	0.256505
8004	1000	0.28986
2496	1999	0.031655
3006	1998	0.051505
4009	1998	0.09572
5003	1999	0.14022
6006	2000	0.18137
7021	2000	0.210375
8079	2001	0.2569
3497	2999	0.03666
3999	3000	0.0569
5007	3001	0.09965
6003	3002	0.14223
6964	3004	0.180235
8024	3006	0.21691
4493	4002	0.043525
5016	4002	0.06325
6004	4005	0.10571
7023	4007	0.14628
8028	4009	0.183095

Table 61 Parameters of the response surface for all deformation tests

SAMPLE	CYCLE	λ	x_1	x_2	x_3	x_4	x_5	x_6
B	LOADING	1.0	-0.00184	0.1417E-4	-0.4886E-5	0.1010E-9	-0.2307E-9	0.4627E-10
B	UNLOADING	1.03	-0.00217	0.1414E-4	-0.6484E-5	0.4572E-11	-0.1204E-9	0.2589E-0
B-DEC. P	LOADING	0.95	-0.00114	0.1643E-4	-0.6567E-5	-0.4015E-10	0.3685E-10	0.6126E-10
B-DEC. P	UNLOADING	1.0	-0.00292	0.1489E-4	-0.6309E-5	-0.1625E-10	-0.1027E-10	0.1538E-9
C	LOADING	1.03	-0.00389	0.1298E-4	-0.2593E-5	0.6817E-10	-0.1763E-9	-0.2119E-9
C	UNLOADING	1.04	-0.00301	0.1284E-4	-0.3734E-5	0.4129E-10	-0.8566E-10	-0.9527E-10
SARATOGA	LOADING	0.9	-0.00326	0.4762E-4	-0.3883E-4	-0.2158E-9	0.6818E-10	0.3020E-9
SARATOGA	UNLOADING	1.22	-0.01205	0.3255E-4	-0.2885E-4	0.8444E-10	-0.7683E-9	0.7809E-9
SAR-DEC . P	LOADING	1.0	-0.00825	0.4005E-4	-0.3009E-4	0.2876E-9	-0.1147E-8	0.3343E-9
SAR-DEC. P	UNLOADING	1.175	-0.00607	0.3424E-4	-0.3239E-4	0.7382E-10	-0.8601E-9	0.1232E-8

DISTRIBUTION:

1	MS 0701	R. W. Lynch, 6100
1	MS 0706	D. A. Northrop, 6112
1	MS 0705	M. W. Scott, 6114
10	MS 0705	N. R. Warpinski, 6114
1	MS 0751	W. R. Wawersik, 6117
1	MS 0751	J. C. Lorenz, 6117
1	MS 0751	D. J. Holcomb, 6117
10	MS 0751	L. W. Teufel, 6117
1	MS 9018	Central Technical Files, 8523-2
5	MS 0899	Technical Library, 7141
1	MS 0619	Technical Publications, 7151
10	MS 0100	Document Processing, 7613-2 For DOE/OSTI

DATE
FILMED
10/17/94
END